Label-Free, Microfluidic Biosensors with Printed, Floating-Gate Transistors

A Dissertation
SUBMITTED TO THE FACULTY OF
UNIVERSITY OF MINNESOTA
BY

Scott White

IN PARTIAL FULFILLMENT OF THE REQUIREMENTS
FOR THE DEGREE OF
DOCTOR OF PHILOSOPHY

Advisors: C. Daniel Frisbie and Kevin D. Dorfman

December 2017

Acknowledgements

This dissertation could have never been completed without the gracious and generous support of the people I've met during my graduate career. Most saliently, I must acknowledge the great advisement I've received from both Dan and Kevin. It is hard for me to imagine better role models for my scientific future or a better match for my developing research style. Their foresight and expertise were paramount to designing and implementing my Ph.D. work.

While I am writing this as an individual, the presented work involved a cadre of fantastic scientists. In rough chronological order, I would thank a fantastic homework group that carried me through the coursework requirements including (but not limited to) Dr. Dayne Plemmons, Koustav Ganguly, Francisco Pelaez, Mike Hollowed (Fluids Partner 1), Max Kruziki (Fluids Partner 2), Dr. Boxin Tang, Nittish Mittal, Akash Arora, Teresa Sells, and Dr. Mark Sullivan. My GPA would be measurably lower without their help.

In the laboratory domain, I have to thank Dr. Se Hyun Kim, Dr. Kihyon Hong, Dr. Wei Xie, and Dr. Bryan Paulsen for the fantastic mentoring during the initial phases of my laboratory experience. Without the knowledge they passed down to me I would still be trying to print and test a single device. A repeat shout-out to Prof. Dorfman is warranted as we tried to orient ourselves in the electronics space while Dan was on sabbatical. For any and all things related to biochemistry, microfluidics, or microfabrication I am indebted to Dr. Julian Sheats, Dr. Joel Thomas, Dr. Scott King, Dr. Damini Gupta, Pranav Agrawal, and Dr. Chang-Hyun Kim.

Once I got my feet underneath me in lab, I leaned heavily on the brilliance of colleagues a fraction of which will be mentioned here. I apologize in advance for all those left out. Dr. Zuoti Xie's outstanding insights into physical chemistry had major impacts on Chapter 4 of this thesis and impacted all the work stemming from it. I must thank Dr. Abel Demissie, Dr. Chris Smith, Dr. Stuart Oram, and Dr. Davood Taherina for politely reminding me that I don't *really* understand chemistry to a degree comparable to them. This void was routinely filled without a modicum of grumbling. Dr. Zhicheng Long, Dr. Hongchul Moon, and Dr. Geoffrey Rojas deserve congressional commendation for their inspiring work ethic and the countless experimental "shortcuts" they taught me. Dr. Yanfei Wu deserves a solitary shout-out for her outstanding AFM skills and gracious help when generating micrographs of my functionalized surfaces. Mathew Thomas is credited with arguably the most rewarding moment of my graduate experience when he independently reproduced some of my fundamental results.

Dr. Ankit Mahajan, Elliot Schmidt, Fazel Bidoky, Akash Arora, Dr. Damini Gupta, Dr. Donghoon Song, Dr. Woo-Jin Hyun, Motao Cao, Dr, Tao He and Xinglong Ren deserve special credit for their commiseration, comedic relief, and technical help whenever it was requested. I will forever remember reprogramming an ancient impedance analyzer with Ankit, Fazel, and Woo-Jin for more hours than I care to numerate. It is a concrete example of a truly global effort (Korea, Iran, India, and … Iowa) working towards a common goal. Maybe the path to world peace is lined with frustratingly outdated research equipment…

I also want to thank more tangential collaborators who made fantastic contributions with proportionally smaller effort. Prof. Lorraine Francis graciously permitted me in her lab from Day 1. Prof. Srinand Sreevatsan and Dr. Elisa Lamont in Veterinary Science catalyzed the development of my Ph.D. after only one personal meeting. I also had fantastic undergraduate workers who are destined for career success including Robert, Nez, Trevor, Charlie, and Maggie.

On a more personal note, credit is warranted for the great friendships developed during my graduate experience. I've had stellar roommates in Dr. Dayne Plemmons, Koustav Ganguly, and Frankie Pelaez at the NE "Monastery". I've had great sports therapists (both real sports and fantasy sports) in Andrew Allman, Matt Quan, Jeff Walter, Dr. Larry Stern, Sadie Johnson, and Ralm Ricarte. Finally, the great facilities and staff at the UMN Rec Center and NE pubs deserve special thanks for constantly supplying me with mental health maintenance in the form of free weights and cheap libations. The acknowledgements I should direct at Brittany Forkus could fill a stand-alone thesis. But, specifically, her unrelenting stubbornness/obstinance/hard-headedness towards scientific results pushed my communication skills far beyond what any presentation, proposal, publication, or workshop could offer.

To all those unintentionally unnamed – you know who you are. I apologize again for omitting you here. However, I'm confident you are very busy solving all the world's scientific problems in industry, academia, and government. My experience at Minnesota has made me very optimistic about the future of scientific advancement and I look forward to the possibility of working with you all again.

Abstract

Printed electronics and microfluidics are two emerging and developing technologies with the common attractive feature of scalability. Advancements in fabrication capabilities have evolved research questions from, “What can we build?” to, “What *should* we build?”. This work focuses on the combination of these two technologies and their application to biosensing. The motivating theme is to understand how integrated, functional materials interact, elucidate the underlying molecular phenomena, then utilize the emergent advantages to address the outstanding limitations of conventional biosensing strategies.

Printed electronics have recently been applied to biological detection with a variety of techniques[1] while microfluidics, since their inception, have been used to handle biological fluids.[2] The work presented here outlines a patented sensing strategy based off Floating-Gate Transistors (FGTs). The FGT design physically separates the electronic materials and biological fluids and thus bypasses various compatibility obstacles limiting other next-generation sensor technologies.[3] The specific changes in interfacial properties that lead to robust signal transduction are derived empirically.[4] This is followed by a mechanistic investigation into the molecular origin of sensor operation when FGTs are used in biomolecular detection. Finally, the versatility and scalability engendered by facile prototyping of FGTs is exemplified by successful iterations to DNA,[3] ricin,[5] and gluten proteins.

The first proof-of-principle experiments incorporated printed electronics with an elementary biological system of DNA oligonucleotides. The results successfully

demonstrated the potential of FGTs but failed to solidify their concrete value. Systematic investigation into the complex dynamics at the interface of chemically functionalized electrodes and electrolytes uncovered the most attractive features of the FGT technology. The chemistry was tuned with molecules that range in complexity from simple, short-chain alkyl-thiols to reversible protein-protein interactions. The observed responses with well-controlled systems were generalized to real systems like protein capture in food matrices (e.g. ricin in milk, orange juice). The resulting versatility originated from the label-free, electronic sensing mechanism and opened a range of possibilities for FGTs' impact.

The fundamental insights into interfacial dynamics, device operation, and biomolecular interactions were made possible by the advancements in the materials science and fabrication techniques underlying the presented results. Future avenues of development are hypothesized along with the most promising strategies. The continued elucidation of the physical mechanism and engineering upgrades justify the proposed strategies and inspire the continued effort to fully realize the potential of FGT biosensors.

Contents

List of Figures

List of Figures (cont.)

List of Figures (cont.)

List of Tables

1. Introduction

Printed electronics and microfluidics are two actively researched technologies to uncover fundamental physical insights[6,7] and to expand their practical advantages for commercially driven applications.[8,9] They are attractive due to their manufacturing scalability[10] and prototyping flexibility[2] and have been adopted into applications ranging from energy conversion[11] to personal healthcare.[12] However, researchers have not yet realized the full capabilities of their technical values due to challenges in material design and device fabrication.[10,13] The crux of this thesis seeks to combine these two seemingly orthogonal technologies and utilize them to positively impact the sensing sector.

The innovative combination presented is based on a floating-gate transistor (FGT) strategy shown schematically in Figure 1.1. The geometry exploits the low-voltage performance of printed electronics and the precise fluid handling of microfluidics while conserving their scalability.[14] FGTs physically separate the biological fluids in the microfluidics from the electronic materials thus bypassing many of the compatibility and material constraints inherent to next-generation sensor design. The use of electrolyte

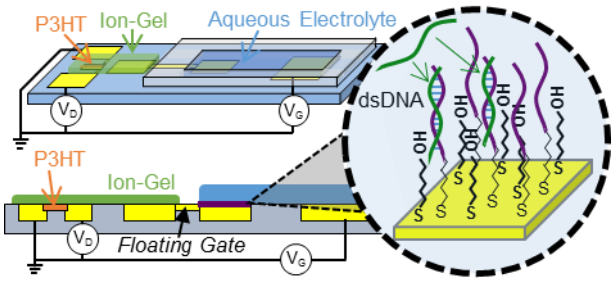

Figure 1.1: Schematic of Floating-Gate Transistor Sensing Platform.
The microfluidics are physically separated from the printed electronics and the floating-gate/aqueous interface is functionalized with capture molecules so that analyte binding perturbs the interfacial properties of the floating gate.

dielectrics further expands the geometries available for FGT construction but also presents unique and novel mechanistic operation of molecular transduction.

The inherent amplification properties of transistors[15] and the sensitivity of device output on interfacial properties permit the FGT strategy to transduce molecular binding without the use of secondary binding agents.[16] Bypassing this step cuts down the time to operate the sensor and presents a major feature for sensor application. Furthermore, the use of microfluidics mitigates the time for molecular binding due to the elimination of mass transport limitations by incorporating flow.[17] The rapid transduction permitted by FGTs serves as the principal advantage of this technique compared to conventional techniques. In contrast to other next-generation sensors, the FGT technique conserves the facile operation and automatability of electronics and microfluidics enabling the technique to be readily adopted to sectors with limited technical expertise often referenced as "field-ready" applications.[18] These features stem from systematic investigation into the operating principles and physical properties of the novel materials that are discussed in detail in this thesis. The results provide valuable scientific insight into emerging materials and highlight remaining obstacles to realizing their potential capabilities.

1.1 Thesis Overview

The following chapters are organized as follows. Chapter 2 begins by putting the work in proper context by surveying the conventional sensing techniques and the motivations behind their continued development. It then provides a brief background on the fundamental operating principles of printed electronics and the experimental methods to fabricate the devices. This is meant as an introduction to the more in-depth discussions in the subsequent chapters.

Chapters 3 through 6 present my experimental results and associated discussions, all of which are published[3–5] or soon-to-be published in scientific journals. Chapter 3 discusses the first version of the FGT technology applied to the detection of DNA oligomers. The work demonstrated the feasibility of the sensing strategy and serves as a "proof-of-principle" for the FGT biosensing strategy. DNA was successfully detected quantitatively and showed good selectivity to mismatched DNA but the performance demonstrated that the version was not optimized to its full potential. The results presented in this chapter have been published as "Label-Free DNA Sensing Platform with Low-Voltage Electrolyte-Gated Transistors" by White, S.P., Dorfman, K.D., and Frisbie, C.D. in the journal *Analytical Chemistry* 87.3 (2015): 1861-1866.

Chapter 4 explores the operating and sensing mechanism of the FGT technology in depth. The experimental platform mimics that used to detect DNA but with well-understood materials in lieu of complex biological molecules. The same ion-gel material was used to capacitively couple a floating gate electrode to both the transducing semiconductor and the externally controlled control gate (CG). The interfacial area between the ion-gel and electrodes were systematically varied to empirically determine the sizes that would lead to a desired operation. We constructed a simple lumped capacitor model with a correction factor to explain the discrepancies between the observed results to those predicted from the simple model. The origin of the observed hysteresis was discussed with applications to the broader printed electronics community. In the next stage of the experimental work, the chemistry of the interfaces was tuned with self-assembled monolayers (SAMs) to control the work functions of the electrodes and connect them to the measured output of the device. We found that the changes in the measured output

depend on both the chemical changes to the work function and the changes in capacitance due to SAM thickness. The results allow for more intelligent and sophisticated optimization of the FGT platform for improved sensing applications. The work is published as "Operating and Sensing Mechanism of Electrolyte-Gated Transistors with Floating Gates: Building a Platform for Amplified Biodetection" by White, S.P., Dorfman, K.D., Frisbie, C.D., in the *Journal of Physical Chemistry C* 120.1 (2016): 108-117.

Chapter 5 uses the lessons learned from Chapter 4 to improve the FGT sensor and apply it to the protein ricin. The electrode areas were turned for optimal performance and functionalized with DNA aptamers from the Sreevatsan Lab at the University of Minnesota. The biological fluid was delivered with a microfluidic system that was designed to rapidly deliver the solution to the functionalized surface and prevent it from fouling or contaminating other areas of the sensor. Ricin was successfully transduced when it was dissolved in buffer, orange juice, and milk demonstrating the flexibility and versatility of the platform to complex media and food matrices. Compared to the DNA sensor, the ricin sensor has a 100x improvement in detection limit with a reduction in the transduction time. The work is published as "Rapid, Selective, Label-Free Aptameric Capture and Detection of Ricin in Potable Liquids using a Printed Floating Gate Transistor" by White, S.P., Sreevatsan, S., Frisbie, C.D., and Dorfman, K.D. in *ACS Sensors* 1.10 (2016): 1213-1216.

Chapter 6 expands the capabilities of the FGT platform to gluten detection by utilizing the inherent multiplexability of printed electronics and microfluidics. It incorporated both DNA aptamers and antibodies to capture gluten from wheat and barley in a complex extraction matrix. The resulting signal from the set of FGTs properly identifies gluten below the regulatory limit in a manner that quantitatively depends on the

specific gluten source. The latter feature allows a given sample to be over analyzed with multiple FGTs in parallel so that a "signature" can be generated and used to improve the accuracy of the measurement. The work will soon be published as, "Detection and Sourcing of Gluten in Grain with Multiple, Tunable Floating-Gate Transistor Biosensors" by White, S.P., Frisbie, C.D., and Dorfman, K.D. in *ACS Sensors*.

Chapter 7 discusses future directions of the work and the remaining obstacles that need to be overcome to fully realize the potential benefits of FGT biosensors. Applications into cellular detection would be greatly facilitated by improvements in the electronic performance and physical design of the sensing electrode.

2. Motivation and Research Objectives

2.1 Perspectives on Sensor Research

Sensors lie at the interface between theory and experiment for all scientific endeavors ranging from handheld monitors to entire space satellites. The simplest distinction between sensor types delineates physical sensors that measure bulk properties from chemical sensors that identify the composition of complex systems. The field of analytical chemistry focuses on the latter with molecular scale detection strategies. The developments impact a wide range of sectors including environmental science,[19,20] food safety,[21,22] and healthcare.[23]

The target application further distinguishes the class of sensor. The scope of this experimental work focuses on diagnostic sensors for routine analysis as opposed to systems that are predominantly used for research purposes. Methods focused on research such as Nuclear Magnetic Resonance (NMR) ,[24] single-molecule fluorescent assays,[25] or the Nobel Prize winning Cryo-Electron Microscopy[26] will be referenced only to put the experiments in the relevant context. Routine diagnostics are central features of many sectors such as personal healthcare,[23] environmental monitoring,[20] process quality control,[27] and food safety.[22] Finally, the chemical nature of the target molecules breaks down the technical class of the sensor to DNA,[28] protein,[29] cellular,[30] and small molecule[31] detection schemes. A map of sensor classes is shown in Figure 2.1. It is important to note that these distinctions are often broad as routine diagnostic tools are commonly used for R&D purposes and vice versa.

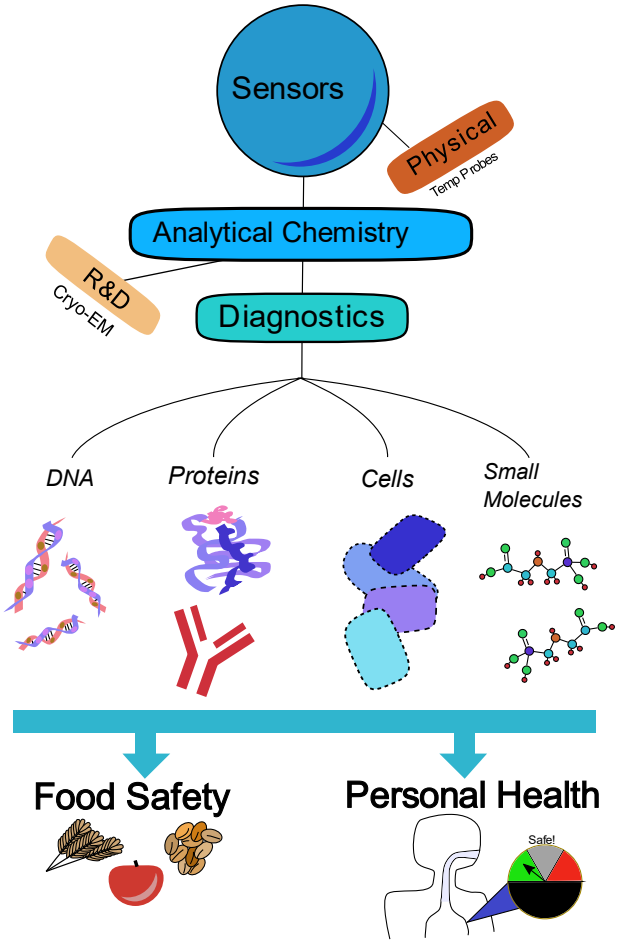

Figure 2.1: Survey of Sensor Distinctions.
The first branch separates chemical sensors from physical sensors. The next separates chemical sensors for R&D from those for diagnostics. From there, the sensors are distinguished by the nature of the target: DNA, proteins, cells, or small molecules. Finally, the industrial sector for diagnostic application is broken into food safety and personal health.

2.2 Available methods

The technology underlying a given sensor is consciously tailored to fit the target application. DNA detection strategies benefit from considerable interest because the genetic material of a potential contaminant provides pronounced specificity for a given biomarker.[32] The invention of the polymerase chain reaction (PCR) catalyzed the development of many DNA detection methods due to PCR's ability to accurately amplify

small amounts of target DNA.[33] Recent years have witnessed another revolution in DNA detection methods with the advent of sequencing methods.[34] Sanger Sequencing reconstructs the DNA molecules base-by-base with fluorescent dyes specific to each base.[35] Emerging techniques such as nanopore sequencing improve on the limitations of Sanger Sequencing such as speed and read length.[36] While profound, current sequencing methods prove too cumbersome for every diagnostic analysis. In many cases, gene-level resolution is all that is required to execute an accurate diagnosis motivating techniques such as DNA Microarrays.[37] Here, the genetic site is removed from the whole genome, amplified with PCR, tagged with a fluorescent dye, then exposed to a plate of binders designed to represent the gene of interest. Microarrays can also be used to assess the relative degrees of gene expression under different experimental conditions.[38] In other cases, even gene-level resolution is too cumbersome and a simple confirmatory diagnostic

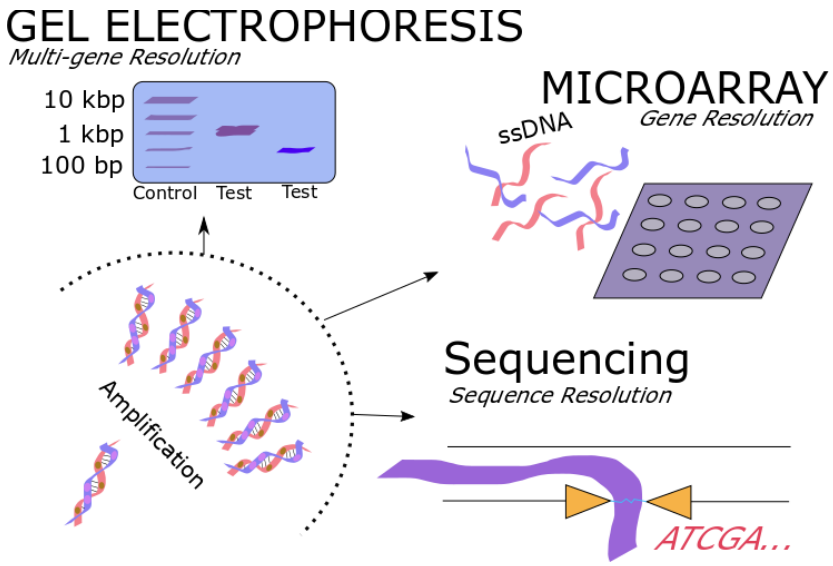

Figure 2.2: Survey of Analytical Methods for DNA.
In the bottom left, a single piece of DNA is amplified via a PCR technique. The amplified set of DNA can be confirmed with a low-resolution, multi-gene detection technique such as gel electrophoresis. The number of specific genes can then be assessed with a DNA microarray that pinpoints certain genes of interest. Finally, high-resolution, sequence-specific techniques such as Nanowire sequencing can outline the order of nucleotides in the DNA.

from a multi-gene level is more useful. Example applications include extraction of DNA from cells or confirmation that a PCR scheme was successful. Techniques such as gel electrophoresis are sufficient in these low-resolution cases. Here, a DNA sample is driven through a porous material (a "gel") by an electric field that directs the negatively charged DNA molecules at a rate inversely proportional to the size of the DNA.[39,40] A schematic of these various methods is shown in Figure 2.2.

Protein detection methods are far more complicated relative to DNA due to the highly variable chemistry of amino acids.[41] As such, no analogous "protein amplification" technique like PCR exists and its absence drastically limits the possibility of transferring DNA methods like sequencing over to proteins.[41,42] As a result, it is more useful to distinguish protein analytical methods based on a compromise between their speed and power. Mass Spectrometry (MS) is the most powerful protein analytical method and is the closest technique to "protein sequencing" available today.[43] With MS, a small amount of sample is injected, ionized, then jetted across a magnetic field that redirects the flow path to a degree inversely proportional to the ratio of the mass of the protein fragment to its charge (m/z). The resulting plot of intensity vs m/z yields a signature unique to the initial sample.[44] Higher chemical resolution of the protein sample can be achieved with chemical pre-treatments of the sample before injection.[44] The high-order signatures can be used to generate the amino acid sequence of some proteins and/or post-translational modifications though it has limitations with more complex protein structures.[45] Protein mixtures can be assessed by MS combined with separations such as liquid chromatography (LC-MS) or gas chromatography (GC-MS).[46] While very powerful, these combination separation/spectrometric analytical methods are very slow and difficult to use limiting their

routine use in diagnostics and handcuffing their potential impact to the scientific community.[47]

Immunological assays represent another option for protein analytics by sacrificing the sensing power of MS for improved speed and usability. The dominant technique is the Enzyme-Linked Immunosorbent Assay (ELISA) that uses a 96 well plate coated with antibodies to capture the target protein of interest.[48–50] Once bound, the formation of a complex can be transduced with two modes: sandwich[51] or competitive.[52] In a sandwich assay, a second antibody that has been functionalized with a colorimetric moiety is also bound to the antibody-protein complex and quantified with a plate reader for the designed absorbance.[51] In competitive assays, the functionalized moiety competes for binding to the

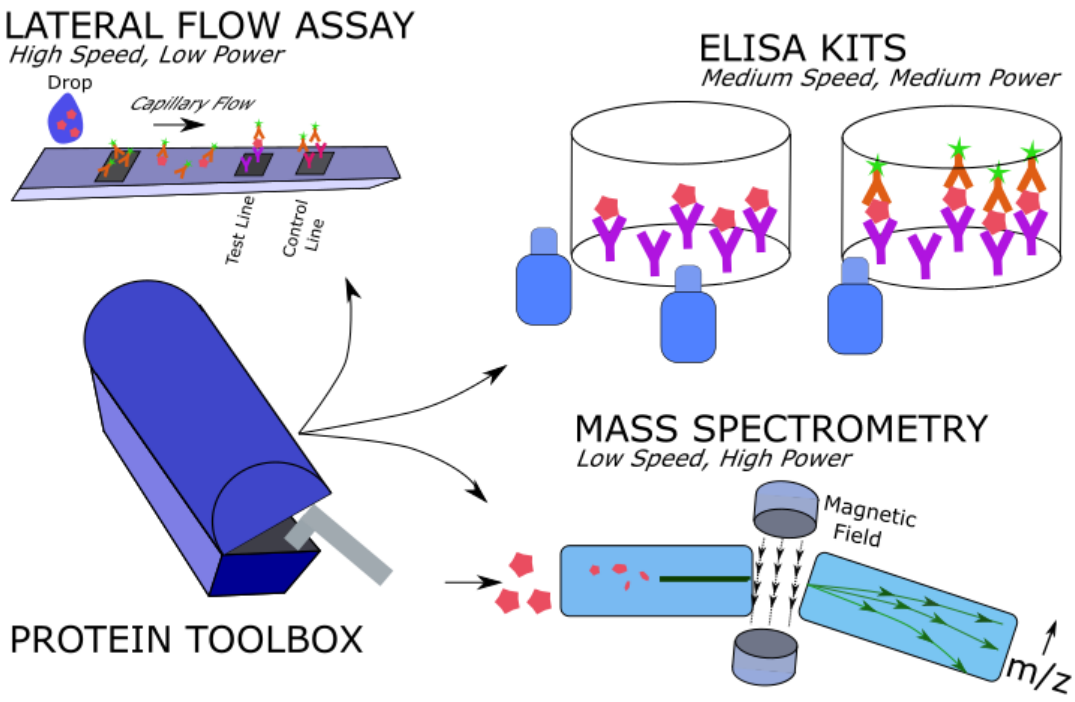

Figure 2.3: Protein Analytical Strategies.
The toolbox of protein analytical methods represents a spectrum of high power, low speed (e.g. mass spectrometry) to low power and high speed (lateral flow assays).

plate surface with the target analyte so that more colorimetric readout implies a lower amount of target protein in the unknown sample.[52,53] These two modes have been applied widely in the biomedical or food safety space to assess the presence of protein contaminants or biomarkers. They are far more adopted than MS methods but still require technical training to operate and at least 2.5 hours to generate results.[54] They also serve as a valuable research tool for characterizing experiments in protein engineering.[55]

Lateral Flow Assays (LFA) are the simplest analytical method as exemplified by over the counter pregnancy tests.[56] A liquid sample containing the target protein (or small molecule) is dropped onto a wicking pad that is flowed across the strip via capillarity. The liquid interacts with a "line" of colorimetric antibodies that enter the solution. The colorimetric antibodies bind to the target in solution (if present) and deposit onto a "test line" that specifically bind the target-antibody complex. A positive result is measured by the appearance of a color change on said test line at the end of the test. LFAs are extremely fast and easy, requiring minimal training and less than an hour. However, they have poorer detection limits than other methods and are only semi-quantitative at best.[56,57] Figure 2.3 outlines the major subsets of protein analytical methods available for use and considerable research and development.

The final, major class of biosensors are devoted to cellular assays. The analytical tool used to assess the presence of cells is primarily dictated by the amount of resolution needed as shown in Figure 2.4. At the highest level of resolution (inner circle of Figure 2.4), the specific strain of the bacterial contaminant is desired requiring a genomic assay including PCR amplification and the corresponding DNA analytical method outlined

above.[58] PCR-based methods are a very common analytical mode for research purposes in areas such as synthetic biology or cellular engineering.[33,58] In many cases only the species is necessary to diagnose a contamination and can be discovered by growing the target in a medium selective to species of interest. These media operate by incorporating a combination of antibiotics selective to non-target species and nutrients selective to the target species leading to an indication of the growth.[59] The penalty for such specificity is time as these assays take days to a week to complete.[59,60] Faster assays for classes of species are available that indicate the presence of, for example, coliforms and represent the next layer of resolution.[61,62] Finally, the lowest resolution methods probe for any biomass by assessing the content of adenosine triphosphate (ATP). This test works well but it does not distinguish between living or dead biomass so it is only useful to verify the quality of a cleaning process.[63,64]

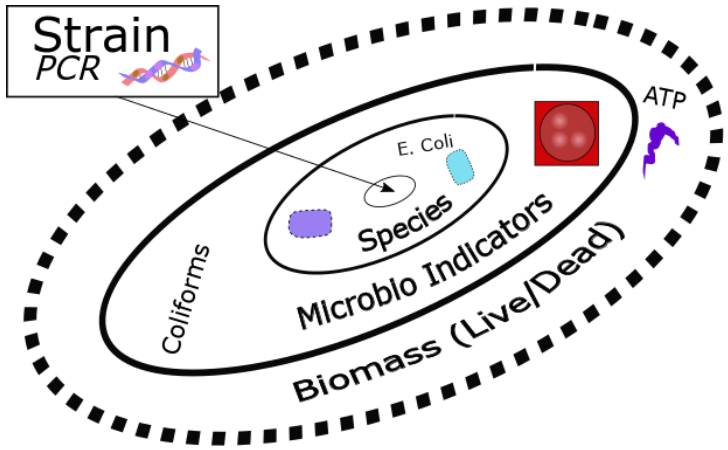

Figure 2.4: Cellular Analytical Schemes.
At the highest level of resolution lies strain specific methods that rely on PCR amplification of the genome. After than comes species-level resolution that distinguishes *e. coli* from *salmonella* for example. Beyond that are microbiological indicators that measure the presence of any species in a broader class such as coliforms. Finally, ATP indicators can assess the presence of any biomass whether the source is alive or dead.

2.3 Research Advancements in Sensing

Technological advancement in each of the above sensor classes have benefitted greatly from continued research and development efforts. Conventional efforts work to improve on the capabilities of existing analytical techniques. DNA sequencing has seen substantial improvements through nanowire sequencing[36,65] and DNA barcoding in genome mapping[66,67] to more accurately construct the sequenced genome. Similarly, MS methods are routinely adopted to new areas with advancements in sample injection and data analysis for more accurate, streamlined operation.[68] Derivatives of ELISA are also developed by incorporating paper microfluidics or advancing the chemical transduction mechanisms.[69,70] Finally, improvements in cellular assays focus on improvement of the species-selective media to minimize the exorbitantly long times necessary to grow a single species.[71,72] Further R&D efforts are devoted to next-generation sensing technologies to expand beyond the common methods outlined above. They seek to fill in gaps in the capabilities of these methods by, for example, providing intermediate resolution of DNA analytics, generating a protein sensor with "medium-high" power so that slower techniques like MS are less necessary, or further resolving the distinction of various cellular tests.[73,74]

The most promising approach to next-generation biosensors exploit electronic or electrochemical methods to transduce the presence of biomolecules.[29] Electrochemical sensors transduce the presence of an analyte by changes in the faradaic current at a specific electrode. The flagship example is the glucose sensor[75] that oxidizes glucose with a widely available enzyme, glucose oxidase, that creates hydrogen peroxide which is readily reduced by application of a voltage. The amount of redox current correlates to the amount of glucose in blood and has found wide success to treat diabetic patients.[75] Another example is the

alcohol breathalyzer that transduces the oxidation of ethanol in respiration. However, the success of these techniques is largely due to chance of nature rather than engineering brilliance. In both cases, little effort is necessary to minimize spurious signals because the target molecules are uniquely redox active in a certain voltage window. This feature has failed to transfer to the general application of electrochemical strategies to biomolecules like proteins motivating much work in the field to overcome this limitation.[76]

Tailoring the interfacial chemistry of electrochemical sensors engenders greater chemical specificity and corresponding applicability to biomolecules. Intelligent design of the interface ensures the target molecule binds selectively to the electrochemical interface before probing it for redox activity.[76] Nucleic acid aptamers are an extremely promising candidate for target molecules due to their low cost, ease of synthesis, and profound reproducibility.[77–79] These molecules are evolved to specifically bind the analyte of interest with affinities on par with antibodies, a more conventional immunological binding agent. The nucleic acid strands often adopt a stem-loop structure due to self-hybridization that binds the unique structure of the target analyte. Advancements in the field have improved the ad-hoc design of binders to a very systematic and successful approach.[80]

Electrochemical Aptamer-Based sensors (E-AB) are applied to a wide range on analytes,[81] primarily small molecules like illicit drugs and hormones.[31] Their adoption to proteins has been limited to those with small-to-medium molecular weight.[82,83] The aptamer capture agent often adopts a "shape-conforming" transduction motif where the native stem-loop structure is altered to a more diffuse structure when the analyte binds to the aptamer.[31,80] The binding agent is often chemically tagged with a redox active agent

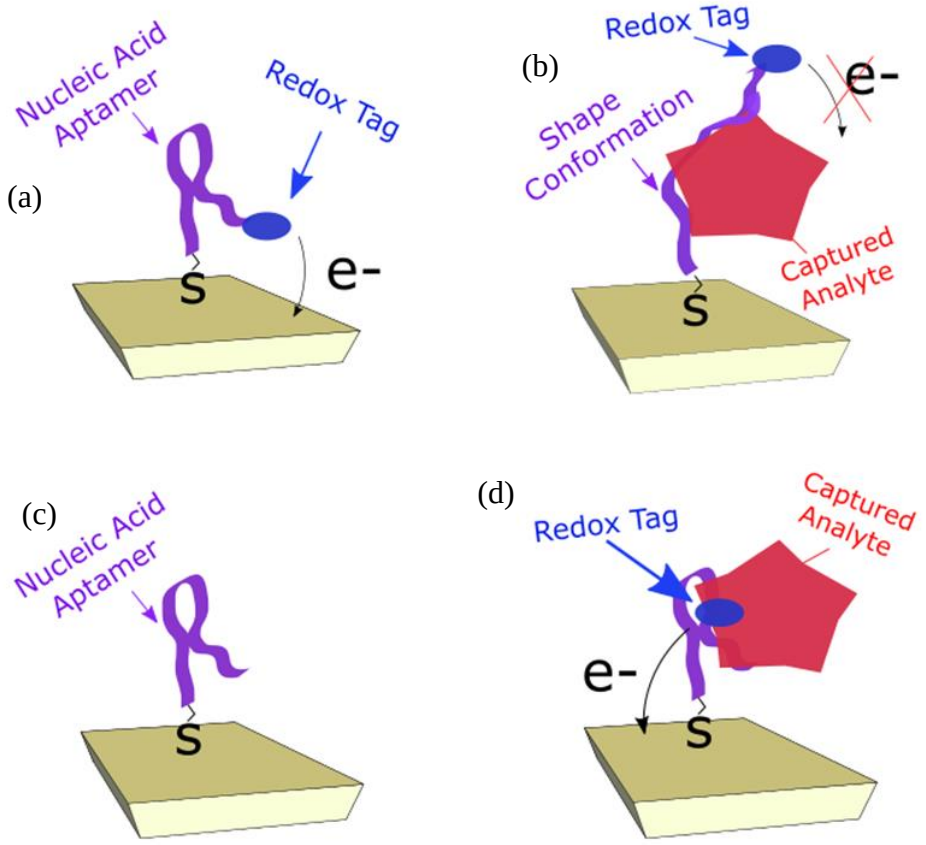

Figure 2.5: Electrochemical Aptamer-Based (E-AB) Sensors.
(a) and (b) demonstrate the mechanism of shape conforming aptamers when used as electrochemical biosensors. The folded aptamer brings the redox tag close to the electrode surface until the target analyte alters the shape and moves it further away. In (c) and (d) a tagged analyte is bound to the surface and the increase in redox current represents successful transduction.

such as methylene blue that yields a faradaic current upon application of a voltage. The electron transfer efficiency is proportional to the measured current and depends strongly on the distance between the redox molecule and the underlying electrode. This mechanism allows for rapid transduction binding events and has been successfully applied to areas such as drug delivery and biomarker monitoring.[84,85] Other variants chemically tag the target analyte with a redox molecule that is in turn concentrated at the electrode interface upon aptamer binding.[86,87] These general schemes are highlighted in Figure 2.5.

Further expansion of electronic sensors exploits the amplification properties of field-effect transistors (FETs) .[15,88] In FET operation, a voltage is applied to a gate electrode (V_G) that alters the conductivity of a semiconductor capacitively coupled through a dielectric layer.[89] An orthogonal drain voltage drives a current through the electrode which is in turn a strong function of the applied gate voltage. Early applications of FETs to sensing were called CHEM-FETs that functionalize an interface with chemical binders.[90] The interface lies between the dielectric layer and an electrolyte medium and perturbs the potential profile through the device.[90] An Ion-Selective FET (ISFET) is another derivate and has been used to indirectly monitor DNA sequencing through pH sensing by tuning the dielectric layer to be chemically sensitive to hydrogen ions.[91,92] The altered chemical potential of the ion-selective membrane is transduced as an altered current in the coupled semiconductor.

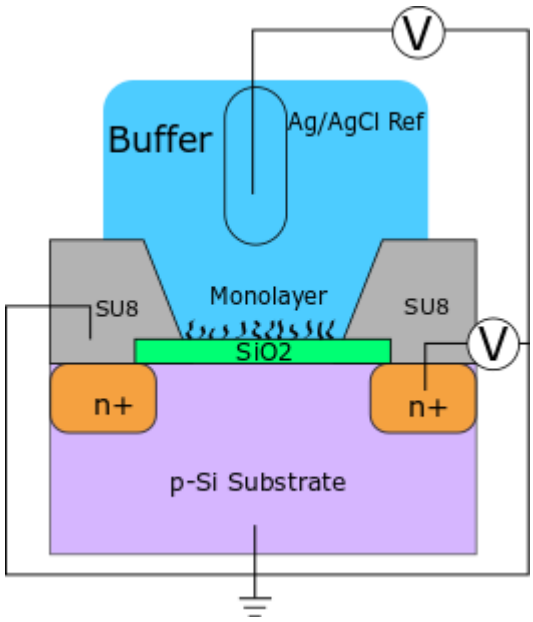

Figure 2.6: Chemical Field Effect Transistors (CHEMFETS).
An inorganic transistor is altered to incorporate a functionalized binding interface that is coupled to a reference electrode through an aqueous electrolyte. Binding at the functionalized interface alters the device characteristic enabling its use as a biosensor.

The two next-generation sensor classes outlined here, electrochemical and transistor, have found ranges of success is various arenas.[88,93] Novel personal care diagnostics are under development with E-AB sensors[84,85] but transistor based monitoring have generally lagged.[77,94] The principle challenges yet to be overcome for transistor biosensors stems from the complicated interactions between transistor operation and biomolecular interactions. This makes it very difficult to precisely correlate altercations in device output to molecular level changes. In terms of sensor merit, it is difficult to make transistor based biosensors with a low limit of detection that can operate in complex chemical or physical environments.[15,23]

2.4 Organic Electronics in Sensing: Methods and Mechanisms

The core of this work is focused on organic electronic based sensors often termed organic bioelectronics.[95] The physical operation of these devices is very similar to conventional, inorganic FETs but with important differences stemming from the material properties.[96] In this context, "organic" implies the materials are carbon-based allowing them to be mechanically flexible and solution processable in direct contrast to conventional inorganic materials like silicon.[10,89] The mechanical flexibility of organic electronics has enabled their adoption as *in situ* biomonitors in, for example, brain implants.[97,98] Monitoring and treatment of epileptic patients has been advanced by the invention of organic electronic based electrodes.[99] Other avenues impacted by electronically functional, mechanically flexible materials are skin prosthetics[100] and robotics[101] where organic electronic films transduce mechanical inputs into an electronic output with a variable form factor.[100,101]

The fundamental building block of organic electronics is the field-effect transistor shown in Figure 2.7 that is analogous to inorganic FETs in Figure 2.6.[96] Similarly, voltages applied to the electrodes govern the conductivity of the semiconducting film. The specific relationship between the input voltages and the output conductivity is a strong function of interfacial properties (highlighted in Figure 2.7) that serve as the target for the construction of bioassays.[14,89,102] The chemical versatility of organic materials enables interfacial

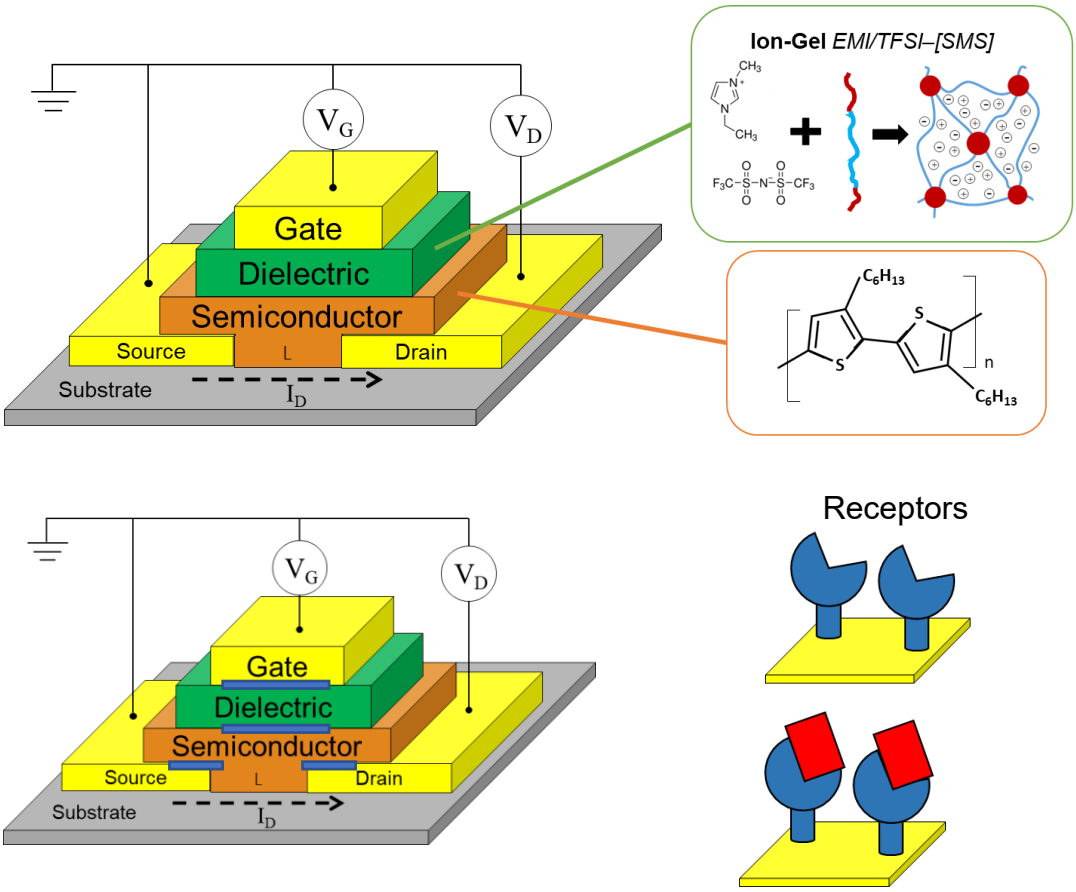

Figure 2.7: Organic Bioelectronic Building Blocks.
An instructive schematic of an organic electronic transistor is shown with a top-gated, bottom contact design. The materials used in the bulk of this work are shown in green and orange. The green dielectric is a combination of an ionic liquid and triblock copolymer termed an ion-gel. The orange semiconductor is a conjugated polymer, P3HT. Interfaces commonly used to fabricate organic electronic biosensors are highlighted in blue and are functionalized with receptors specific for a target analyte.

functionalization with chemical binders that concentrate analyte molecules at said interface.[103] The resulting change in chemistry is transduced by the transistor due to the aforementioned sensitivity of the output conductivity on interfacial chemistry. A spectrum of variations is pursued that functionalize the gate electrode/dielectric interface,[104,105] the semiconductor/dielectric interface,[106] the source/semiconductor interface,[94,107] and the semiconductor/semiconductor interface for films with polycrystalline or amorphous soft matter films.[108–110]

The chemical versality of organic molecules allows for capacitive coupling between the gate electrode with an electrolyte with mobile ions as opposed to solid state dielectrics (e.g. Parylene C or SiO_2).[89] The corresponding material properties of the dielectric layer distinguish important subclasses of organic electronics into electrolyte-gated transistors (EGTs) and conventional organic FETs (oFETs).[89,107] A very promising type of electrolyte dielectric and the major focus of this work is an "ion-gel".[111–113] An ion-gel is a mixture of ionic liquids (non-volatile, liquid organic ions) and triblock copolymers

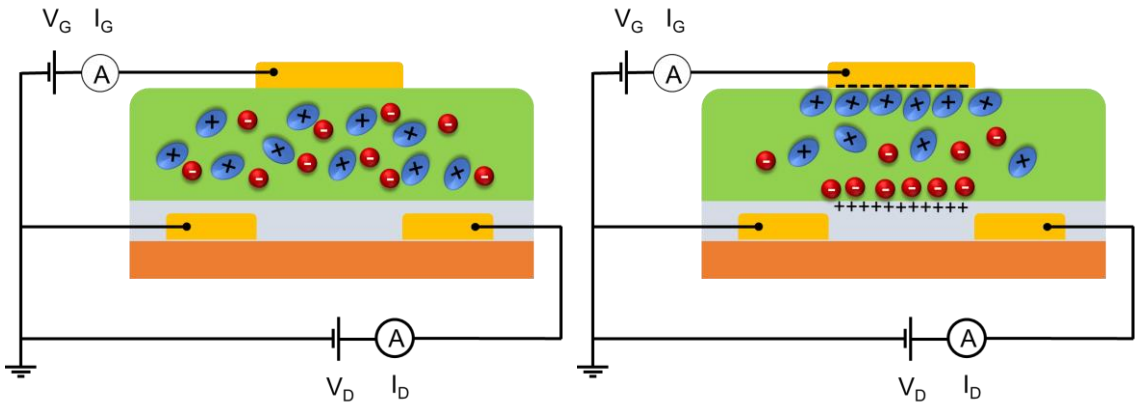

Figure 2.8: Capacitive Mechanism of EGTs.
The mobile ions of the ion gel migrate to the gate electrode and semiconductor interfaces upon application of a voltage. The resulting electric double layers have very high concentration of charge at low applied voltages resulting in a very high electric field due to the thin length of the double layer (~1 nm).

that physically crosslink to enhance the mechanical integrity and processability of the material.[112,113] The electrolyte dielectric contains mobile ions that form electric double layers at the gate and semiconductor interface as outlined in Figure 2.8.[89] The resulting double layers result in very high concentrations of ions and corresponding high interfacial electric fields. This mechanism yields very high capacitances on the order of 1 μF/cm^2 and low voltage operation (<1 V).[89,107] These features are central to adoption in sensing applications that permit facile transduction of small potentiometric perturbations brought by specific changes in interfacial properties.

The semiconducting action of organic materials is dependent on the dielectric used for capacitive coupling and the chemistry of the underlying semiconductor. This work focuses on the polymeric semiconductor, poly(3-hexylthiophene) (P3HT) (Figure 2.7), with a semiconducting action that originates from molecular orbital overlap of adjacent π-π bonds in the polymer backbone.[114–116] Upon application of a gate voltage, the energy levels of these bands are raised until they resonate with the Fermi levels of the underlying

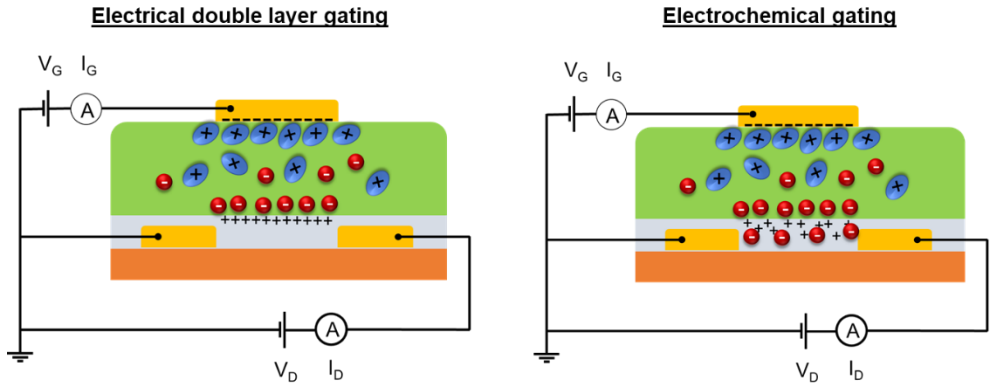

Figure 2.9: Gating Action of Electrolyte Dielectrics on Organics Semiconductors. The interfacial ions in the dielectric can form a two-dimensional double layer in a process termed Electrical Double Layer Gating. In the work presented here, the ions penetrate the semiconductor forming a three-dimensional layer in a process termed Electrochemical Gating.

source/drain electrodes. The resulting carriers can be measured as a drain current upon application of a voltage (V_D) across the film. This current is proportional to the product of the number induced carriers and the speed of those carriers measured by the carrier mobility (μ).[96] The presence of an ion-gel presents unique gating behavior of EGTs. Under a gate voltage, the ions that migrate to the semiconductor/dielectric interface can penetrate the semiconductor and lead to three-dimensional doping.[89] This occurs for polymeric semiconductors like P3HT but not for small molecule crystals and is depicted in Figure 2.9.[117,118] The devices used in this work operate via electrochemical gating yielding very high rations between the ON and OFF current at low applied voltages (~1 V).[6] An archetypal device is shown in Figure 2.10.

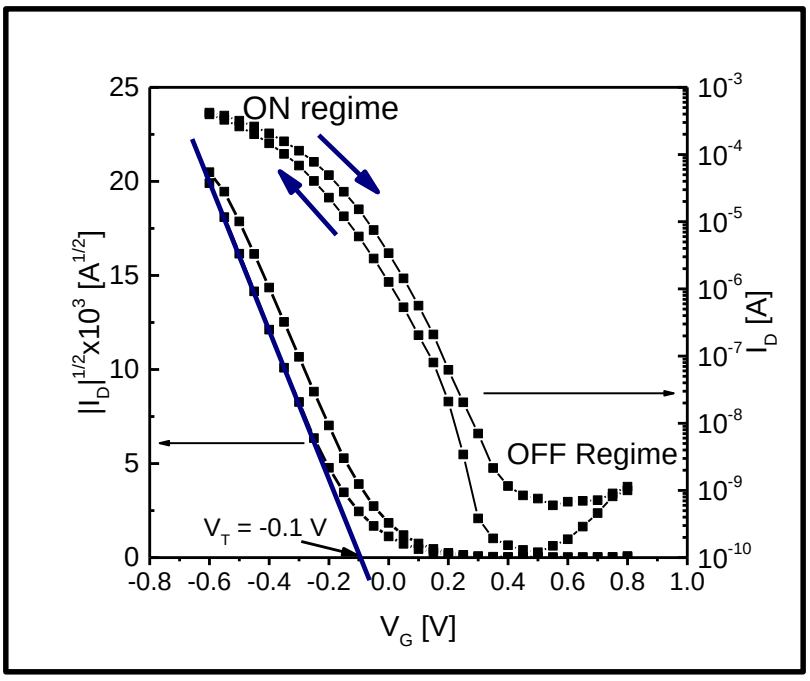

Figure 2.10: Archetypal Device Response of a Printed EGT.
A standard I_D-V_G response of a printed EGT is shown. The current is presented on a semilog plot and a linear plot of $I_D^{1/2}$. The device exhibits ON/OFF ratios of ~10^6 at applied voltages less than 1 V.

Utilizing organic electronic transistors for biosensors is motivated by their printability,[10,119] chemical versatility,[103,120] and corresponding low-voltage operation.[111,121] However, their success has been limited by the inherent material constraints and corresponding applications for which they are qualified. Referring to Figure 2.7, the incorporation of capture molecules on interfaces essential to device operation requires the corresponding chemistry and solvents to be compatible with the electronic materials. Additionally, the voltages necessary to run the device cannot irreversibly breakdown the electrolyte or degrade the semiconductor.[122] The final constraint depends on the strategic choice of the sensing mechanism. If, for example, the binding of the analyte is transduced due to the mirror charge induced onto the semiconductor then the ionic strength of the electrolyte must be very low to prevent masking of the charge screening process.[102]

We introduce a solution by separating the electronics and biocapture interfaces as discussed in the subsequent chapters and corresponding publications.[3–5] The novel geometry and material choice enables a wide range of compatible electrolytes and corresponding analytes to target. The strategy is discussed in detail in Chapters 3-6.

2.5 Methods

A salient feature of organic electronics is their solution processability. The chemistry of carbon based materials enables them to be dissolved in a volatile solution and cast onto a substrate after evaporation.[123,124] In contrast to conventional semiconductor manufacturing, the temperatures are drastically lower (~100^{o}C vs. ~1000^{o}C) requiring far lower energy input. The technique is also additive so that it bypasses the waste and precision required for etching processes. The long-term goal of printed electronic materials

is to generate a fully roll-to-roll (R2R) process that can align and register multiple layers at speeds comparable to conventional printing processes used in, for example, newspaper printing.[124–126]

A variety of techniques are available for printing organic films such as inkjet printing,[127] gravure prinking,[128] or aerosol jet printing.[115,129] Inkjet printing is the most common mode of material transfer and uses a piezoelectric actuator to dispense a small droplet of dissolved organic onto a substrate with precise control over the droplet size and spatial location.[127] It has wide applicability but suffers from clogging problems and limitations on the solvent viscosity.[127] The focus of this work is aerosol jet printing utilizing printers from Optomec Inc. and is depicted in Figure 2.11. The organic electronic material is dissolved in a volatile solvent, aerosolized by a sonication bath, then entrained in an inert carrier gas that is brought near the substrate (~1-3 mm away). Once the entrained aerosols

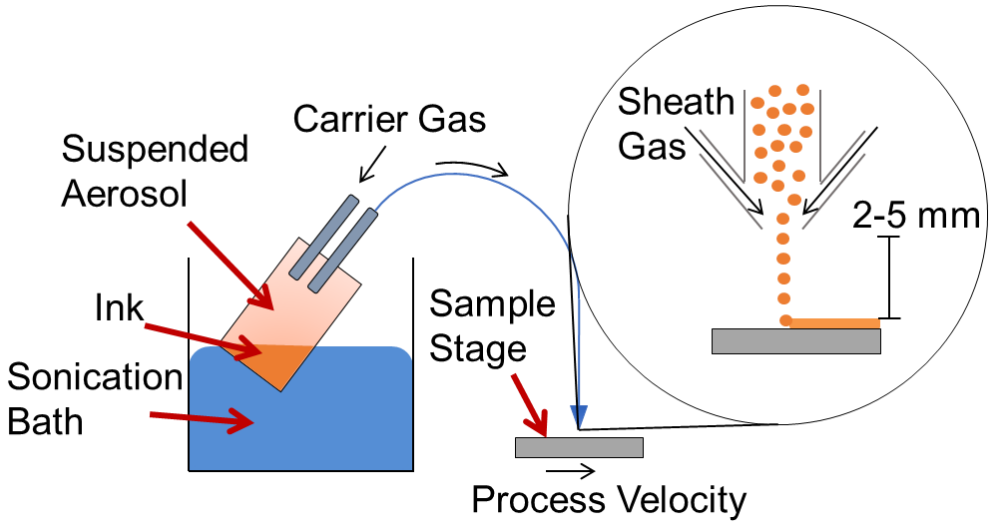

Figure 2.11: Aerosol Jet Printing.
The scheme of aerosol jet printing is demonstrated with an organic ink placed in a sonication bath to form a suspended aerosol. An inert carrier gas is injected to entrain aerosols and deliver them to the nozzle near the substrate. A sheath gas meets the carrier gas at the nozzle and concentrically focuses the aerosol as it is brought to the nozzle.

are brought to the nozzle tip the carrier gas is focused with a concentrically flowing sheath gas to prevent dispersion and spreading of the organic solute leading to spatial resolutions of 15-25 μm. The aerosol jet printing technique is advantageous for this work because it is compatible with a wide range of solvent viscosities, permits rapid prototyping of film geometry, and is flexible to planar and three-dimensional geometries.[115,129]

The methods of printing are provided in detail in the following chapters, but some heuristic guidelines are presented first. The formulation of the ink is constrained by the operating principle of the technique, namely that the solution needs to be volatile enough to form an aerosol but not so volatile it evaporates before the aerosol reaches the nozzle. In the former case, no material will get deposited on the substrate. In the latter case, the solid particulates will get splattered on the substrate erratically with very poor spatial resolution or film uniformity. For example, P3HT can be dissolved in chloroform but the solution is so volatile it does not form uniform films. The addition of a co-solvent like terpineol (1:10 by volume) lowers the volatility of the solvent leading to a solution deposited film on the substrate that, after solution evaporation by heating the stage at 60^{o}C, leaves behind a continuous film of P3HT with good spatial resolution. However, the addition of terpineol lowers the solubility of P3HT and/or leads to agglomeration of the dissolved solids. This process limits the lifetime usability of a P3HT ink dissolved in chloroform/terpineol to about 8 hours. The stage temperature is selected so that it dissolves the ink solvent but does not boil it. For example, a temperature of 60^{o}C is used for chloroform that has a boiling point of boiling point of 61.2^{o}C (note that this is elevated slightly upon addition of terpineol). With a proper ink formulation, the sonicator power is selected in tandem with the physical position of the ink in the sonication bath in order to

generate an aerosol of sufficient density that will be well entrained by the flowing carrier gas. This is a very iterative, empirical procedure that depends on the solution properties, the volume of the ink, and the volume of water in the bath. The goal is to generate as high a density aerosol with the lowest amount of sonicator power. The final parameters are the carrier gas flow rate, the sheath gas flow rate, the working distance of the nozzle to the substrate, and the size of the nozzle. These cannot be tuned independently leading to range of useful parameter sets for a given material. A few guiding heuristics are presented to help orient a new user or an experienced user with a new material. The carrier gas rate needs to be high enough to deliver appreciable solution to the substrate but low enough to prevent over pressuring or excessive amounts of material deposition. The sheath gas flow rate is tied to a given carrier gas. Higher sheath gas flow rates lead to better spatial resolution of the deposited film. But too high rate can again cause overpressures or a sporadic, atomized deposition onto the substrate. The working distance of the nozzle tip to the substrate is generally kept as small as possible (~1 mm). However, some fabrication demands, such as those in this work, require very high working distances closer to ~1 cm. As the aerosol stream travels farther without focusing the resulting film becomes less and less resolved. To compensate for the increased working distance, the flow rates (both carrier and sheath) need to be increased in order to counter the uncontrolled spreading between the nozzle and the substrate. The size of the nozzle is a very critical parameter that in turn affects all the other parameters listed. Smaller nozzle openings lead to larger pressure drops across the orifice requiring higher carrier and sheath gas flow rates. These altered rates also depend on the properties of the aerosol and the working distance of the nozzle. It is best to start a new process with a 150 μm nozzle before constricting it to 100 μm for higher spatial

resolution or expanding it to 200 µm or 250 µm to get larger area coverage at a faster rate. The other operating parameters that lead to successful films at 150 µm are suitable initial iterations for other nozzle sizes. As a final note, the speed and path of the stage moving under the nozzle can be varied completely independently of the flow and solution parameters outlined above. I highly recommend generating a quality film first then programming the computer afterwards. For example, if the resulting film has good resolution and continuity but it too thin then it is best to maintain the flow and aerosol parameters and instead program the stage to slowly print multiple layers over one another. Figure 2.12 shows some optical images of quality film for P3HT, ion-gel, and polystyrene that are used to generate the sensors in this work.

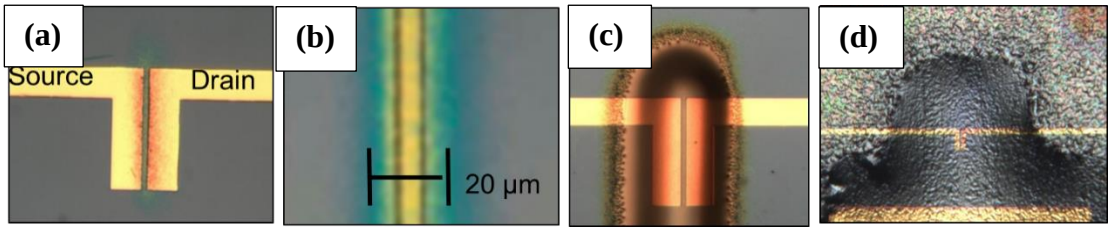

Figure 2.12: Optimal Images of Printed Films.
Printed films of P3HT are shown with a spatial resolution of ~20 µm in (a) and (b). An ion-gel film is shown in (c). An encapsulation layer of polystyrene is shown in (d).

The University of Minnesota is equipped with a stellar cleanroom facility that has enabled the work presented here to succeed. Unlike printing, the procedures outlined in the following chapters can be accurately transferred to other designs or altercations of the design. The gold electrodes are patterned by standard photolithographic methods by coating an oxide wafer with a Shipley photoresist, exposing the film to UV radiation through a chrome mask, dissolving the exposed photoresist in developer, then evaporating a film of chrome followed by gold. The final step strips the photoresist, chrome, and gold

that has not adhered to the exposed oxide. This protocol is useful for patterns with a minimum feature size of ~10 μm.[130]

For higher spatial resolution, a two-layer photoresist process is used with LOR3A deposited first followed by a Shipley resist.[131] Developing the two-layer leads to anisotropic dissolution of the top layer but an isotropic dissolution of the underlying LOR3A. This undercut facilitates the deposition of metals at high spatial resolution so that the interconnects do not unintentionally overlap and cause shorts. The two-layer process generally leads to lower yields due to edge effects compared to the single layer process with lower spatial resolution. As a result, the two-layer photolithography method should only be used when necessary.

The microfluidics used in this work are also fabricated in the cleanroom through soft lithography methods. A film of SU-8 is spin-coated onto silicon wafer to a thickness of ~100-200 μm. The thickness of SU-8 is governed by the spin speed, spin time, and solids content of the SU-8 formulation. Exposure to UV light leads to a highly dense cross-linked network that, after annealing, is not dissolved by SU-8 developing solution. The patterned strips of SU-8 are baked to solidify the film then passivated with HMDS, a hydrophobic molecule that forms a monolayer on the wafer surface. The patterned is transferred to a rubber of poly(dimethyl siloxane) (PDMS) by mixing a solution of base and curing agent named Sylgard® 184 over the pattern and baking for 2 hours at 75ºC.[132,133]

The incorporation of microfluidics and printed electronics to the same photolithographically patterned wafer warrants discussion. The bonding of PDMS to the wafer surface is greatly strengthened by plasma treatment of the corresponding surfaces.

The energetic oxygen molecules in the plasma clean the wafer and PDMS surface from trace organic molecules and increase the surface concentration of hydroxyl groups that permit high integrity surface bonding. Due to this necessity, the PDMS must be bonded to the wafer before printing as the oxygen plasma will detrimentally degrade the printed organic materials. The printing process requires a clean surface that is enabled through plasma treatment, but too much plasma treatment will lead to a large mismatch in surface hydrophobicity between the gold and oxide wafer. As a result, the films for ion-gel depicted in Figure 2.12 will lose their shape due to wicking onto the gold. The complication is bypassed by plasma treating the wafer for a very short time (~10 sec) while the PDMS is treated for a longer time (~30 sec). Then the PDMS can be bonded to the wafer and the organic electronics can be printed with a high working distance of the nozzle.

2.6 Entrepreneurship

I have had the unique experience of pushing my research from the academic sector into the commercialization sector, albeit at a very early stage. The motivations and strategies were developed with help from Dr. Carla Pavone with the Carlson School of Management at the University of Minnesota and a variety of instructors involved in the NSF I-Corps program. The transfer of technology from academia to industry is often challenging due to conflicting motivations between the two sectors. In academia the primary goal is education and knowledge. In industry, to a simple approximation, it is profit.[134]

Straddling these two sectors with a research project requires strategic design of experiments and considerable foresight. Research, by definition, results in advances that are difficult to predict further complicating the transition into the commercialization

sphere. An academic researcher interested in the commercial opportunities of their work is highly advised to begin the commercialization process as early as possible to maintain as much control over the direction as possible.[134]

How does one assess the commercial value of their research? This is a core question that is explored in entrepreneurial courses, books, and experiences. The recommended pathway is outlined in Figure 2.13. Naively, one might consider the top, linear pathway that involves identifying a problem and progressively building the corresponding technological solution with business acumen and capital backing. This strategy works well for large corporations that already have a large, open relationship with their customer base and a strong understanding of their technical capabilities. For an entrepreneur starting-up an endeavor, this fails at extremely high rate. A more intelligent strategy is outline at the bottom of Figure 2.13 that approaches the commercialization problem more

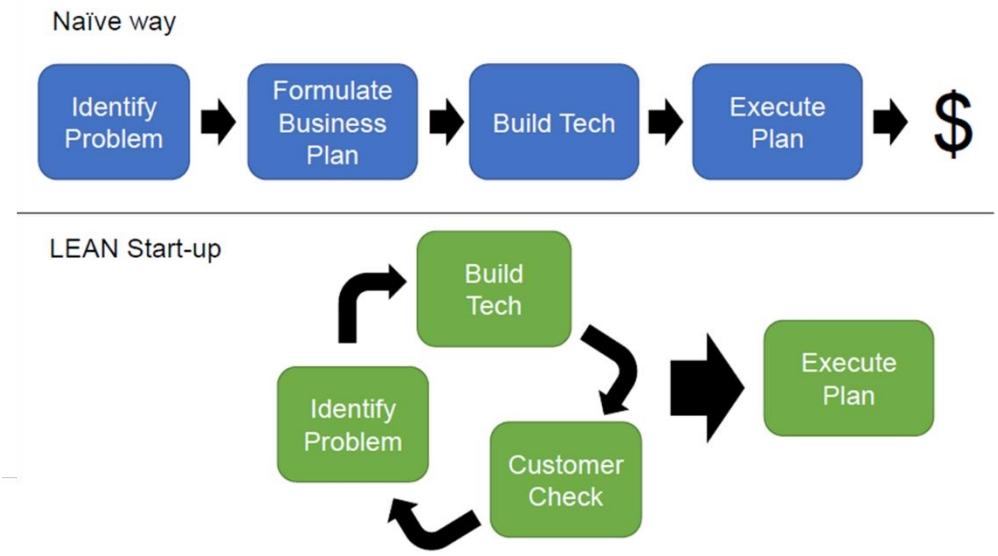

Figure 2.13: Commercialization Pathways.
Two potential pathways for technology commercialization are presented. The blue pathway on top is a linear pathway that works best for established corporations but is very expensive for start-up companies. The more iterative approach in green is far more efficient for start-up companies as it allows the technology to progress with more feedback from potential customers.

experimentally. The process of idea generation and assessment is approached iteratively with the initial problem identified hesitantly. The proposed technological solution is developed with the minimal possible features or capabilities that still permits communication of the final vision of the finished product. This simplified product is tested with real customers and their feedback is used in a continuous process until the technology is ready to sell.[134]

The core mechanism of commercialization is communication with potential customers. This requires translating the technical features of the research project into commercial value of the envisioned product. The Value Proposition (VP) is defined based on the latter definition (i.e. commercial value) and is highly context dependent. VPs constructed from the same vocabulary could have widely different responses to different customer segments (CS). A central goal of the iterative process outlined in Figure 2.13 is to find a match between a given VP and CS resulting in a product market fit. Once the product market fit is found the technology can be advanced to communicate that fit and the potential vision. These technology iterations are termed Minimum Viable Products or MVPs. Chapters 5 and 6 can be thought of as iterative MVPs of the biosensing technology presented in this work.[134]

In short, an aspiring R&D entrepreneur needs to begin the process early and seek out various CS to translate their technical features into a VP. Once successful an MVP can be engineered and developed to deliver the product market fit. The process is repeated until the MVPs transform into an actual product that can be sold for profit. Once enough profit is generated the profit can be used to fund more R&D permitting the cycle to begin again.[134]

3. Label-Free DNA Sensing Platform with Low-Voltage Electrolyte-Gated Transistors

3.1 Abstract

We report a method to measure DNA hybridization potentiometrically in a manner conducive to portable or hand-held biosensors. An electrolyte-gated transistor (EGT) based on poly(3-hexylthiophene) (P3HT) and an ion-gel serves as a transducer for surface hybridization of DNA. The key aspect of the design is the use of a floating-gate electrode functionalized with ssDNA whose potential is determined by both capacitive coupling with a primary, addressable gate electrode and the presence of adsorbed molecules. When DNA is hybridized at the floating gate it offsets the primary gate voltage felt by the P3HT semiconductor; the offset is directly measurable and quantitatively related to the number density of dsDNA molecules. The presented sensing strategy can be readily adapted to other biomolecules of interest and integrated into a microfluidic system for field applications of biosensors.

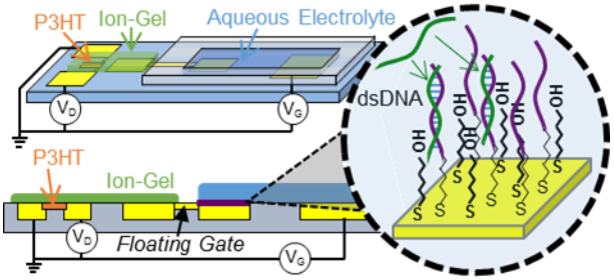

Figure 3.0: Overview Sketch.

3.2 Introduction

Rapid, label-free, and portable DNA detection devices continue to be of interest for applications in biothreat detection[135] or point-of-care diagnostics.[136,137] Key figures of merit for sensors are sensitivity and selectivity but other requirements for portability include robust, simple operation and fast readout.[137–139] Many strategies have been reported including electronic,[140] colorimetric[141] and electrochemical[136] sensing mechanisms. These

approaches avoid the use of fluorescent labels, which is in principle attractive to overall ease of use.

In this article we describe a new potentiometric approach to label-free DNA detection using an electrolyte-gated transistor (EGT) coupled to a microfluidic reservoir. An advantage of using a transistor in a detection scheme is the opportunity for significant signal gain, allowing direct electronic readout of DNA hybridization.[140] As in a conventional field-effect transistor (FET), the current (I_D) through the semiconducting channel of an EGT is a strong function of the voltage applied to the drain electrode (V_D) and the voltage at a capacitively coupled gate electrode (V_G).[142,143] For p-type EGTs, the current is low (or the device is OFF) when $V_G > V_T$ (the threshold voltage) but when $V_G - V_T \approx V_D$ the current follows the saturation behavior[142,144]

$$I_D = \frac{W}{2L} \mu C_i (V_G - V_T)^2 \tag{3.1}$$

where W and L are the width and length of the semiconductor channel, μ is the carrier mobility in the semiconductor, and C_i is the specific capacitance of the gate insulator. EGTs are well suited for potentiometric biosensing[145–147] because of the very large value of C_i, on the order of 10 $\mu F/cm^2$,[142,148] associated with the electrolyte gate "insulator". The large C_i means small changes in V_T, for example due to chemisorption on the gate electrode, result in significant and easily detectable changes in I_D.[138,142,143] In prior work, biocompatible semiconductors such as PEDOT:PSS[149] and carbon nanotubes[150] have been employed in water-gated EGTs where DNA or other analyte molecules interact with the gate electrode in contact with an aqueous electrolyte layer.[151]

The key aspect of this work is the use of a second, floating-gate electrode whose potential (V_F) is not directly controlled. Floating gates have been applied previously in transistor-based DNA sensors.[152,153] However, the use of solid gate dielectrics with lower capacitances limits the change in semiconductor conductance for a given V_T shift arising from DNA hybridization. Our work improves on previous device designs by implementing a floating gate into a high capacitance (or low-voltage) EGT for the first time. The advantages of this sensor architecture are: (1) the pronounced sensitivity due to the extremely large EGT transconductance[154] (dI_D/dV_G, Equation 3.1) i.e., there are large changes in semiconductor conductance for a given potentiometric signal (V_T shift); (2) the low operating voltages that make the devices amenable to a variety of printable, lab-on-a-flexible-substrate schemes;[155] and (3) the versatility of the floating gate design that separates the molecular capture interface from the electronically controlled electrodes.[153]

3.3 Experimental Methods

Materials. The ionic liquid, 1-ethyl-3-methyl imidazolium bis(trifluoromethylsulfonyl)imide (EMI/TFSI) was purchased from EMD Millipore, Inc. (high purity). Poly(3-hexylthiophene) was purchased from Rieke Metals Inc. (MW = 50-70k, regioregular, electronic grade). The block copolymer poly(styrene-b-methyl methacrylate-b-styrene) (SMS) (MW = 15k-81k-15k) was used to create the ion-gel and synthesized by the procedure outlined by Zhang *et* al.[156] All DNA was purchased from Integrated DNA Technologies with the sequences in Table 3.1. The highlighted nucleotides represent the location of non-complementary base pairs with respect to the probe sequence. Beta-Mercapto Hexanol was purchased from Sigma-Aldrich and used as received. YOYO-

1 dye was purchased from Invitrogen. TE buffer was used to store and transport DNA (10 mM Tris, 1 mM EDTA, pH = 8.0) and phosphate buffered saline (PBS 1x) was used as an aqueous electrolyte during device testing.

Table 3.1: DNA Sequences

Name	Sequence
Probes	5'-GAG-AGA-CCG-GCG-CAC-AGA-GG-3'
COMP	3'-CTC-TCT-GGC-CGC-GTG-TCT-CC-5'
MM1	3'-CTC-TCT-GGC-**A**GC-GTG-TCT-CC-5'
MM2	3'-CTC-TC**G**-GGC-CGC-GT**T**-TCT-CC-5'
MM3	3'-CTC-TC**G**-GGC-**A**GC-GT**T**-TCT-CC-5'
RAND	3'-C**GT**-**AAA**-**T**G**A**-**TC**C-**T**T**C**-**AAC**-**TA**-5'

Device Fabrication. The P3HT and ion-gel were deposited with an aerosol jet printer from Optomec Inc. P3HT was dissolved in chloroform (1 mg/mL) then terpineol was added (1:10 by volume) as a co-solvent. The ionic liquid was mixed with SMS and ethyl acetate at a ratio of 1:9:90 by weight (EMIM/TFSI:SMS:ethyl acetate). Experimental parameters and procedures for the printing process can be found in the article by Kim *et al.*[144] The device was annealed as fabricated at 120^{o}C for 30 min. A PDMS well was then reversibly bonded (i.e., without plasma treatment) to the device. In terms of areas, the semiconductor footprint was 0.11 mm x 0.2 mm (A_{SC}), the floating-gate/ion-gel interface was 1 mm x 1 mm (A_{FG1}), the floating-gate/aqueous interface was 3 mm x 3 mm (A_{FG2}), and the primary gate/aqueous interface was 5 mm x 5 mm (A_{G}).

DNA Handling. All DNA was stored in TE buffer at 100 μM. To immobilize the thiol-modified probes, they were first reduced with dithiothreitol (DTT) (Sigma-Aldrich) and then purified via chromatography and diluted to 1 μM with TE buffer containing NaCl. To immobilize probes at a low density (2 pmol/cm^2)

they were spotted onto the floating gate electrode in TE buffer at 0.1 M NaCl for 2 h; for medium density (7 pmol/cm^2) they were spotted in TE buffer at 1.0 M NaCl for 2 h; for high density (12 pmol/cm^2) they were spotted in TE buffer at 1.0 M NaCl for 24 h.[157] The samples were then rinsed with TE buffer (no NaCl) and then spotted with 1 mM Beta Mercapto Hexanol (MCH) in DI water for 1 h and rinsed with TE buffer. Complementary, mismatched or random DNA were then added at 1 μM (or as specified for complementary DNA) in TE buffer at 1.0 M NaCl for 1 h and rinsed with TE buffer. All electrical measurements were carried out with PBS 1x connecting the floating gate and gate electrodes. For fluorescent measurements, the samples were immersed in a YOYO-1 solution diluted to 100 nM with TE buffer overnight (≥12 h).

Equipment. All electrical measurements were performed with a Keithley 2400 Source Measure Unit connected to the gate electrode, a Keithley 2611B Source Measure Unit connected to the drain electrode, and a Keithley 6517A Electrometer connected to the source electrode. DNA probes were purified with a QiaGen oligonucleotide clean-up kit. DNA concentrations were verified with a Thermo Scientific NanoDrop 2000c UV-Vis Spectrophotometer. Fluorescent images were taken with an inverted epifluorescence microscope (Leica DMI 4000B) with a 120 W metal halide light source. Electrical Impedance Spectroscopy measurements were performed with an HP 4192a Impedance Analyzer.

3.4 Results

Figure 3.1 shows the device architecture and overall detection strategy. The floating gate straddles two separate portions of the sensor: (1) the detection reservoir (right arm) filled with aqueous buffer where the target DNA is introduced and binds to the floating gate and (2) the EGT transducer (left arm) which converts the DNA hybridization event to an electrical signal. The EGT consists of a printed polymer semiconductor (poly(3-hexylthiophene) or P3HT) connecting source and drain electrodes and an ion-gel electrolyte[8,16,19] that couples the semiconductor and the left arm of the floating gate. The ion gel is favorable to other electrolytes due to its chemical compatibility with P3HT. Applying a voltage directly to the floating gate (which is in this case no longer floating), as illustrated in Figure 3.1a, modulates the conductance of the polymer semiconductor, which can be measured directly as a change in drain current (following Equation 3.1) as shown in Figure 3.2 (black curve). However, during normal operation of the floating-gate EGT, voltages are not applied directly to the floating gate. Instead, a second electrode, the primary gate, is used to control the EGT through capacitive coupling with the floating gate via the aqueous buffer, as shown in Figure 3.1b. The primary gate is connected to the P3HT channel through the floating gate, i.e. the two gates are in series. Therefore, chemical events at the surface of the floating gate result in V_T shifts as discussed below. This design allows the surface capture chemistry to occur in a separate electrolyte from the transistor, minimizing contamination and/or degradation of the device.

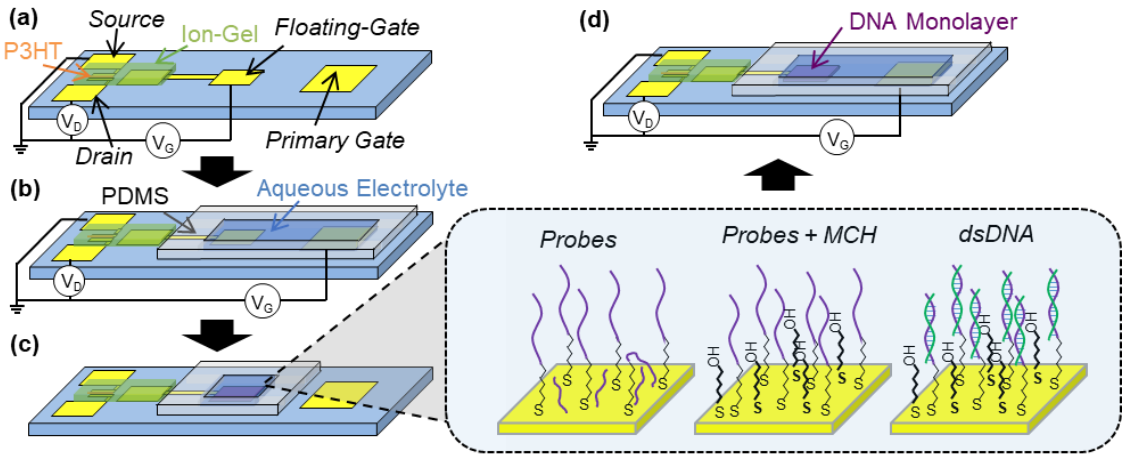

Figure 3.1: DNA Detection Scheme.
(a) The electronic materials are printed on a patterned silicon wafer then tested in a side-gated architecture. **(b)** The floating-gate EGT is tested by connecting the floating gate to the primary gate with phosphate buffered saline (PBS 1x). **(c)** The floating gate is selectively reacted with ssDNA probes, beta mercapto hexanol (MCH), and complementary/mismatched/random DNA. **(d)** The change in threshold voltage (V_T) is recorded by testing the EGT before and after probes are reacted with DNA.

Figure 3.2 demonstrates that sweeping V_G negatively turns the EGT ON (i.e., the source-drain hole current increases[142]) whether the device is tested in the Figure 3.1a (black curve) or 3.1b (red curve) configuration. This happens because the application of V_G to the primary gate equivalently biases the floating gate, V_F, because of capacitive coupling. The current at the gate electrode (I_G) is also not altered between the configurations (Figure S3.1, Supporting Information). Importantly, Figure 3.2 shows that, with no chemisorption on the floating gate, V_T is independent of whether the gate bias is applied directly to the floating gate or to the primary gate.

To complete the sensor, surface immobilization of ssDNA, the capture sequence, was carried out on a portion of the floating gate with thiol-modified DNA probes[157,158] as shown in Figure 3.1c. A blocking layer MCH was also adsorbed after probe immobilization to displace non-specifically adsorbed probes and to prevent further adsorption of

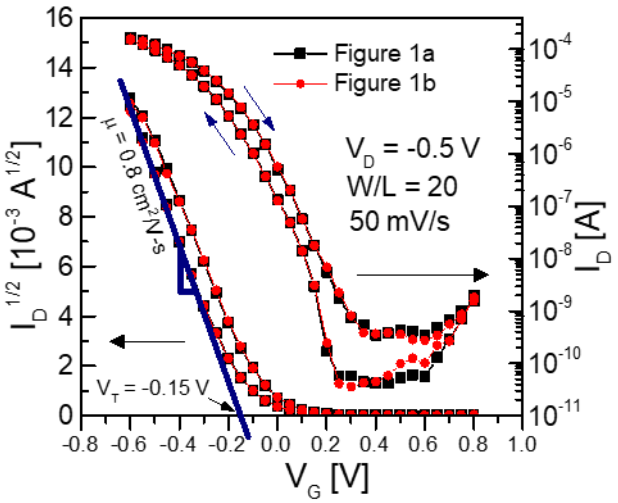

Figure 3.2: Floating-Gate Operation.
Testing the device in two different geometries (Figure 3.1a vs. Figure 3.1b) does not alter the I_D-V_G characteristics of the side-gated EGT because the potential at the floating-gate electrode (V_F) is dominated by the primary gate electrode (V_G).

oligonucleotides.[157–159] To operate the sensor, the device was configured as shown in Figure 3.1d where the aqueous buffer covered the functionalized pad of the floating gate and the primary gate. The resulting transfer curve colored red in Figure 3.3a was shifted positively from the curves in Figure 3.2 (i.e., before chemisorption) and was taken as the background signal. Exposure of complementary DNA to the immobilized ssDNA, accomplished in the Figure 3.1c configuration, resulted in the formation of dsDNA on the floating gate as confirmed by fluorescence microscopy (Figure 3.7, Supporting Information).[160] Importantly, as shown in Figure 3.3b, the formation of dsDNA on the floating gate resulted in a significant -120 mV shift in the I_D-V_G characteristic of the EGT when it was re-tested in the Figure 3.1d configuration. Exposure of random DNA to the sensor exhibited a much smaller <10 mV shift. The size of the voltage shift was a function of ssDNA surface density.[157,161] A moderate probe density (7 pmol/cm^2) was used because it exhibited a large signal (inset Figure 3.3b) while avoiding non-idealities associated with densely packed DNA probes.[157,161]

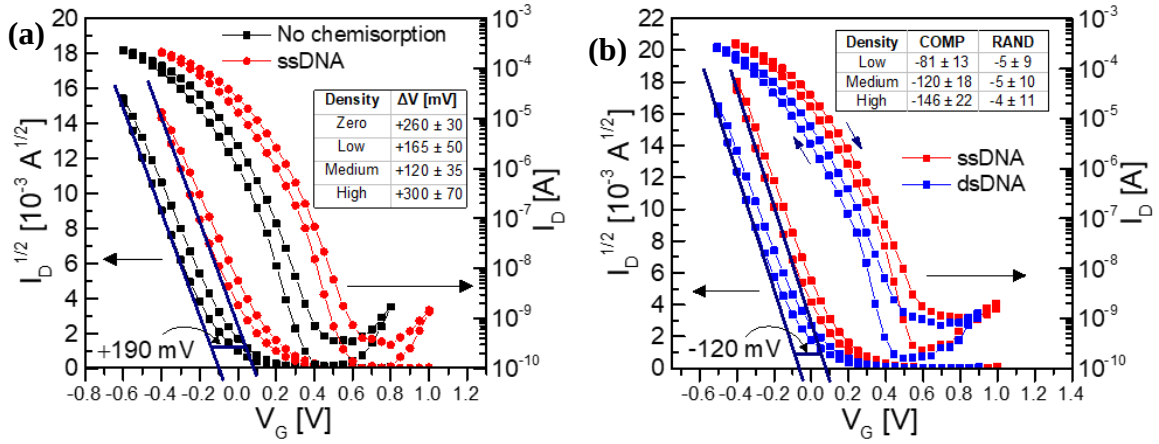

Figure 3.3: Sensor Response to Surface Functionalization.
(a) Testing the device after chemisorption of DNA probes (red) positively shifts the transfer curve with respect to that taken before chemisorption (black). The inset shows the magnitude of the shift at different densities of ssDNA probes with zero corresponding to only MCH. Error is the standard deviation of 20-30 devices. **(b)** The formation of dsDNA on the functionalized floating gate electrode causes the transfer curve (blue) to shift negatively from the one taken with ssDNA (red). The inset shows a table of ΔV from complementary and random DNA at different probe densities. The error is the standard deviation of 10 devices.

The sensitivity of the floating-gate EGT was demonstrated by varying the concentration of target ssDNA exposed to the sensor from 10 nM to 10 μM. Measurements were taken at steady-state by increasing the hybridization time for lower concentrations ($\tau \sim 1/k_{on}C_{DNA}$, $k_{on} \sim 10^4$ $M^{-1}s^{-1}$).[157,162] The results in Figure 3.4a show that the signal is saturated at high concentration (≥ 1 μM) but steadily declines for lower concentrations. The data are well fit by a Langmuir isotherm ($\nu = C_{DNA}/(C_{DNA} + K_D)$) with K_D = 25 nM by assuming the ΔV decreases due to the smaller fraction of the surface converted to dsDNA ($\nu = \Delta V/\Delta V_0$).[161,162] The limit of detection for this configuration is 10 nM, assuming a background level equal to the signal from adding random DNA (<15 mV). The intrinsic background is caused by a combination of EGT instability,[144] non-specific adsorption of DNA,[158] and drifting potentials of the primary gate electrode.[163] The sensitivity can be improved significantly by incorporation of a reference EGT into the sensor,[163] which will

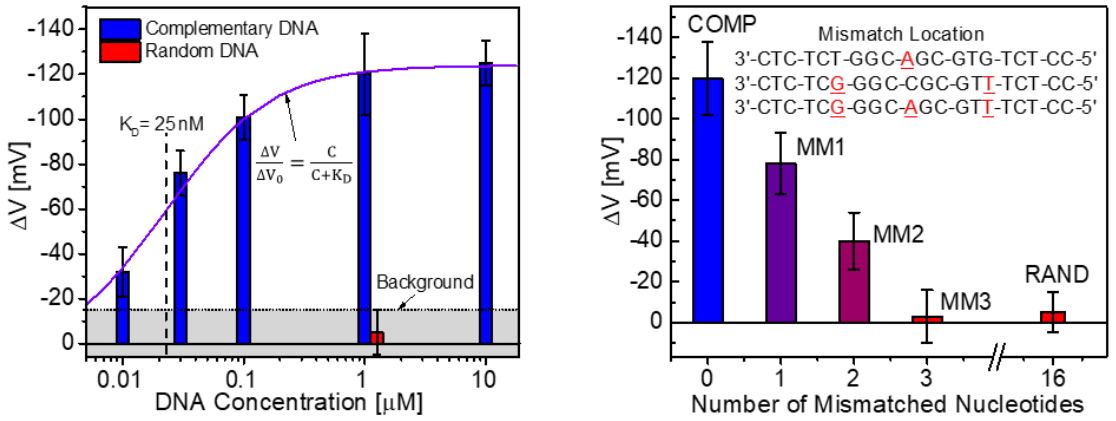

Figure 3.4: Sensitivity and Selectivity.
(a) The sensitivity of the sensor (Figure 3.1d configuration) was tested by varying the concentration of complementary DNA and the response is well fit by a Langmuir isotherm. The background level is defined as the sensor response to random DNA. **(b)** Mismatched DNA sequences diminish the shift of transfer curves (DV) and 3 mismatches are indistinguishable from a completely random sequence. Error bars are the standard deviation of ≥5 devices.

be a focus of future work. For nucleic acids with different binding strengths, the tests can be performed in triplicate with a positive control (target DNA at high concentration), a negative control (random DNA), and the test sample all measured in parallel.

The selectivity of the sensor was measured by varying the sequence of target ssDNA in solution. The number of mismatched base pairs was increased until the signal was indistinguishable from a random sequence. Figure 3.4b demonstrates that there is a measurable difference in V_T for a sequence with only 1 mismatched base pair and as few as 3 mismatched base pairs exhibit responses indistinguishable from a fully random sequence.

3.5 Discussion

The operation of a floating gate EGT can be understood by approximating the device as a network of series capacitors with each capacitor representing a double-layer at an electrode/electrolyte interface (schematic in Figure 3.5). This model is valid under the following assumptions: (1) zero gate-source current; (2) the semiconductor is held at ground; (3) constant capacitance values. The capacitors in the aqueous electrolyte can be combined ($1/C_{Total} = 1/C_1 + 1/C_2$) to define C_G and those in the ion-gel to define $C_{SC,}$ which physically represent the capacitive coupling between the floating gate/primary gate and the floating-gate/semiconductor channel. With capacitors in series, the total charge separated in the network is equal to the total charge separated on each individual capacitor by a charge balance,

$$Q_F = Q_{Total} \tag{3.2}$$

where Q_{Total} is the total charge separated in the device and Q_F is the total charge separated on the capacitor between the semiconductor channel and the floating-gate electrode (C_{SC}). Substituting in the definition of capacitance ($Q = CV$) and writing the total capacitance as a series combination of C_{SC} and C_G ($1/C_{Total} = 1/C_{SC} + 1/C_G$) results in

$$C_{SC}V_F = \frac{C_{SC}C_G}{C_{SC}+C_G}V_G \tag{3.3}$$

Solving for V_F in terms of V_G gives

$$V_F = \frac{C_G}{C_{SC}+C_G}V_G \tag{3.4}$$

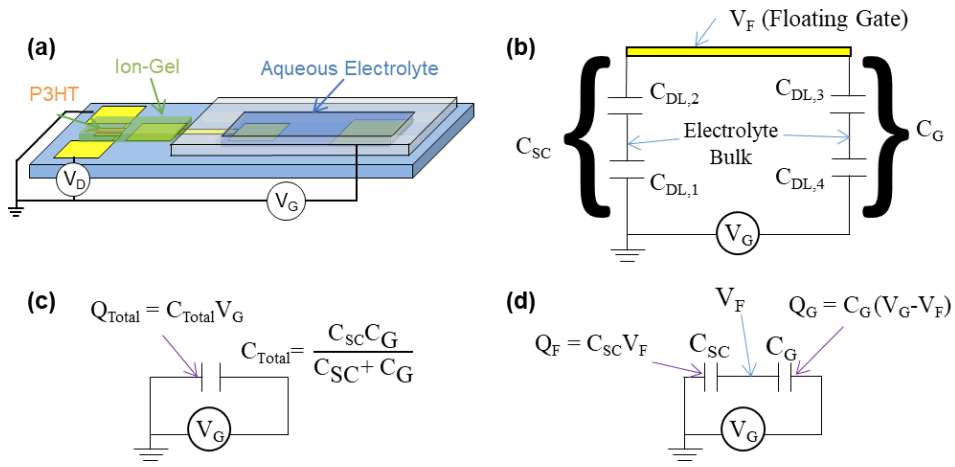

Figure 3.5: Floating Gate EGT Circuit.
The schematic of a floating-gate EGT in **(a)** can be approximated as the equivalent circuit shown in **(b)** where the capacitors represent electric double layers and the nodes represent electrodes or electrolyte bulks. **(c)** is the equivalent circuit when C_G and C_{SC} are combined into C_{Total}. **(d)** is another equivalent circuit where C_{Total} is separated into C_G and C_{SC} each immobilizing an equal amount of charge ($Q_F = Q_G = Q_{Total}$).

which demonstrates that V_F tracks V_G if $C_G >> C_{SC}$ or the capacitive coupling between the floating gate and primary gate dominates. In this work, $C_G/C_{SC} \approx 20$ (Figure 3.6) yielding the result presented in Figure 3.2.The sensing action of the device is achieved through selective modification of the floating gate/aqueous electrolyte interface with DNA, creating a voltage offset[153,164] between the floating gate and the primary gate. DNA hybridization alters the effective double layer potential created at the floating gate/aqueous interface[149] requiring a more negative V_G on the primary gate to turn the EGT ON, as observed in Figure 3.3b. Mathematically, we account for this voltage offset by treating it as a correction ΔV to the threshold voltage for the I_D-V_G characteristics in the saturation regime,

$$I_D = \frac{W}{2L}\mu C_i\left(V_G - [V_T + \Delta V]\right)^2 \qquad (3.5)$$

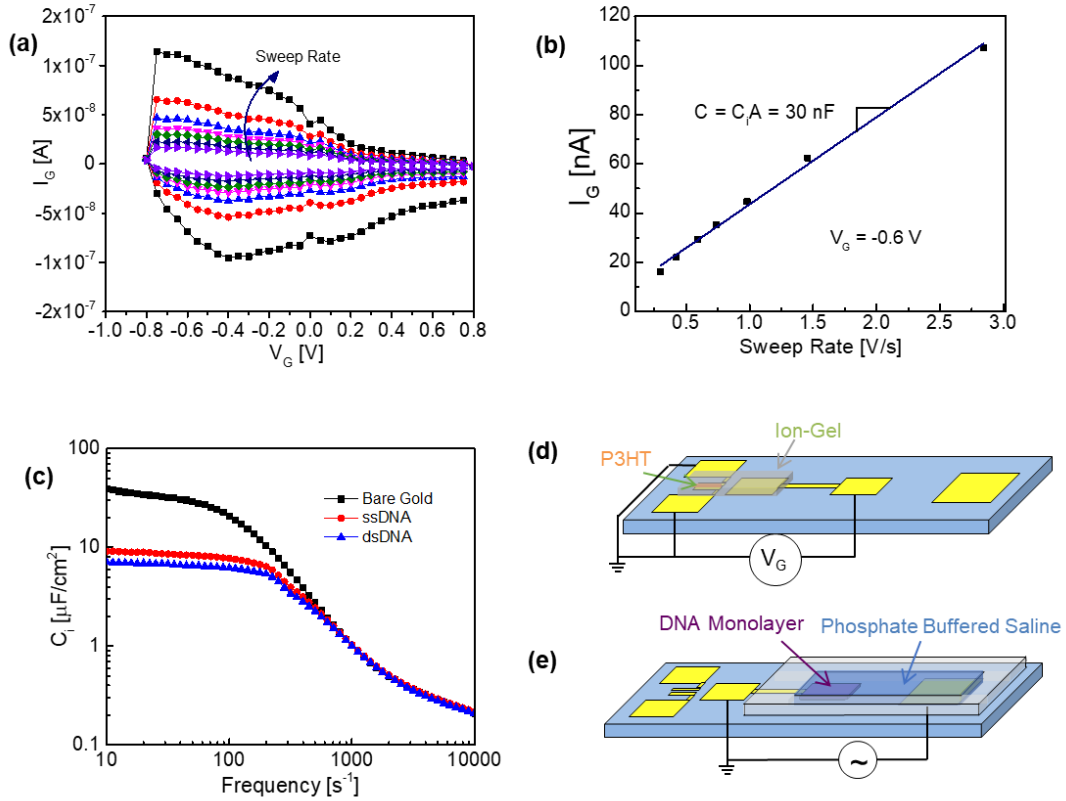

Figure 3.6: Capacitance Measurements.
In **(a)**, the displacement current of the side-gated EGT is presented at various sweep rates then plotted in **(b)** with a linear fit to extract the total capacitance of the EGT. Measurements on 7 devices give C_{SC} = 30 ± 9 nF (C_i = 135 µF/cm^2 for A_{SC} = 0.11 mm x 0.20 mm). In **(c)**, electrical impedance spectroscopy of DNA monolayers in phosphate buffered saline (PBS 1x) show a decrease in capacitance with DNA hybridization. Measurements on 5 devices give C_G = 670 ± 10 nF for ssDNA + MCH and 520 ± 50 nF for dsDNA + MCH (C_i = 9.1 and 7.0 µF/cm^2). Resulting in $C_G/C_{SC} \approx 20$. **(d)** shows the testing configuration for displacement current measurements in **(a)** and **(b)**. **(e)** shows the testing configuration for Electrical Impedance Spectroscopy in **(c)**.

where $\Delta V = V_G - V_F$ and is due to adsorbed molecules.

In Figures 3.3 and 3.4, negative shifts in V_T occur when ssDNA is hybridized to dsDNA. This binding event brings about a number of changes in electrical properties of the immobilized molecule such as dipole orientation, increased conductivity, polarizability,

and negative charge.[165–167] To date, floating-gate transistors have differentiated ssDNA and dsDNA by using the increase in negative charge on the floating gate to electrostatically shift the potential of the coupled semiconductor ($\Delta V \approx Q_{DNA}/C$).[153,164,168] However, applying this model to our device predicts an increase in I_D at a given V_G in contrast to the result seen in Figure 3.3b. That is, the charge model predicts a positive V_T shift upon hybridization, whereas Figure 3.3b indicates a negative shift. Additionally, the high ionic strength of the aqueous electrolyte yields a Debye length of ~1 nm which effectively screens negative charge on the DNA backbone. Thus, it appears that simply considering the charge of duplex DNA is not sufficient to describe the sensor mechanism.

Instead, we consider the potential on the floating gate, V_F. Hybridization to make dsDNA at the floating gate/aqueous interface reduces C_G (Figure 3.7) and thus the coupling between the floating gate and the primary gate, i.e., $V_F < V_G$ at any given V_G.[153,169–171] This condition produces the observed negative shift in V_G, but does not adequately account for the magnitude of the shifts. The causes of a decrease in C_G upon hybridization are related to the increase in thickness of an adsorbed DNA monolayer that impedes ion penetration into the DNA layer and, in turn, the double-layer capacitance.[169–171]

Another factor to consider is the surface dipole at the floating-gate/aqueous interface and the corresponding changes in electronic energy levels due to adsorbed molecules. The formation of gold/thiol bonds due to probe and MCH immobilization (Figure 3.3a) results in a bond dipole with the negative side oriented towards the gold substrate.[172] Since the floating gate is embedded in the sensor circuit between the primary gate and EGT transducer, this charge separation may effectively bias the floating gate with

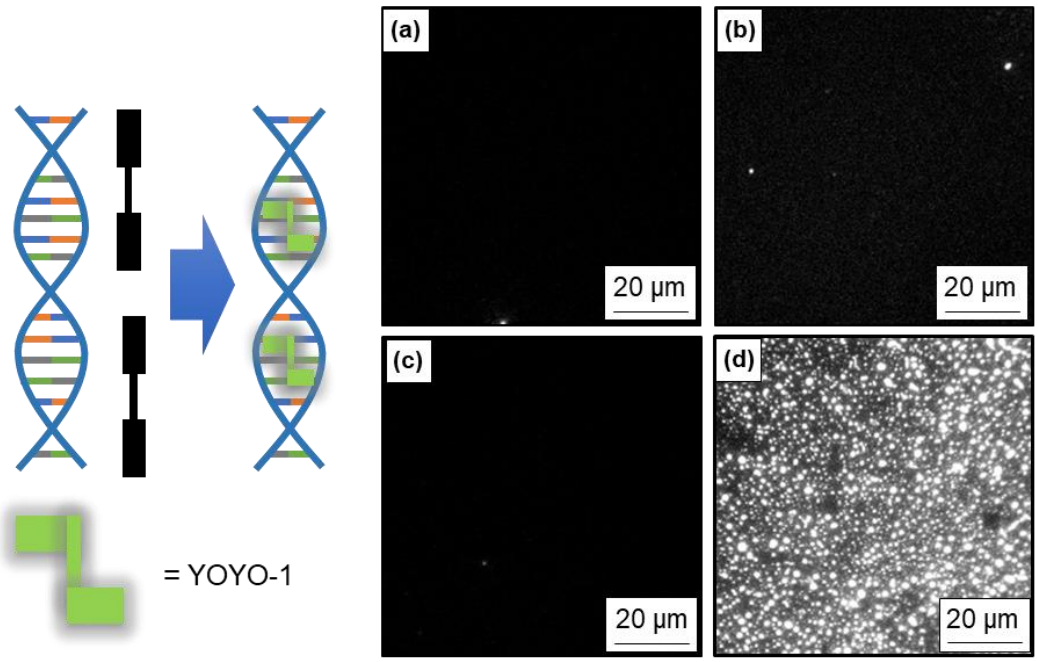

Figure 3.7: Confirmation of Surface Hybridization.
YOYO-1 dye was used to generate fluorescent images of functionalized gold substrates. Samples were immersed in YOYO-1 which is a bisintercalating dye that exhibits a ~1000 increase in fluoresence when in the presence of dsDNA. **(a)** is a bare gold substrate, **(b)** is a sample functionalized with a medium density of probes and MCH, **(c)** has probes which were exposed to random DNA, and **(d)** has probes exposed to complementary DNA resulting in a drastic increase in fluorescence.

respect to the primary gate shifting the V_T in the coupled EGT. It is then plausible that DNA hybridization would alter this surface dipole resulting in a different offset than the one with ssDNA. However, more work is required to confidently attribute both the magnitude and direction of the observed V_T shifts to the complex molecular changes between ssDNA and dsDNA. Also, the dependence on experimental parameters such as ionic strength will be optimized for detection of small dsDNA coverages. Lower ionic strengths may render the device more sensitive to changes in surface potential but may also decrease electrode stability or increase potential drops due parasitic capacitance (diminished C_G/C_{SC}).

The pronounced selectivity to mismatched sequences may also be understood as a combination of the mentioned effects. On a molecular level, the complex formed between DNA probes and a mismatched sequence carries the same nominal charge as purely dsDNA.[173] However, the geometry and orientation of mismatched DNA differs from perfectly complementary DNA.[174–176] Additionally, the mismatched sequences may exhibit a smaller equilibrium coverage[162,177] on the floating gate. Both diminished coverage and the different geometry associated with mismatched dsDNA may lead to a smaller change in C_G upon hybridization, or a smaller change in surface dipole compared to complementary dsDNA, and thus a smaller negative V_T shift, as observed (Figure 3.4b). Again, further research is necessary to understand the precise origin of the signal associated with mismatched DNA, but the sensitivity to base mismatches depicted in Figure 3.4b is a salient advantage of this label-free, electronic approach to measuring DNA hybridization.[136,166,178]

3.6 Conclusions

Implementing a floating-gate electrode into a low-voltage EGT allows surface bio-recognition events to be recorded as an altered conductivity of the coupled organic semiconductor. The advantages of the sensor design are the lack of labeling reagents, the electronic readout, and selectivity.[136,138,179] Additionally, the strategy can be readily multiplexed into an array of sensors that are connected with a microfluidic network.[180] Ongoing work aims to enhance the limit of detection and to minimize the large amount of solution (100 µL) required to fully functionalize the electrode. These limitations can be alleviated through optimization of the circuit design and microfluidic handling of the sample, both of which follow directly from established techniques.[163,181–183]

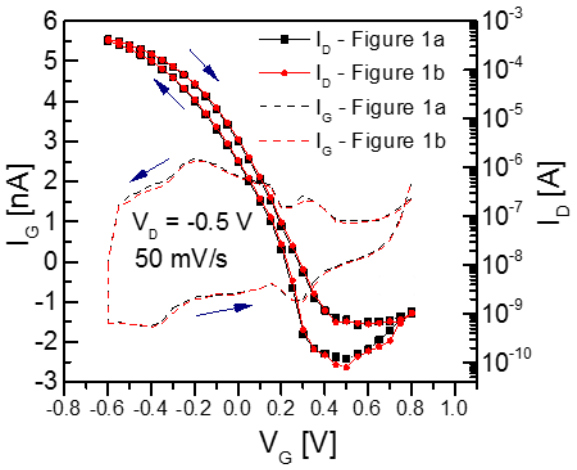

Figure S3.1: Floating-Gate Operation.
The drain current and gate current of the EGT are not altered when the device is tested in the floating-gate architecture. Solid lines represent the I_D-V_G curve while dashed lines represent I_G-V_G curves.

3.7 Supporting Information

The planar, side-gated architecture and electrolyte materials allow the device to be tested with and without a floating-gate. There is no observed difference in I_D-V_G or I_G-V_G characteristics since the capacitance at the aqueous interfaces are much larger than the ion-gel interfaces ($C_G >> C_{SC}$).

For this work, the area of the ion-gel/floating-gate interface was 1mm x 1mm; the floating-gate/aqueous interface was 3mm x 3mm; and the primary gate electrode was 5mm x 5mm. These areas yield a $C_{SC} \approx 30$ nF and $C_G \approx 1000$ nF before chemisorption.

Acknowledgements: The authors acknowledge several funding sources including the National Science Foundation (Predoctoral Fellowship for SPW), the Office of Naval Research through the Multi-University Research Initiative (CDF) and the David and Lucile Packard Foundation (KDD). A portion of this work was performed at the University of Minnesota Nano Center, which received partial support from the NSF through NNIN.

4. Operating and Sensing Mechanism of Electrolyte-Gated Transistors with Floating Gates: Building a Platform for Amplified Biodetection

4.1 Abstract

Electrolyte-gated transistors (EGTs) with floating gates (FGs) are an emerging platform for label-free electronic biodetection. Advantages of floating-gate EGTs (FGTs) include signal amplification and inherent sensitivity to small voltages, on the order of 10 mV, associated with chemical binding events on the floating gate electrode surface. Here we examine how the performance of these devices depends on their architecture, specifically the relative sizes (areas) of the control gate, the floating gate, and the source-semiconductor-drain channel. The results allow optimization of the geometry for future biodetection studies. Further, using self-assembled monolayer (SAM) chemistry, we also examine the effect of chemisorption on the floating gate on the current voltage (I-V) characteristics. We find the FGTs respond to both interfacial dipoles and capacitance changes and that the I-V behavior can be reasonably predicted with a lumped capacitor model. Overall, this work provides the most detailed picture to date of the operating mechanism of these promising electronic sensing devices.

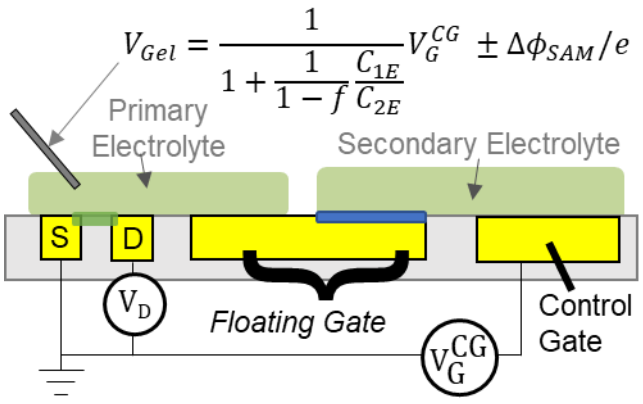

Figure 4.0: Overview Sketch.

4.2 Introduction.

Originally developed in the 1980s, electrolyte-gated transistors (EGTs) are re-emerging as a promising platform for biosensing.[184–187] In these devices, an electrolyte serves as the high capacitance "gate insulator" between the gate electrode and the semiconductor channel (Figure 4.1a-c).[188] Application of a voltage to the gate results in polarization of the electrolyte and an increase in the conductivity of the semiconductor channel due to electrochemical doping or electric double layer charging.[187] This effect can be the basis of bioelectric signal amplification, as has been demonstrated recently for brain wave monitoring.[189,190] Alternatively, by modification of the semiconductor with selective chemical receptors, EGTs can function as label-free biosensors in which chemical binding events result in large changes in channel conductivity.[191] Advantages of EGTs for sensing include signal amplification typical of transistors (e.g. 'chemFETs')[192–195] and inherent sensitivity to small voltages.[196] In particular, due to the very large capacitances associated with electrolyte interfaces, EGTs typically transition from low conductance OFF to high conductance ON states over voltage ranges as small as several hundred millivolts,[187,188] making them exquisitely sensitive to the surface chemistry of the semiconductor.[191,197]

Here we focus on an alternative EGT architecture in which a floating gate electrode is introduced (Figures 4.1d-f). For sensing applications, floating gate EGTs (FGTs) have the advantage that the semiconductor does not need to be modified with selective receptor molecules and it is not put in contact with the target-containing sample fluid.[198,199] Instead, the receptors are located on the right arm of the floating gate in a secondary electrolyte compartment that is entirely separate from the primary electrolyte in contact with the semiconductor.[200] The shift of the molecular "capture surface" from the semiconductor to

the floating gate provides two principal avenues for device optimization. First, the semiconductor can be selected simply based on its electronic performance (e.g., carrier mobility, stability in contact with the primary electrolyte) and not on the ease of its chemical modification or robustness to sample fluids, which offers simultaneous opportunities to maximize amplification and to reduce fabrication complexity. Second, well-developed and versatile self-assembled monolayer (SAM) chemistry can be employed to create the selective capture surface on the right arm of the gold floating gate. This in turn opens up opportunities to use a wide array of chemical- or bio-receptors that are conveniently immobilized on gold.[201–203] In an initial study, we demonstrated that FGTs

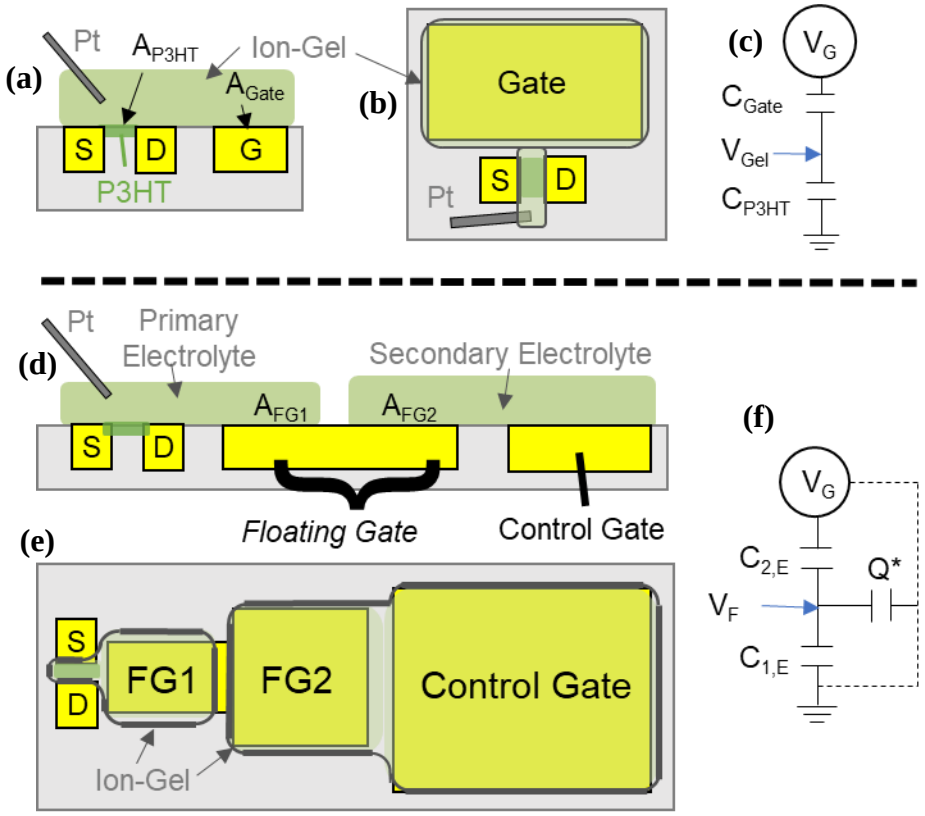

Figure 4.1: Device Architecture.
(a) and **(b)** show a side and top view of an EGT with P3HT in the semiconductor channel (W/L = 40 µm/2 µm) and a platinum wire placed in the ion-gel. **(c)** presents the equivalent circuit used to interpret the response of the device. **(d)** and **(e)** show a side and top view of an FGT with ion-gel as both the primary and secondary electrolyte. **(f)** is the modified equivalent circuit used to interpret an FGT's response.

can be employed to detect DNA oligomers with discrimination of single-base pair mismatches.[200] Interestingly, parallel work has shown the sensor capabilities of floating gate field effect transistors (FG-FETs) that do not use electrolytes, but do employ the same operating principle in which the capture chemistry occurs on the floating gate, not on the semiconductor.[198,199]

As we demonstrate here, FGT operation depends sensitively on the relative areas of the semiconductor/electrolyte, floating gate/electrolyte, and control gate/electrolyte interfaces. Thus, our first goal in the present study was to determine the optimal geometry for FGTs. The second goal was to understand precisely how chemisorption on the right arm of the floating gate affects device response. Specifically, we have investigated the role of interface dipoles and interfacial capacitance using chemisorbed SAMs on the floating gate. FGTs are exquisitely sensitive to both, demonstrating that collective interface dipole and capacitance effects may contribute to the sensor response of an FGT. We also find that the influence of SAMs on the device current-voltage (I-V) behavior can be modeled, to first order, using a simple linear circuit model that can separate dipole effects from capacitance effects. Our experiment and analysis provide the most complete picture to date of the operating mechanisms of FGTs and open the door to more systematic studies on the use of these devices in label-free electronic biodetection experiments.

4.3 Materials and Methods

Materials. Poly(3-hexylthiophene) (P3HT) was purchased from Rieke Metals, Inc. and stored in an inert environment. 1-ethylmethyl imidazolium bis(trifluoromethyl)sulfonylimide (EMIM/TFSI) was purchased from EMD Millipore, Inc.

and stored in an inert environment. Polystryene-*b*-methylmethacrylate-stryene (SMS) was synthesized by a previously reported procedure by Zhang *et al*.[204] The ion-gel was a mixture of SMS and EMIM/TFSI at 1:9 by weight. 6-mercapto-1-hexanol (MCH), octanethiol, dodecanethiol, and octadecanethiol were purchased from Sigma-Aldrich and used as received.

Fabrication. Cr/Au (5 nm/30 nm) electrodes were photolithographically patterned onto a silicon wafer. 50 μm diameter platinum wire (Sigma-Aldrich) was solvent cleaned before being used as a quasi-reference electrode. Organic materials were printed with an Aerosol-Jet 200 Printer (Optomec, Inc.). For printing, P3HT was dissolved in chloroform at 1 mg/ml then terpineol was added as a cosolvent at 0.1 ml per ml of chloroform solution. The solution was printed with a 150 μm nozzle, a carrier gas flow rate of 10 ccm and a sheath gas flow rate of 20 ccm. The ion-gel was mixed with ethyl acetate at a ratio of 1:9 by weight, stirred overnight, then printed with a 150 μm nozzle, but with a carrier gas flow rate of 20 ccm and a sheath gas flow of 25 ccm. More details on the printing process have been reported previously.[205,206]

Microfluidic Channels. Microfluidic flow channels were imprinted into poly(dimethylsiloxane) (PDMS) molds from an SU8 master. The base and curing agent were poured onto the SU8 master at a ratio of 10:1 then heated at 75^{o}C for 2 h. The imprints were 150 μm high in a pattern that outlined the source/drain electrodes, the floating-gate electrode, and primary gate electrode. The imprints over the floating-gate electrode were extended to two inlets/outlets such that a solution injected through one inlet interacted with the semiconductor side of the floating gate (or primary gate side) selectively. These inlets

were 100 μm wide and ~1 mm long. The design is sketched in the supporting information (Figure S4.1).

Interface Functionalization. To fabricate devices functionalized with SAMs, P3HT was printed onto a wafer with patterned electrodes to a thickness of 50 nm and then heated to 120°C for 1 h in a nitrogen environment to anneal the polymer film. The microfluidic channels were aligned by hand and reversibly bonded to the substrate.[207] The SAM molecules were diluted to 1 mM in distilled water for MCH and a 1:1 by volume mixture of ethanol and water for alkanethiols.[208,209,210] The solution was then selectively

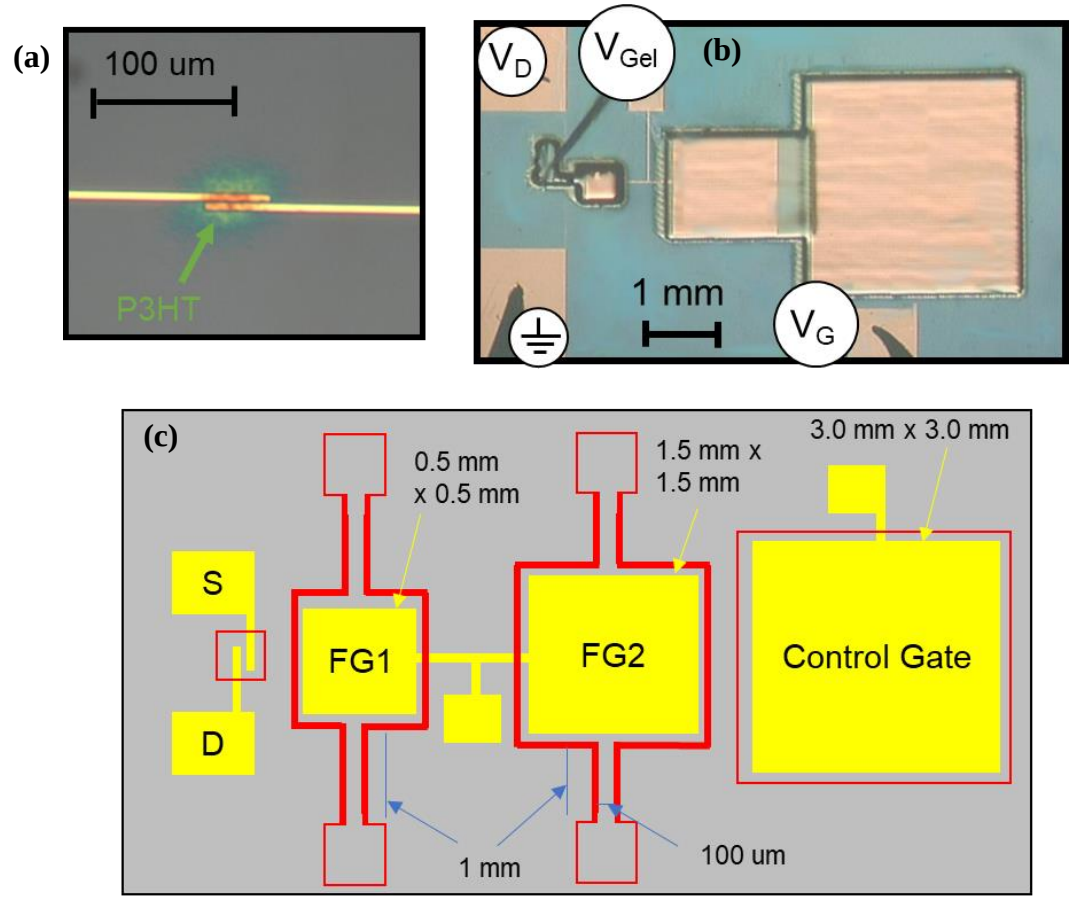

Figure S4.1: Device Structure.
(a) is an image of the printed P3HT film (50 nm) with W/L = 40 μm/2 μm. **(b)** is an image of an FGT with A_{FG1} = 150$A_{P3HT,}$ A_{FG2} = 1500A_{P3HT} and A_{CG} = 6000A_{P3HT}. **(c)** is a schematic of the FGT with the microfluidic channels (outlined in red) used to selectively functionalize the floating gate with SAMs.

flowed over one side of the floating gate at 1 μl/min and allowed to adsorb at room temperature for 2 h followed by rinsing with solvent. Finally, the microfluidic channels were removed so that ion-gel could be printed over the electrodes.

Equipment. All electrical measurements were performed in an inert glove box with a Keithley 2612B Source Measure Unit applying voltages and recording the current at the source/drain electrodes, a Keithley 237 Source Measure Unit applying voltages and recording the current at the gate electrode, and a Keithley 6517A electrometer recording the voltage at the Pt electrode.

4.4 Results and Discussion

Side-Gated EGT. We began our investigation by focusing first on a simple side-gated EGT, Figures 4.1a-c. To understand the device operation, it is important to determine how voltage is "dropped" from the gate electrode to the P3HT channel.[211,212] Thus, in addition to tracking the drain current as a function of V_G, we have inserted a Pt wire into the gel to probe the gel potential (V_{Gel}) with respect to the source electrode as a function of V_G. The goal is to use this extra information to correlate the non-linear behavior of the drain current to the response of a simple, linear equivalent circuit, Figure 4.1c. When the area of the ion-gel/gate electrode interface (A_{Gate}, see Figure 4.1a-b) is lowered compared to the area of the P3HT/ion-gel interface (A_{P3HT}), we observe in Figure 4.2a and 4.2b that (1) the turn-on is not as sharp (or the subthreshold swing, $dV_G/d\log(I_D)$, is higher), (2) the ON current is lower, and (3) there is pronounced hysteresis. When the same data are plotted with respect to V_{Gel} in Figure 4.2c, however, the curves coincide. This is expected because the conductivity of the P3HT film should directly reflect the potential difference across the

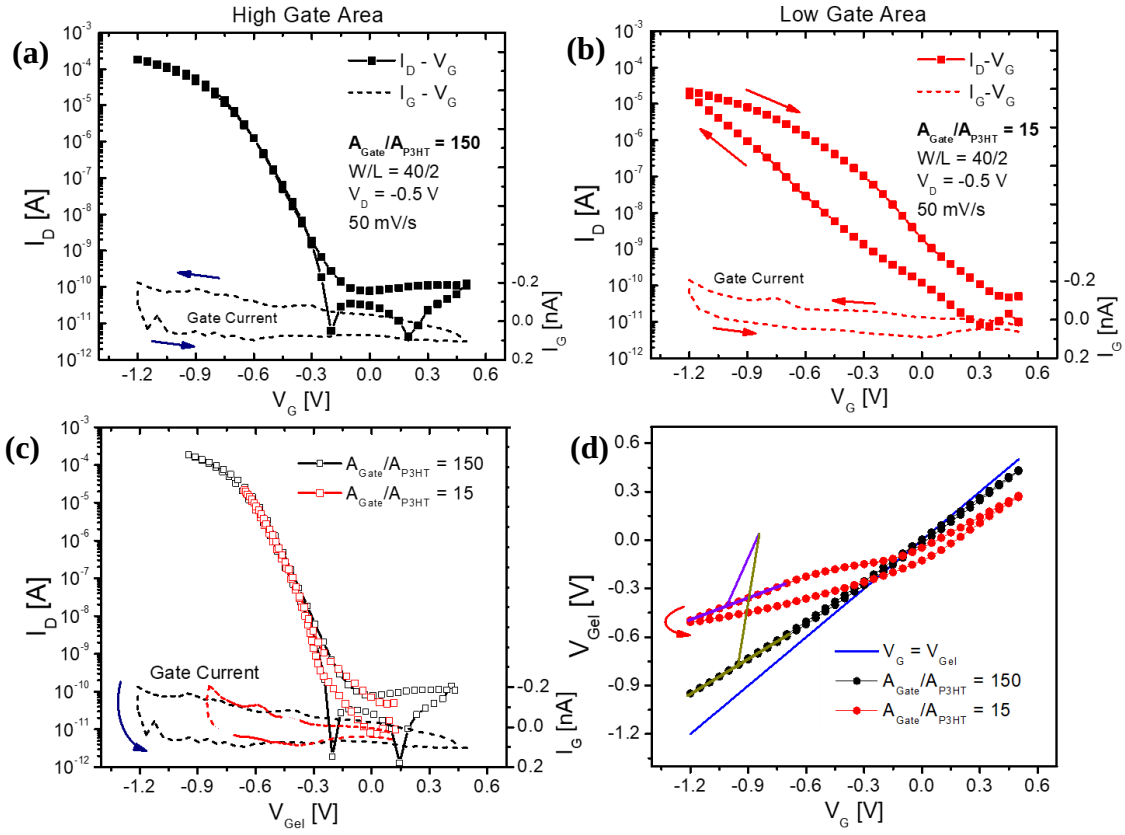

Figure 4.2: Gate Area Dependence of EGT Operation.
(a) the I_D-V_G and I_G-V_G response of an EGT with high gate area (A_{Gate} = 0.5 mm x 0.5 mm). **(b)** the I_D-V_G and I_G-V_G response of an EGT with low gate area (A_{Gate} = 0.10 mm x 0.25 mm). **(c)** I_D-V_{Gel} and I_G-V_{Gel} curves are independent of A_{Gate}. The thickness of the P3HT film was kept constant at 50 nm. **(d)** the V_{Gel}-V_G relationship with the fit from Equation 4.3 highlighted.

P3HT/gel interface (relative to ground at the source electrode). Thus Figure 4.2c confirms that the key potential regulating P3HT conductance, and thus I_D, is V_{Gel}. Equation 4.1, which is the standard equation for a transistor operating in the saturation regime, reads[187]

$$I_D = \frac{W}{2L}\mu C_i (V_{Gel} - V_T)^2 \qquad (4.1)$$

where W/L is the aspect ratio of the P3HT channel (40 µm/2 µm), μ is the carrier mobility (~1 cm^2/V-s),[205] V_T is the threshold voltage of the P3HT (~ -0.3V),[205] and C_i is the specific capacitance of the P3HT/ion-gel interface (~100 µF/cm^2).[190,205]

Next we consider how V_{Gel} should depend on V_G. To a first approximation, we use the simple lumped capacitor model in Figure 4.1c which assumes (1) the semiconductor is held at ground, and (2) zero gate current. We have two capacitors in series: one for the P3HT/ion-gel interface and another for the ion-gel/gate electrode interface. A charge balance at the node labeled "V_{Gel}" in Figure 4.1c yields Equation 4.2,

$$V_{Gel} = \frac{1}{1 + \frac{C_{P3HT}}{C_{Gate}}} V_G \qquad (4.2)$$

where V_{Gel} is the voltage at the node between C_{P3HT} and C_{Gate} which is experimentally measured with a Pt wire dipped into the ion-gel. If $C_{Gate} >> C_{P3HT}$ then $V_{Gel} \approx V_G$ which is desirable to achieve the sharpest turn-on (steepest I_D-V_G curve) because very little voltage is dropped at the gate electrode.

Figure 4.2d displays V_{Gel} measured as a function of V_G for EGTs with A_{Gate}/A_{P3HT} = 150 and 15. Note that V_{Gel} is offset from the voltage measured at the Pt wire by an open-circuit voltage ($V_{Gel} = V_{Pt} – V_{OC}$) which ranges from -0.1 V to -0.2 V from device to device because the Pt wire is a quasi-reference electrode.[213] The V_{Gel} vs. V_G data for the A_{Gate}/A_{P3HT} = 150 case follows a roughly linear relationship as predicted by Equation 4.2. The A_{Gate}/A_{P3HT} = 15 data deviate more substantially. A fit to Equation 4.2 of the data in Figure 4.2d over the whole range of V_G is not possible because C_{P3HT} is voltage dependent.[189,214,215] That is, ions penetrate the P3HT film as V_G (or more accurately, V_{Gel}) becomes more negative and the P3HT becomes electrochemically doped, thus C_{P3HT} changes with V_G.[216,217] C_{Gate} may also have a voltage dependence due to ion adsorption and

packing effects, though this is expected to be weaker than that for C_{P3HT}.[218,219] So Equation 4.2 is simplistic.

A reasonable fit for Equation 4.2 (Figure 4.2d) was nevertheless obtained between V_G = -0.7 V and -1.2 V for the forward sweep over ~2 orders of A_{Gate} by taking $C_{i,P3HT}/C_{i,Gate} = 8$ and offsetting the denominator by 0.17. The capacitance ratio is consistent with previous reports (e.g. 100 μF/cm^2/12.5 μF/cm^2)[205] and the additional offset represents an effective ohmic resistance between the gate electrode and the electrolyte bulk ($0.17 \approx R_{eff}I_G/(V_G-V_{Gel})$) which was not accounted for in the capacitor model for simplicity. The resistance is a combination of a polarization resistance at the ion-gel/gold interface (in parallel with C_{Gate}) and the bulk resistance of the ion-gel (in series with C_{Gate}).[217] More details on this calculation can be found in the Supporting Information.

Another way to analyze these data is to consider the fraction of voltage dropped at the gate electrode/ion-gel interface (F^{Gate}) which can be derived from Equation 4.2,

$$F^{Gate} = \frac{V_G - V_{Gel}}{V_G} = \frac{1}{1 + \frac{C_{i,Gate}A_{Gate}}{C_{i,P3HT}A_{P3HT}}} \qquad (4.3)$$

F^{Gate} is calculated from the fit of Equation 4.2 and plotted with respect to A_{Gate} in Figure 4.3. The end result demonstrates the importance of proper sizing when constructing an EGT by highlighting how the effective voltage is lowered when the gate capacitance is decreased. Improper sizing (small A_{Gate}/A_{P3HT}) requires higher operating voltages. The dependence on gate area saturates at high values, corresponding to $A_{Gate}/A_{P3HT} \geq 50$. This presents a complication when constructing top-gated EGTs with small metal electrodes and ion-permeable semiconductors, because permeability increases the effective capacitance

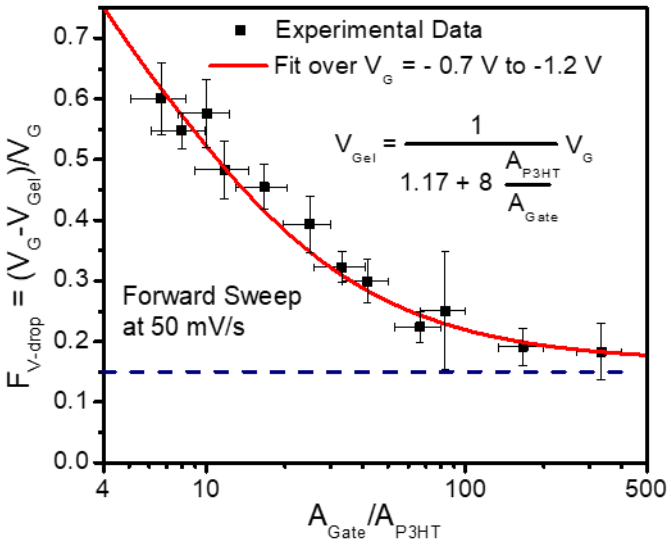

Figure 4.3: Quantitative Area Dependence.
The fraction of V_G dropped at the gate electrode calculated from Equation 4.4 using the fit obtained from Equation 4.3 and plotted as a function of A_{Gate}. Error bars represent the standard deviation of at least 5 devices.

of an interface.[190,220] Previous reports presented high performance, top-gated EGTs with $A_{Gate}/A_{P3HT} \approx 1$ by using PEDOT:PSS as a gate electrode (a permeable gate electrode)[205,221] or by using printed ZnO as the semiconductor (an impermeable channel).[215] The good performance of these devices is rationalized by our current results in Figure 4.3 which show that higher effective A_{Gate}/A_{P3HT} ratios lead to less voltage drop at the gate and correspondingly larger gating effect on the semiconductor.

Hysteresis. The fit in Figure 4.3 only considers the forward sweep of the transfer curve, which is equivalent to the reverse sweep only for high gate area (Figure 4.2a). Hysteresis in an EGT can arise due to trap formation at the semiconductor/electrolyte interface,[222] or impurities. [211,223,224] However, the lack of hysteresis in the I_D-V_{Gel} curves (Figure 4.2c) suggests that the P3HT/ion-gel interface is clean and free of traps. A more advanced equivalent circuit for an EGT could be designed with RC elements at the

P3HT/ion-gel and gold/ion-gel interface to represent the double-layer capacitor and interfacial charge-transfer or polarization resistance.[225] A plausible explanation for hysteresis is then the relative increase of the RC time constant of the P3HT/ion-gel interface with respect to the lowered RC time constant of ion-gel when A_{Gate} is lowered. This may cause V_{Gel} to 'lag' V_G when the device is scanned at a rate comparable to the RC time constant leading to a hysteresis when V_{Gel} is plotted versus V_G (Figure 4.2d). Empirically, we observe that the hysteresis scales with the logarithm of A_{P3HT}/A_{Gate} (Figure S4.2, Supporting Information).

Alternatively, previous reports on room temperature ionic liquids (RTILs) have demonstrated a hysteresis in differential capacitance (ΔC_{Au}) above a critical charge density at the RTIL/gold interface.[218,219] Similarly, the charge transfer resistance at the RTIL/gold interface may exhibit nonlinear behavior (ΔR_{ct}) related to the overpotentials associated with slow kinetics and/or ion adsorption.[218,219] The actual hysteresis is likely a combination of all the mentioned effects, but the geometric dependence sets the lower bound for gate area in order to achieve reliable, direction independent EGT performance.

Floating – Gate EGT. The construction of an EGT with a floating gate follows directly from the results for the side-gated EGT in Figures 4.2 and 4.3. As shown in Figure 4.1d-e, the floating-gate electrode is an extension of the gate electrode in Figure 4.1a and is coupled to the P3HT channel through an ion-gel termed the primary electrolyte. Rather than being directly controlled, the floating gate potential is set by capacitive coupling to a control gate electrode through the secondary electrolyte.[198,226] For biosensing, the secondary electrolyte is aqueous from which target molecules are bound to the right arm

of the floating gate.[200] For the experiments here, the secondary electrolyte is an ion-gel so that every electrode/electrolyte interface is identical. The floating gate electrode straddles both the primary and secondary electrolyte with ion-gel/electrode interfacial areas denoted as A_{FG1} and A_{FG2}, respectively. The goal in the following experiments is to determine the effect that changing the capacitance and work function of the floating gate/secondary electrolyte interface has on the EGT output (which, in principle, could be caused by adsorbing analytes).

Capacitance Sensitivity. Altering the capacitance of the floating gate/secondary electrolyte interface is expected to give similar results to those in Figure 4.3 – namely, smaller capacitances (areas) lead to larger interfacial potential drops. So, as a first approximation, the introduction of a floating-gate was analyzed with the circuit in Figure 4.1f in a manner analogous to the previous approach. C_{1E} is the capacitance of the primary electrolyte, a series combination of the double layer capacitances previously denoted C_{P3HT} and C_{Gate} in Figure 4.1c. C_{1E} was kept constant by maintaining $A_{FG1}/A_{P3HT} = 150$ so that potential drops across the entire primary electrolyte were concentrated at the P3HT/ion-gel interface (see Figure 4.3). C_{2E} is the capacitance between the floating gate and control gate and was varied by printing different ion-gel/floating gate areas (A_{FG2}). The area of the control gate interface was kept constant at 3 mm x 3 mm, much larger than A_{FG2} so it did not contribute to the value of C_{2E}. Q* represents charge stored in the floating gate in a parasitic capacitor that will be discussed later. The voltage between these capacitors now represents the potential of the floating-gate electrode (V_F), as shown in Figure 4.1f.

To understand FGT operation, we performed experiments in which V_G was applied *to the floating gate* (so, it is not floating) in a conventional EGT test ($V_G = V_G^{EGT}$, as done in Figures 4.2-4.3), and then was transitioned to the control gate to test the device with a true floating gate ($V_G = V_G^{CG}$). This procedure allowed the effect of testing an EGT with and without a floating gate to be measured directly. We refer to the data sets as "No

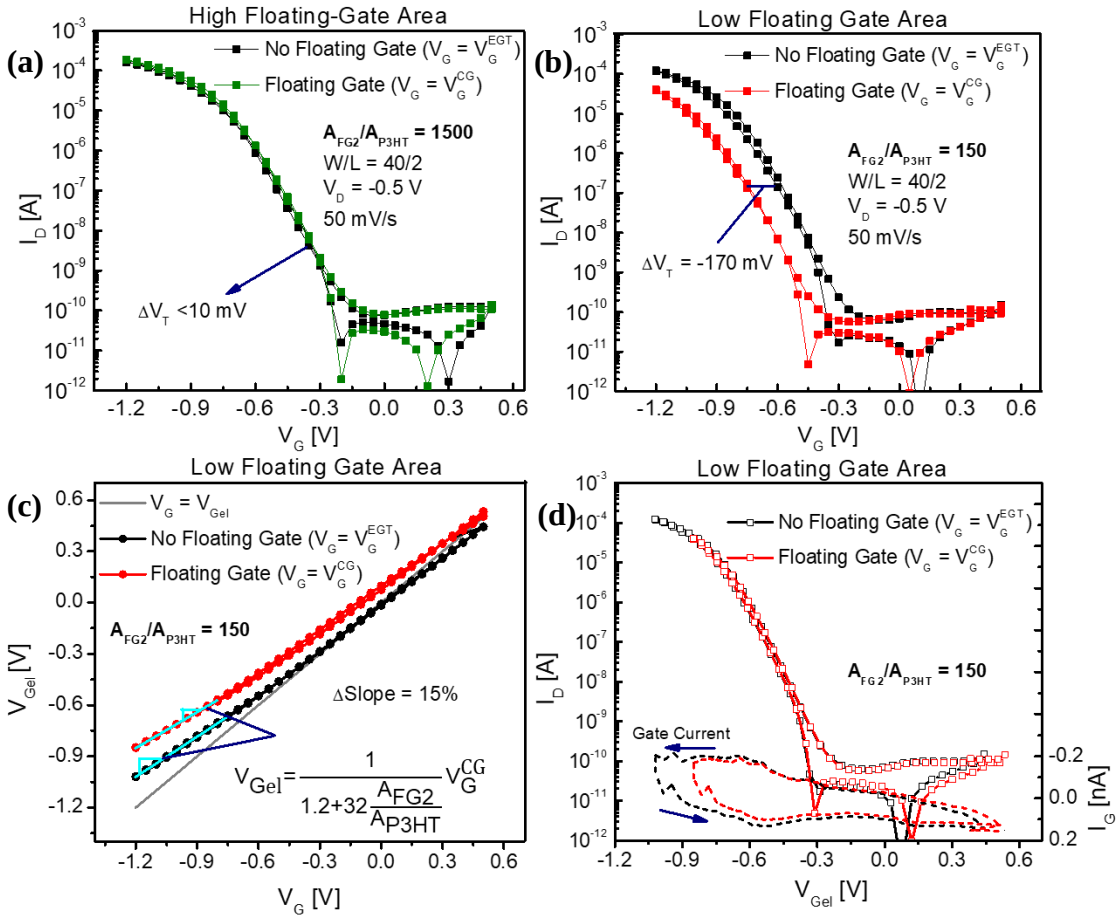

Figure 4.4: Floating-Gate Area Dependence on Device Operation.
(a) the response of an EGT in a conventional test (black) and again with a floating gate (green). In this case, the curves overlap because A_{FG2} is high (1.50 mm x 1.50 mm). **(b)** the difference between conventional (black) and floating gate tests (red) for a device with low A_{FG2} (0.50 mm x 0.50 mm). **(c)** the V_{Gel}-V_G curves for a device with low A_{FG2}. The fit is from Equation 4.3 but with a much higher area dependence than the EGTs in Figure 4.3. **(d)** the I_D-V_{Gel} curves that are again independent of A_{FG2}.

Floating Gate" and "Floating Gate" in Figure 4.4. Figure 4.4a shows the results when A_{FG2}/A_{P3HT} = 1500 (A_{FG2}/A_{FG1} = 10), an intentionally oversized ratio to rigorously avoid parasitic effects, and the resulting transfer curves for the Floating Gate and No Floating Gate scans overlap. Figure 4.4b displays the results for the same test but with A_{FG2}/A_{P3HT} = 150 (A_{FG2}/A_{FG1} = 1); the Floating Gate curve is shifted negatively on the V_G axis due to the lower effective gating of the P3HT channel across the floating gate, i.e. more negative V_G's are required to achieve the same current (in other words, $V_G^{CG} < V_G^{EGT}$ at the same I_D). Similarly, the Floating Gate V_{Gel} vs. V_G curve in Figure 4.4c is shifted negatively to reflect this change. In Figure 4.4d the same current-voltage data are plotted with respect to V_{Gel} causing the curves to coincide as implied by Equation 4.1 and the data in Figure 4.2c. Qualitatively, lowering A_{FG2} is similar to the effect of lowering A_{Gate} in Figure 4.2a and 4.2b except (1) higher areas are required to minimize changes, and (2) no hysteresis results.

To further understand this result, we performed a charge balance on the circuit in Figure 4.1f, assuming Q* = 0 or no stray capacitance in the floating gate, to compare the tests with and without a floating gate (similar to the derivation of Equation 4.2) and arrived at Equation 4.4[198,226,227]

$$V_G^{CG} = \left(\frac{C_{1E}}{C_{2E}} + 1\right) V_G^{EGT} \tag{4.4}$$

where V_G^{CG} and V_G^{EGT} are the voltages applied to the control gate and floating gate that yield the same I_D. A detailed derivation is provided in the Supporting Information, but the role of C_{1E} and C_{2E} on the difference in V_G at the same I_D is expected. A high value of C_{1E}/C_{2E} lowers the effective gating of P3HT since potential is lost across the series capacitors in the secondary electrolyte. However, quantitative analysis with Equation 4.4 underestimates

the dependence of V_G^{CG} and V_G^{EGT} on geometry, that is the $\Delta V_T = V_G^{CG}$-V_G^{EGT} highlighted in Figure 4.4b is larger than would be predicted when the extracted capacitance ratio from Figure 4.3 is used in Equation 4.4. This can also be seen in Figure 4.4c that presents V_{Gel} vs. V_G curves that depend on A_{P3HT}/A_{FG2} ~4x more than predicted from Equation 4.2 and Figure 4.3 (see the factor of 32 in the fit in Figure 4.4c).

A key assumption in Equation 4.4 is that all capacitors are connected in series or Q*= 0. This way, the amount of charge stored on C_{1E} and C_{2E} capacitors is equal.[198] However, when an amount of charge (Q_{2E}) is stored on $C_{2E,}$ not all of this charge is reflected on C_{1E} if a portion is held at the floating-gate/substrate interface (Q*), modeled as a parasitic (or 'stray') capacitor in Figure 4.1f. Further, based off the results in Figure 4.2d, V_{Gel} is linearly proportional to V_G^{EGT} and approximately equal so that V_{Gel} will reflect the potential at the floating gate (V_F). Carrying out a charge balance on the floating gate with the circuit in Figure 4.1f allows for the floating gate potential (V_F) to be expressed by Equation 4.5,

$$V_{Gel} \approx V_F = \frac{C_{2E}}{C_{1E} + C_{2E}} V_G^{CG} - \frac{Q^*}{C_{1E} + C_{2E}} \tag{4.5}$$

This equation has the anticipated dependence on C_{2E} and C_{1E} but carries an additional term that can further offset V_F from V_G^{CG}. Q* can be understood as the difference in charge stored at the floating gate/primary electrolyte and floating gate/secondary electrolyte interfaces ($Q^* = Q_{2E} - Q_{1E}$) and is held on a capacitor between V_F and an unknown potential. As a result, it is difficult to solve for Q* *a priori* and it is instead assumed to be a constant fraction of the charge on C_{2E}. We defined f, the fraction of charge lost ($f = \frac{Q^*}{-Q_{2E}}$ and $0 <$

$f < 1$) on the floating gate, and carried out another charge balance at the floating gate (Figure 4.1f) resulting in Equation 4.6,

$$V_G^{CG} = \left(\frac{C_{1E}}{C_{2E}}\frac{1}{1-f} + 1\right) V_G^{EGT} \tag{4.6}$$

A detailed derivation is provided in the Supporting Information. Comparison of Equations 4.4 and 4.6 shows that if Q* ≠ 0 ($f \neq 0$) then the voltage required to overcome parasitic losses will be increased by a factor of $1/(1-f)$.

Finally, the difference $\Delta V_T = V_G^{CG} - V_G^{EGT}$ is evaluated at the current threshold, on a plot of $I_D^{1/2}$ vs. V_G as shown in Figure 4.5a, and is also presented in Figure 4.5b as a function of A_{FG2}/A_{P3HT}. The resulting fit to Equation 4.6 is shown in blue by taking f = 0.77 and C_{1E}/C_{2E} = 8 from Figure 4.3. The gray line is with f = 0 and C_{1E}/C_{2E} = 8 to illustrate the insufficiency of Equation 4.4 to fully describe the behavior of FGTs. Equation

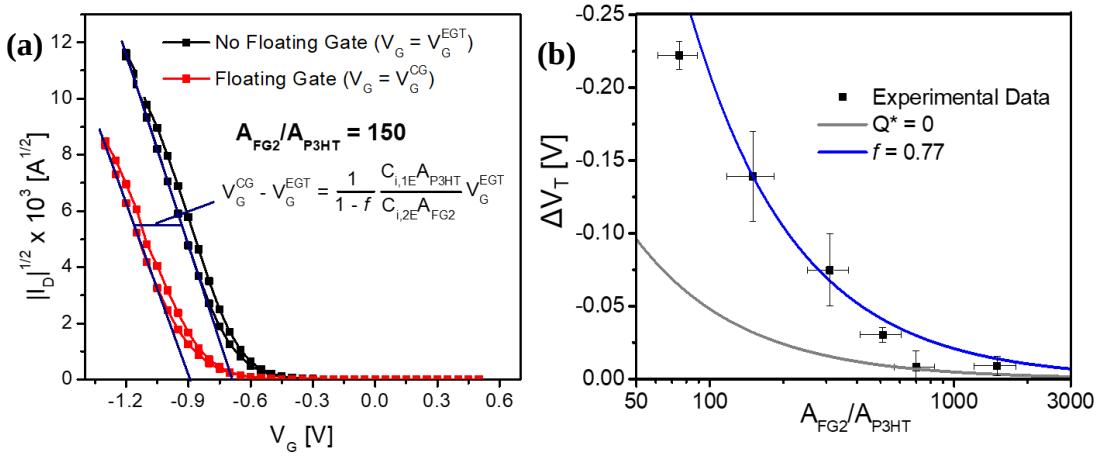

Figure 4.5: Floating Gate Area Dependence on Device Operation.
(a) shows the square root of I_D vs. V_G and linear scaling predicted by Equation 4.1, and a sample calculation of the change in threshold voltage for a floating gate EGT with low A_{FG2}. The change in threshold voltage is recorded and plotted with respect to A_{FG2} in **(b)** with a fit from Equation 4.4 in blue for f = 0.77. The gray line is the insufficient fit with f = 0.

4.6 accurately captures the V_T shift for FGTs relative to EGTs. A significant fraction of potential is lost across the floating gate due to parasitic capacitance. Importantly, we find that this is not detrimental to FGT operation and only affects the sizing criteria of the device.

Effect of Changing the Floating Gate Work Function. In addition to changing the capacitance, adsorption of biomolecules can also change the work function or electrochemical potential of the underlying substrate.[196,228] Common practice in biosensor design is to first chemisorb a self-assembled monolayer (SAM) of alkyl-thiol derivatives.[201,202] The versatile chemistry of SAMs can be easily exploited so that the surface will selectively capture the analyte of interest.[229,230] This process is well-known to change the work function of the underlying metal[230] and the shift is commonly measured in an inert environment using ultraviolet photoelectron spectroscopy (UPS)[210] or scanning kelvin probe microscopy (SKPM).[231] Immobilizing alkyl-thiols onto the electrodes of an EGT has been studied previously and shown to alter the injection barrier of carriers into the semiconductor when bound to the source/drain electrodes,[230,191] and also to tune the threshold voltage of an EGT when the thiols are bound to the dielectric.[232,233] The goal of these final experiments was to observe how forming a SAM (thus changing the work function) on either side of the floating gate electrode impacted the measured I_D-V_G curves.

1-Mercaptohexanol (MCH) ($HS\text{-}(CH_2)_5\text{-}CH_3$) was used to alter the work function of the floating-gate electrode. MCH is commonly used to passivate sensing surfaces and, like many alkyl-thiol derivatives,[229] is expected to lower the work function of gold.[234] The molecules were selectively deposited onto the primary electrolyte/floating gate electrode

interface (FG1, the left arm) or the secondary electrolyte/floating gate electrode interface (FG2, the right arm) by flowing them through reversibly bonded microfluidic channels, rinsing/drying, removing the microfluidic channels, then printing ion-gel over the functionalized electrode. In these experiments, the area of the floating-gate was intentionally oversized (A_{FG2}/A_{P3HT} = 1500) so that reducing the interfacial capacitance by SAM formation would not diminish the capacitive coupling between the control gate and floating gate.

Figure 4.6 presents the results of absorbing MCH on either side of the floating gate; there is a clear dependence on the location of the SAM. Figure 4.6a demonstrates that the SAM on FG1 shifts the threshold voltage negatively, while the SAM on FG2 (Figure 4.6b) shifts it positively. Figure 4.6c and 4.6d display V_{Gel}-V_G curves that give insight into the mechanism changing the I-V curves. Instead of changing slopes (dV_{Gel}/dV_G) due to changing capacitance as in Figure 4.2d and Figure 4.4c, the V_{Gel}-V_G curves are horizontally offset from the reference curve, taken from a device without a SAM, and approximately parallel to it. Once again, if the I_D-V_G curves are plotted with respect to V_{Gel}, they collapse as predicted from earlier results (data not shown).

It is well known that the work function of gate electrodes impacts the threshold voltage of transistors.[212] Figure 4.7 outlines the thermodynamics of changing the floating gate work function. First consider the case of a SAM on the primary electrolyte/floating gate interface (FG1, in Figure 4.6A). The electrochemical potential difference between P3HT and the control gate electrode is then, $E_G^1 = \varphi_{P3HT} - \varphi_{SAM}$ (Figure 4.7b). Experimentally, the functionalized device is tested in parallel with a non-functionalized

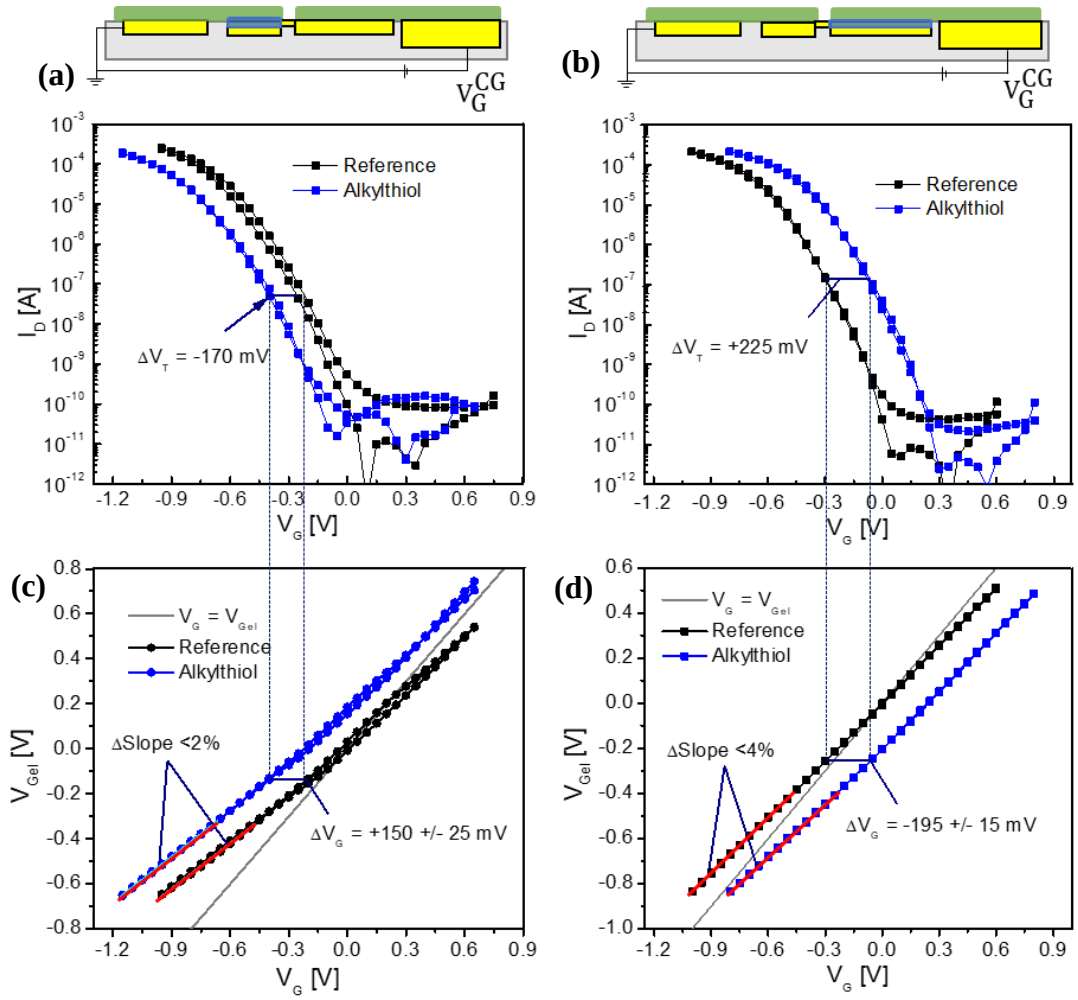

Figure 4.6: SAM Orientation Dependence.
(a) an FGT tested with MCH chemisorbed on the left arm of the floating gate (A_{FG1}) denoted in blue in the device sketched above it. The transfer curve shifted negatively by -170 mV along with **(b)** showing the V_{Gel}-V_G curve. **(c)** an FGT tested with MCH chemisorbed on the right arm of the floating gate (A_{FG2}) denoted in blue in the device sketched above it. The transfer curve is shifted positively by +230 mV. **(d)** the corresponding V_{Gel}-V_G curve.

device with $E_G^0 = \varphi_{P3HT} - \varphi_{Au}$ (Figure 4.7a). In this manner, the difference in electrochemical potential between the samples is $\Delta E_G = E_G^1 - E_G^0 = \varphi_{Au} - \varphi_{SAM}$. Therefore, if the SAM lowers the work function then the electrochemical potential at the gate electrode must be raised (by applying a more negative V_G) in order to compensate this energy difference and generate the same response in the P3HT film (same I_D).[212] With this

convention, $\Delta V_G = -\Delta E_G = \varphi_{SAM} - \varphi_{Au}$, yielding the negative V_T shift observed in Figure 4.6a.

In the next experiment the same molecule was chemisorbed on the secondary electrolyte/floating gate interface (A_{FG2}, Figure 4.6b). Carrying out a similar analysis, the electrochemical potential of the control gate with a SAM is $E_G^2 = (\varphi_{P3HT} - \varphi_{Au}) + (\varphi_{SAM} - \varphi_{Au})$ (Figure 4.7c) and without a SAM is still $E_G^0 = \varphi_{P3HT} - \varphi_{Au}$ (Figure 4.7a). Now, the polarity of the SAM is opposite from when it was in the primary electrolyte and $\Delta V_G = \varphi_{Au} - \varphi_{SAM}$. As a result, the V_T shift in Figure 4.6B has the opposite direction as the V_T shift in Figure 4.6a because lowered work functions result in positive V_T shifts due to the different orientation of the SAM with respect to the P3HT film. This is also reflected in the V_{Gel} vs. V_G curves that are shifted in opposite directions when the SAM location is changed, Figures 4.6c-d. Therefore, the orientation of the SAM with respect to the P3HT film controls the polarity of the voltage offset between V_{Gel} and V_G. This effect can be incorporated into Equation 4.5 by introducing $\Delta\varphi_{SAM}$ to reflect the offset of V_F with respect to V_G

$$V_{Gel} \approx V_F = \frac{1}{1 + \frac{C_{2E}}{C_{1E}} \frac{1}{(1-f)}} V_G^{CG} \pm \Delta\phi_{SAM}/e \qquad (4.7)$$

where $\Delta\varphi_{SAM}$ is negative if the SAM is located on the left arm of the floating gate (FG1) and positive if it is on the right arm (FG2) and e is the elementary charge. Equations 4.1 and 4.7 are the basic working equations of FGTs. Equation 4.7 shows the impact of capacitance and work function changes on the control potential V_{Gel} and Equation 4.1 relates V_{Gel} to the source-drain current, I_D.

Sensitivity to SAM Thickness. Three alkylthiols of increasing length were used to measure the sensitivity of FGT response to SAM thickness: octanethiol, dodecanethiol, and octadecanethiol. (Note that MCH used previously is a 6 carbon chain). SAMs of these molecules were formed on the floating gate/secondary electrolyte interface (right arm) and the device response was measured by testing with and without a floating gate. The size of the right arm floating gate (A_{FG2}) was set to $500A_{P3HT}$ so that, according to Figure 4.5b, the reduced capacitance from SAM formation altered the response of the coupled EGT. This way, the device sensitivity to molecular-scale changes in capacitance was enhanced.[196,235]

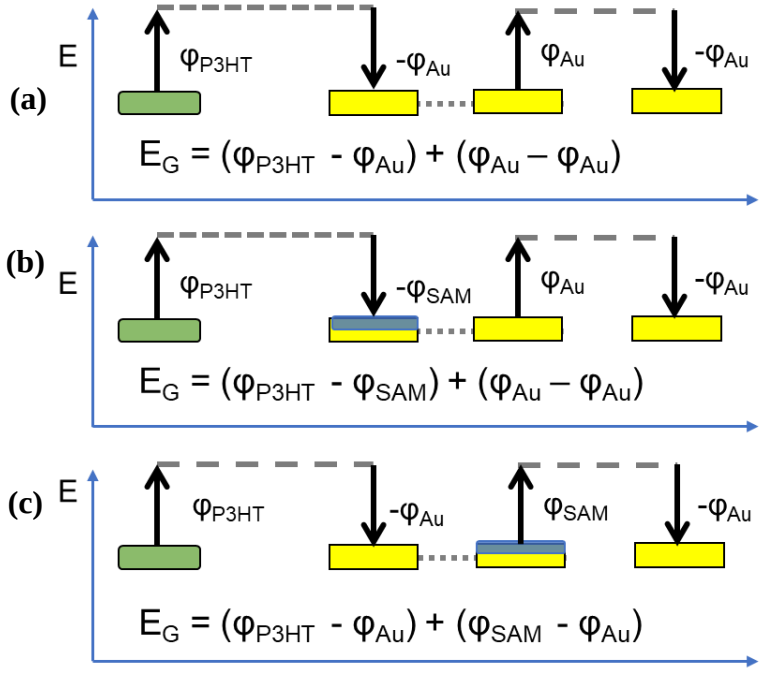

Figure 4.7: Interface Functionalization.
The schemes illustrate the impact of SAM location on the electrochemical potential at the primary gate with respect to the semiconductor (E_G). P3HT (orange) is the reference point and upward arrows indicate a positive change in electron energy due to the interfacial work function (φ), while downward arrows indicate a negative change in energy. The electrochemical potential through the ion-gel bulk is assumed to be constant. **(a)** depicts the situation for a reference FGT without a SAM. **(b)** describes an FGT with a SAM on the primary electrolyte/floating gate interface (FG1, left arm). **(c)** is for an FGT with a SAM on the secondary electrolyte/floating gate interface (FG2, right arm).

In contrast, the area of the floating gate/secondary electrolyte interface (A_{FG2}) in Figures 4.6 and 4.7 was intentionally oversized so that reduction in C_{2E} from SAM formation did not appreciably lower C_{2E} with respect to C_{1E}. That is, the capacitive coupling between V_F and V_G^{CG} was still at the maximum.

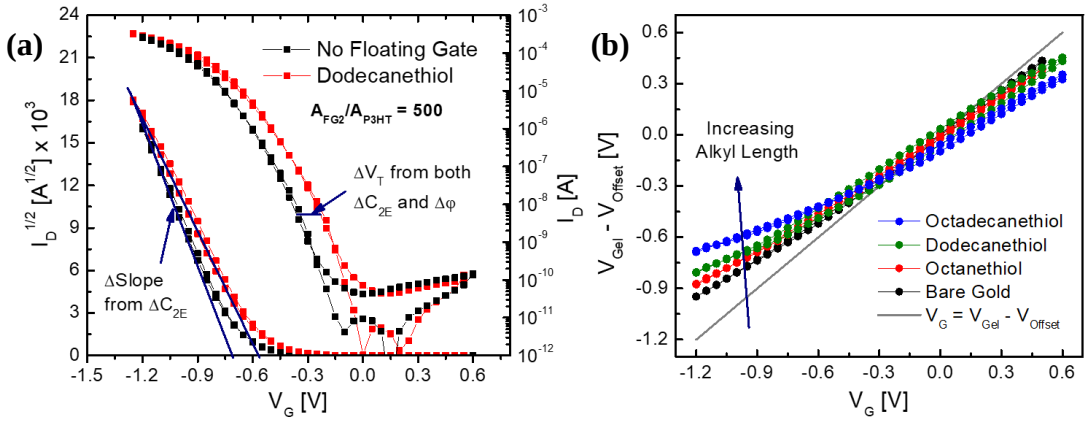

Figure 4.8: SAM Thickness on Floating Gate.
(a) shows the dependence of testing a device without (black) and with (red) a floating gate with a SAM of dodecanethiol absorbed on the floating gate. The ΔV_T is due to a combination of changing capacitance and surface potential while the change in slope is due to a change in capacitance. **(b)** shows V_{Gel}-V_G curves for different lengths of alkylthiol. The slopes consistently decrease as the length is increased. The curves have been normalized by subtracting off the offset due to an altered surface potential.

The formation of a SAM at an electrode/electrolyte interface alters the surface potential of the electrode and also reduces the interfacial capacitance.[210,232] This reduction in capacitance can be understood by modeling the SAM as a thin, parallel-plate capacitor in series with the larger, double-layer capacitor ($1/C = 1/C_{SAM} + 1/C_{DL} \approx 1/C_{SAM}$).[233,236] This result is illustrated in Figure 4.8a where dodecanethiol absorbed on the right arm of the floating gate causes a positive change in V_T and a clear reduction in the slope of I_D-V_G curves. We propose that the former effect is due to a combination of an altered surface potential and reduced capacitance while the latter effect is due to a reduced capacitance

only. Figure 4.8b shows the V_{Gel}-V_G curves as a function of SAM length after normalization. As the alkyl thiol length increases, dV_{Gel}/dV_G decreases in support of this model. Figure 4.9 shows the calculated fraction of V_G dropped ($F_{V\text{-}drop}$) across the floating gate electrode for SAMs of the three alkyl thiols at $A_{FG2}/A_{P3HT} = 500$. The gradual increase in $F_{V\text{-}drop}$ is expected as the length (t_{SAM}) of the SAM increases because $C_{SAM} \approx \kappa_{SAM} A_{FG2}/t_{SAM}$ and $F_{V\text{-}drop} \sim 1/C_{SAM}$. The results show that the presence of a SAM is easily observed for all lengths when compared to a bare gold electrode. Thus, FGTs are extraordinarily sensitive to capacitance at the floating gate/secondary electrolyte interface.

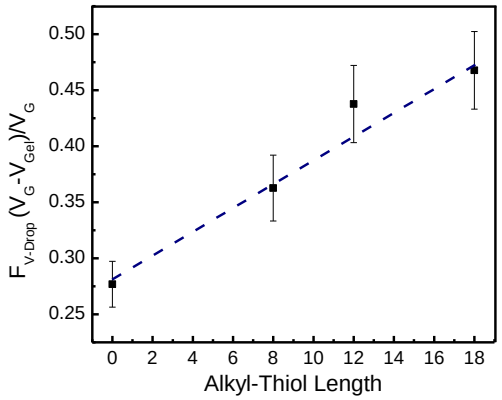

Figure 4.9: Device Response and SAM Length.
The calculated $F_{V\text{-}drop}$ for an FGT with the right arm of the floating gate functionalized with octadecanethiol, dodecanethiol, octanethiol, and no SAM. The ratio of $A_{FG2}/A_{P3HT} = 500$ so that changes in C_{2E} would elicit a response. The error bars are the standard deviation of at least 5 devices.

4.5 Conclusions

In this paper we have elucidated the major factors affecting the current-voltage response of FGTs. Convenient, hysteresis-free control of semiconductor conductivity (i.e., I_D) requires a stepped reduction of electrode/electrolyte interfacial areas, i.e., $A_{CG} > A_{FG2} \geq A_{FG1} > A_{P3HT}$. Equations describing FGT operation in simple terms have been developed

(e.g., Equations 4.1 and 4.7) that show FGTs are sensitive to both capacitance and work function changes on the floating gate. These effects were clearly demonstrated using SAMs to modify the work function and capacitance. The inherent sensitivity of FGTs to both work function and capacitance opens up intriguing opportunities to use these devices in a variety of sensing applications, where, for example, selective chemisorption provides a clearly measurable threshold voltage shift in the I_D-V_G characteristics.

4.6 Supporting Information.

Derivation of Equations 4.2-4.3

Considering the circuit in Figure 4.1C (two capacitors in series), a charge balance yields

$$Q_{Gate} + Q_{P3HT} = 0 \qquad \text{(S4.1)}$$

substituting in the definition of capacitance (Q = CV)

$$C_{Gate}(V_{Gel} - V_G) + C_{P3HT}V_{Gel} = 0 \qquad \text{(S4.2)}$$

and rearranging for Equation 4.2 after substituting $C = C_iA$

$$V_{Gel} = \frac{1}{1 + \frac{C_{i,P3HT}A_{P3HT}}{C_{i,Gate}A_{Gate}}}V_G \qquad (4.2)$$

Rearranging further results in Equation 4.3, the fraction of voltage dropped at the gate electrode

$$F^{Gate} = \frac{V_G - V_{Gel}}{V_G} = \frac{1}{1 + \frac{C_{i,Gate}A_{Gate}}{C_{i,P3HT}A_{P3HT}}} \qquad (4.3)$$

To overcome experimental limitations, mainly the variability of open circuit voltage of the quasi-reference Pt electrode, we considered the slope of V_{Gel}-V_G

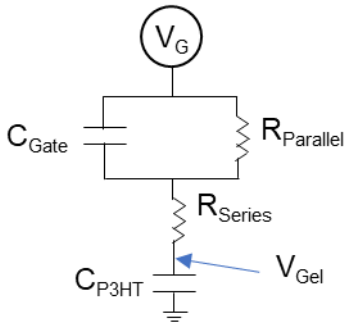

Figure S4.2: Sketch of a More Advanced Equivalent Circuit of an EGT

$$\frac{dV_G}{dV_{Gel}} = 1 + \frac{C_{i,P3HT}A_{P3HT}}{C_{i,Gate}A_{Gate}} \qquad \text{(S4.3)}$$

When plotting this relationship, we found that the slope of dV_G/dV_{Gel} with respect to A_{P3HT}/A_{Gate} is ~8, representing the ratio of specific capacitances. However, the intercept was not unity, and instead 1.17. We attribute this area-independent potential drop to a combination of series resistance through the ion-gel bulk and a parallel resistance at the gate electrode interface due to charge transfer and electrode polarization. This is sketched in Figure S4.2.

Additional data on hysteresis effects in FGTs. In addition to altering the relationship between V_G and V_{Gel}, lowering the gate area also affects the hysteresis in an EGT. We observed a systematic increase in hysteresis, defined as the difference in V_G between the forward and reverse sweep at the same I_D (Figure S4.3A), with lowered gate area (Figure S4.3B). We attributed this to a combination of potential dependent capacitance, overpotentials associated with interfacial charge transfer, and mass transport limitations of ions into the P3HT film as discussed in the main text.

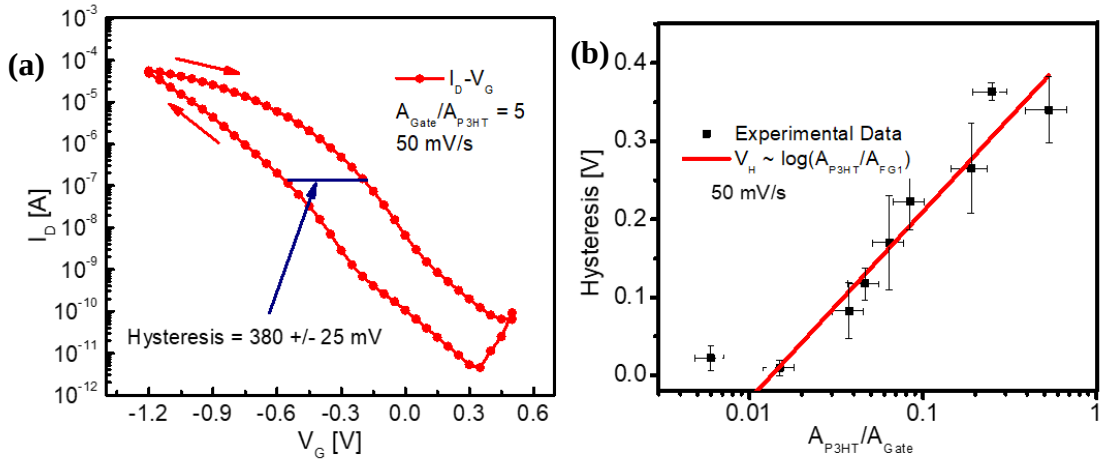

Figure S4.3: Hysteresis in an EGT.
(a) is an EGT with A_{Gate}/A_{P3HT} = 5 and a significant hysteresis of 380 ± 25 mV, calculated by measuring the difference in V_G between the forward and reverse sweep at the same I_D. This calculation is repeated for multiple A_{Gate} values and plotted in **(b)** with a logarithmic fit in red.

Derivation of Equations 4.4-4.6

Considering the circuit in Figure 4.1F (two capacitors in series and an additional parasitic capacitor), we compared the effect of applying V_G to the floating gate (V_G^{EGT}) and control gate (V_G^{CG}) by performing a charge balance and assuming I_D directly reflects the charge on C_{1E} (Q_{1E}).

$$\Delta Q_{1E} = 0 \qquad \text{(S4.4)}$$

Substituting in the definition of capacitance (Q = CV) yields

$$C_{1E}V_G^{EGT} - C_{1E}V_F = 0 \qquad \text{(S4.5)}$$

Next, perform a charge balance on the node labeled "V_F" in Figure 4.1F while assuming Q* = 0 to express V_F in terms of V_G^{CG} analogous to the derivation of Equation 4.2

$$V_F = \frac{1}{1 + \frac{C_{1E}}{C_{2E}}} V_G^{CG} \qquad \text{(S4.6)}$$

Substitute Equation S4.6 into Equation S4.5 for Equation 4.4 in the text,

$$V_G^{CG} = \left(\frac{C_{1E}}{C_{2E}} + 1\right) V_G^{EGT} \qquad \text{(4.4)}$$

Next, introducing a stray capacitor with Q* stored on it requires modification of the charge balance on the node labeled "V_F"

$$Q_{1E} + Q_{2E} + Q^* = 0 \qquad \text{(S4.7)}$$

Substituting in the definition of capacitance furnishes

$$C_{1E}V_F + C_{2E}(V_F - V_G^{CG}) + Q^* = 0 \qquad \text{(S4.8)}$$

Rearranging results in Equation 4.5 in the text,

$$V_F = \frac{C_{2E}}{C_{1E} + C_{2E}} V_G^{CG} - \frac{Q^*}{C_{1E} + C_{2E}} \qquad \text{(4.5)}$$

To account for Q* empirically, we assumed that it is a constant fraction of the charge stored in C_{2E}, but opposite in sign, so that $f = Q^*/-Q_{2E}$ and substituted this into Equation 4.5

$$V_F = \frac{C_{2E}}{C_{1E} + C_{2E}} V_G^{CG} + \frac{fC_{2E}(V_F - V_G^{CG})}{C_{1E} + C_{2E}} \qquad \text{(S4.9)}$$

Rearranging for V_F in terms of V_G^{CG} yields

$$V_F = (1 - f)\frac{1}{1 + \frac{C_{1E}}{C_{2E}}} V_G^{CG} + f\frac{1}{1 + \frac{C_{1E}}{C_{2E}}} V_F \qquad \text{(S4.10)}$$

$$\left((1 - f) + \frac{C_{1E}}{C_{2E}}\right) V_F = (1 - f)V_G^{CG} \qquad \text{(S4.11)}$$

$$V_F = \frac{1}{1 + \frac{1}{1-f}\frac{C_{1E}}{C_{2E}}} V_G^{CG} \qquad \text{(S4.12)}$$

Substituting Equation S4.12 back into Equation S4.5 above results in Equation 4.6 in the text,

$$V_G^{CG} = \left(\frac{C_{1E}}{C_{2E}}\frac{1}{1-f} + 1\right) V_G^{EGT} \qquad \text{(4.6)}$$

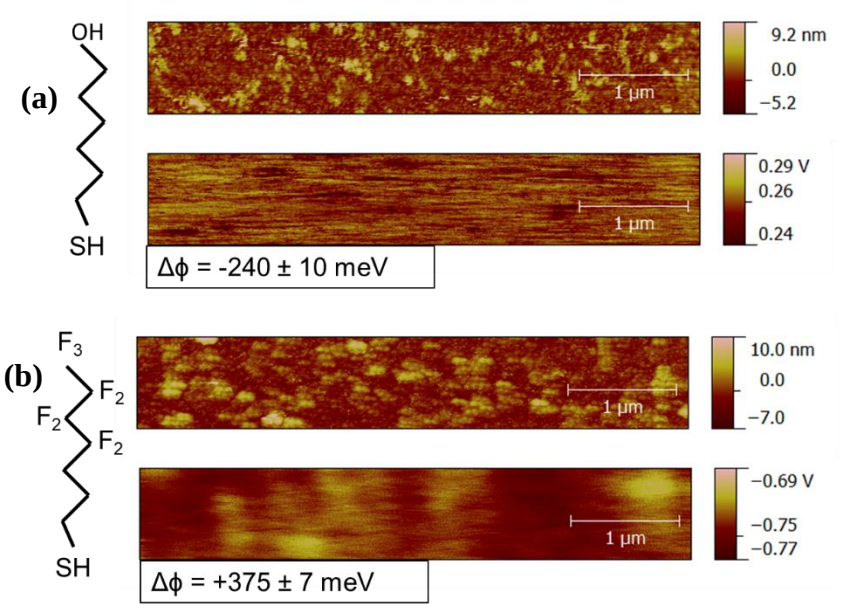

Figure S4.4: Scanning Kelvin Probe Micrographs of Thiol SAMs.
(a) is a scanning kelvin probe micrograph of a gold strip functionalized with MCH and **(b)** is scanning kelvin probe micrograph of a gold strip functionalized with NFH.

Funding sources. Scott P. White thanks the NSF for a Graduate Research Fellowship. Partial support was provided by NSF through grant ECCS-1407473 and a Packard Fellowship from the David and Lucile Packard Foundation.

5. Rapid, Selective, Label-Free Aptameric Capture and Detection of Ricin in Potable Liquids Using a Printed Floating Gate Transistor

5.1 Abstract.

We report a label-free method to quantify protein levels using a combination of printed electronic and microfluidic technologies. The protein, in this case ricin, is captured by a floating electrode functionalized with a DNA aptamer. The binding is transduced into an amplified potentiometric signal by a printed, electrolyte-gated transistor (EGT). Microfluidic channels physically separate the active sensor surface from the EGT-transducer, permitting the capture of ricin down to 30 pM (1 ng/mL) in buffer and 300 pM (10 ng/mL) in orange juice and milk in the absence of pre-concentration. The assay is flow-based, leading to measurement in minutes since no pre-processing, enzymatic reaction, or rinsing steps are needed. Its easy fabrication, multiplexability, simple operation and facile analysis, combined with rapid quantitation at clinically relevant levels, make this strategy a promising approach to parallelized monitoring of toxin levels in food and other environmental samples.

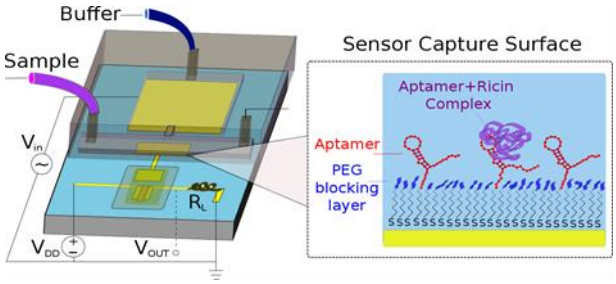

Figure 5.0: Overview Sketch.

5.2 Introduction

Rapid detection of toxic proteins remains a crucial challenge for homeland security,[237] food safety,[238] and disease diagnosis.[239,240] Sandwich immunoassays such as an Enzyme-Linked Immunosorbent Assay (ELISA) are the gold standard for detection, but

rely on time- and labor-intensive antibody labeling of immobilized analytes.[241] Alternatively, lateral flow assays (LFAs) mitigate the laboratory infrastructure and labor issues, but suffer from complex quantitation methods[242,243] and poorer detection limits.[244] Significant efforts are underway to develop new chemical analysis technologies, including electrochemical,[245] Raman,[246] surface plasmon resonance,[247] and piezoelectric[248] sensors, that can achieve clinically relevant detection limits much faster than conventional methods. However, these techniques require complex laboratory equipment and analysis or pre-processing steps for samples extracted from complex media (e.g. food). Additionally, the use of analyte-specific transduction methods can limit the scope of their applicability; in most cases, a detector adaptable for chemically diverse analytes is preferred.[238,249,1]

We report a label-free, transistor-based method to measure the concentration of ricin, an easily obtained toxic protein,[237] in complex media using a combination of printed electronic and microfluidic technologies.[250] The specificity for ricin is achieved with a nucleic acid aptamer[251] which, compared to an antibody, is more stable, easier to synthesize, and more chemically versatile.[15,16] The focus here is placed on aptameric detection of ricin, but this sensor platform should be applicable to detection of other proteins for which suitable capture aptamers or antibodies are known. The sensor is based on a floating gate transistor (FGT) architecture. As shown in Figure 5.1A, the poly(3-hexylthiophene) (P3HT) semiconductor channel on the left side of the device is coupled to the left arm of a floating gate electrode (FG-L) by means of a non-aqueous gel electrolyte. The right arm of the floating gate (FG-R) is in turn coupled via aqueous electrolyte to the electrically addressable control gate (C_G) on the right side of the device. The FG-R is also functionalized with aptamers (Figure 5.1B) and it is the sensor capture surface. Two

microfluidic channels fit over the FG-R and the C_G (Figure 5.1C); one channel feeds the sample medium to the FG-R and the other feeds clean aqueous electrolyte to the C_G. The streams merge such that there is flow over both electrodes and a continuous ionically conducting path between them. The C_G flow stream keeps the sample fluid from fouling the C_G surface. Convective flow over the FG-R decreases mass transport limitations and improves the response time of the device.[182,254,154]

In the absence of ricin, sweeping the potential at the C_G produces a marked change in conductivity of the P3HT channel; the change in conductivity occurs abruptly at a certain trip voltage, V_T (see Figure S5.1).[250,255] When ricin binds to the aptamer-functionalized FG-R, the trip voltage V_T changes. This shift in V_T is the basis of the sensor.

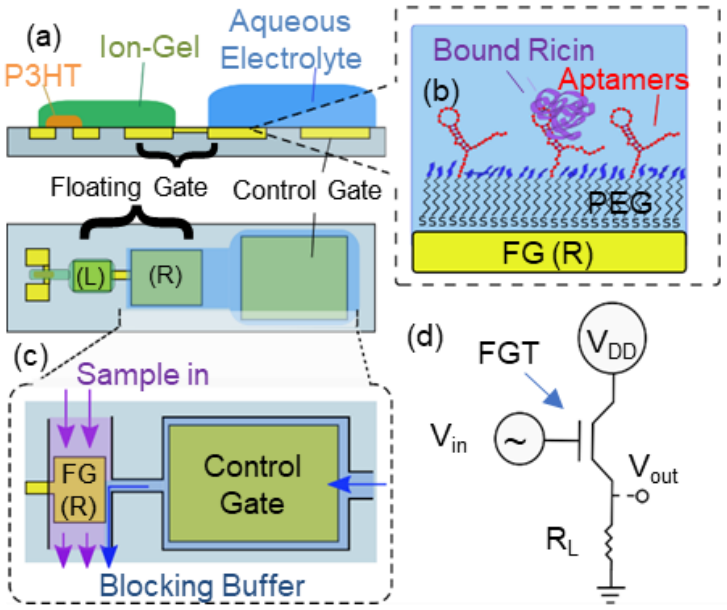

Figure 5.1: Sensor Schematic.
(a) Side- and top-view of the FGT biosensor consisting of P3HT and an ion-gel along with the floating-gate (FG) electrode coupled to the control gate through an aqueous electrolyte. **(b)** Active surface of the sensor with the FG/aqueous interface functionalized with a PEG-SH blocking layer and aptamers that specifically capture ricin. **(c)** Microfluidic schematic with the analyte containing sample flowed over the FG in purple and buffer over the control gate in blue. **(d)** Equivalent circuit of the biosensor with the FGT in series with a resistor (R_L).

In order to conveniently detect the V_T shift and to amplify it, we have connected the floating gate transistor to a series resistor (Figure 5.1D). This simple circuit is an inverter. The red trace in Figure 5.2A shows the quasi-static response of the inverter in the absence of ricin; the voltage V_{in} applied to the C_G was swept slowly and the output voltage V_{out} between the transistor and the resistor was recorded. As is the case for an inverter, V_{out} is high when V_{in} is low and V_{out} is low when V_{in} is high. The trip voltage V_T of the inverter is labeled. The blue curve in Figure 5.2A is the response after exposure of the

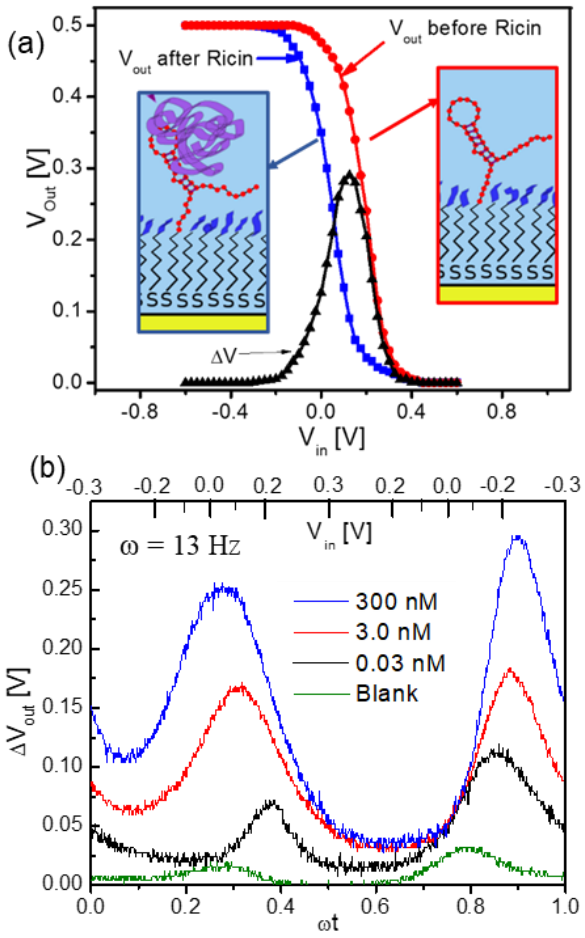

Figure 5.2: Protein Detection with FGTs.
(a) Quasi-static measurement of V_{out} as V_{in} is swept before (red) and after (blue) ricin exposure. The black curve is the difference in these to measurements at the same V_{in}. **(b)** Raw output of devices exposed to increasing ricin concentration.

aptamer-functionalized FG-R to a very high concentration of ricin subunit B (>1 μg/mL, >300 nM). The blue trace is shifted negatively with respect to the red curve, and the black curve is the difference between the traces, ΔV_{out}. This differential response peaks at Vin ≈ +0.15 V where the inverter gain (dV_{out}/dV_{in}) is maximum. ΔV_{out} is the signal response of the device and is proportional to ricin concentration, as we will show. In Figure 5.2A, the gain is ~2 but increases to 5 for lower concentrations of ricin. The possibility of much higher gains (and correspondingly larger ΔV_{out}) for suitably optimized floating gate inverters is an attractive feature of this transistor sensor design.

In practice, we obtain ΔV_{out} by subtracting the output of a reference inverter not exposed to ricin from the output of an inverter exposed to ricin. The test and reference inverters are fabricated side-by-side and form two arms of a differential amplifier (Figure S5.1). A 13 Hz, sinusoidally-varying input signal V_{in} is fed simultaneously to the C_G of

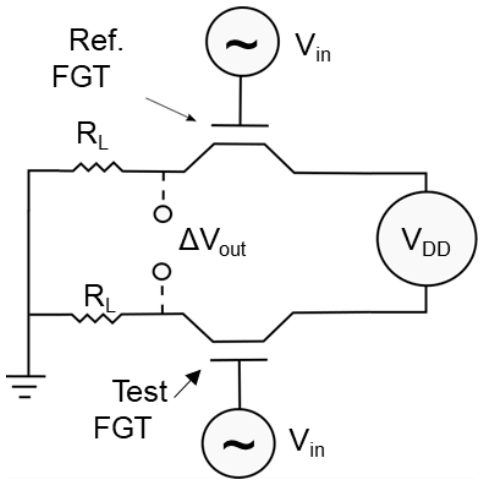

Figure S5.1: Equivalent Circuit of Differential Amplifier Scheme.
FGTs are placed in series with a load resistance (R_L) with a driving voltage (V_{DD}) set across them. The Reference FGT is functionalized with only PEG while the Test FGT has PEG and aptamers for ricin. The AC input voltage (V_{in}) modulates the conductivity of the FGTs and is read as a ΔV_{out} between them.

both the test and reference inverters and ΔV_{out} is recorded. The signal is monitored as the sample stream flows over the floating gate[182] and recorded until the signal is stable for ~10 min.

The ΔV_{out} waveforms for ricin concentrations of 30 pM, 3 nM, and 300 nM are shown in Figure 5.2B for an AC-input of ±0.3V at 13 Hz when ricin is dissolved in buffer (PBS 1x). As seen in Figure 5.2A, the ±0.3V sweep covers much of the non-zero range of ΔV_{out}. The peaks in ΔV_{out} in Figure 5.2B occur at $V_{in} \approx +0.15$ V and -0.2 V and there is no mirror symmetry about the time $\omega t = 0.5$, owing to hysteresis with respect to V_{in} as the transistor is switching between "ON" and "OFF" states at shifted V_{in}'s (see Figure 5.2A). The systematic increase in both peak height and area as a function of ricin concentration demonstrates the quantitative capability of the FGT sensor.

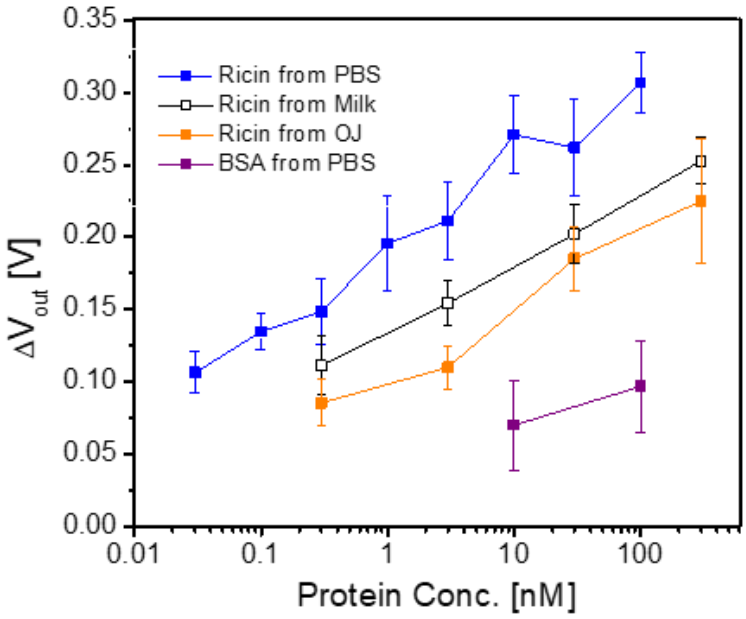

Figure 5.3: Dose-Response Curves.
The maximum ΔV_{out} over one waveform for various protein concentration are plotted. The blue curve is ricin from PBS buffer, the orange is ricin from orange juice, the unfilled black squares are ricin from milk, and the purple curve is BSA from PBS buffer. Error bars represent the standard deviation of 3-5 devices.

The peak ΔV_{out} was used for quantitation and plotted in Figure 5.3. The blue curve is the data when ricin is present in buffer (PBS 1x) and shows a monotonic dependence on ricin concentration. The red curve is the corresponding response when an equivalent concentration of bovine serum albumin (BSA) in PBS flows over the FG-R, representing a control experiment for non-specific adsorption. The negative control signals are ~300x smaller than those for equivalent concentrations of ricin, demonstrating the specificity of the immobilized aptamer and the efficacy of the PEG-SH blocking layer. The limit of detection for ricin is 30 pM (1 ng/mL) and the device requires an exposure of only ~0.5 ng of ricin in order for the surface to be completely covered (as low as 0.5 μL at high concentration). These concentrations and volumes are well within the clinically relevant levels for ricin given that the LD_{50} is ~20 μg/kg-body-weight.[237]

Figure 5.3 shows data for ricin quantitation in orange juice (orange curve) and 2% milk (black curves). The reference device subtracts alterations at the complex media/buffer interface (e.g. liquid/liquid junction potential) so that the resulting signal is only due to changes at the electrode/electrolyte interface.[17] The highest signal obtained from ricin binding in complex media is ~100 mV less than that obtained in clean buffer (at concentrations > 300 nM). The dissociation constant of the aptamer (K_D) is approximately the concentration when ΔV_{out} is half this value, and shifts to higher concentrations when ricin is extracted from complex media (~10 nM compared to 1 nM). These effects lead to a poorer limit of detection for ricin in milk and orange juice of 0.3 nM (10 ng/mL), ten times higher than that for clean buffer. The values of K_D obtained are consistent with previous reports using this aptamer and on par with ricin antibodies.[10] The higher values of K_D in complex media are also expected and are attributed to interference by complex

ions and small molecules in the food matrix with the aptamer-protein complex.[246] On the molecular level, these interactions may alter the conformation of either the aptamer or ricin, effectively lowering the binding affinity of the aptamer-protein complex.[256],[257],[258] Nonetheless, the quantitative range is clinically relevant for ricin and the bypassing of time-consuming filtering, rinsing, and washing steps is a clear advantage of the FGT approach.[237],[249],[259]

The molecular origin of this signal is the excess interfacial charge at the FG-R due to bound ricin.[260] The screening of this excess charge by counter-ions alters the surface potential of the FG-R with respect the bulk electrolyte potential, causing the observed shift[261] even when the Debye screening length of the electrolyte is smaller than the size of the bound protein[261] (Table S5.1). The change in potential across the FG-R interface (ϕ) required to screen interfacial charge (σ) can be approximated by

$$\sigma = \sqrt{8\epsilon\epsilon_0 e N_A V_{thermal} C_{ions}} \sinh\left(\frac{\phi}{2V_{thermal}}\right) \tag{5.1}$$

where ϵ is the dielectric constant of the interface, e is the elementary charge, N_A is Avogadro's number, $V_{thermal}$ is ~25 mV at room temperature, C_{ions} is the concentration of ions in solution, and ϕ is the surface potential of the electrode interface with respect to the bulk electrolyte.[261] For small changes in interfacial properties, Eq. 5.1 is approximately linear. For larger changes, corresponding to larger amounts of bound ricin, non-linear effects become important.[261] Additionally, high coverages of bound ricin can incur non-primary binding sites that alter the interfacial charge distribution and corresponding signal transduction. Future efforts will strive to distinguish nano- and macro-scale non-linearities.[256,257,258]

In summary, we demonstrated quantitative detection of ricin from complex food matrices with a printed FGT. Compared to our previous work on DNA hybridization,[250] the limit of detection of our new approach is nearly two orders of magnitude lower (when corrected for the lower K_D for the ricin-aptamer system) and similar to other methods requiring more time, optical laboratory equipment, chemical labeling, and/or pre-concentration.[237,245,246,248] The improved performance is attributed to noise suppression from reference device integration and AC testing modality[262] along with the specificity provided by the nucleic acid aptamers and precise control of fluid volumes provided by microfluidic patterning. The flexibility of the sensing mechanism to other analytes and antigens will be pursued in future work.

Supporting Information. The supporting information herein begins with an illustrative sample experiment to show the changes in semiconductor current (Figure S5.2)

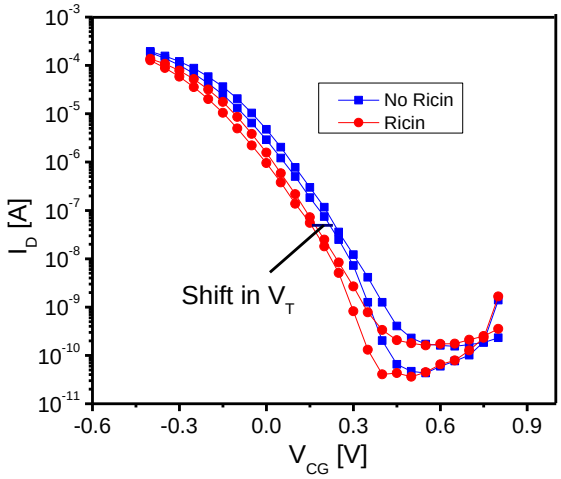

Figure S5.2: Shifts in V_T due to Ricin.
The blue curve is an I_D-V_{CG} trace before ricin exposure while the red-curve is after. The shift in V_T is ~75 mV in this example.

rather than the inverted output voltage in Figure 5.2a in the main text. The following table (Table S5.1) summarizes the signal-to-noise ratio for devices exposed to high concentrations of ricin in solutions of varied ionic strength. The signal is defined as the maximum change in voltage and the noise is the maximum fluctuation from a blank solution. This table illustrates that complete screening of interfacial charge does not drastically inhibit signal transduction. The equivalent circuit in Figure S5.2 represents an upgraded and more advanced circuit from the inverter circuit in Figure 5.1d by including the reference device. The rest of the provided information is dedicated to experimental materials, methods, and design. It includes a schematic (Figure S5.3) that illustrates the relative sizes of the electrodes and microfluidic channels.

Ionic Strength [M]	Signal-to-Background
10^{-7}	7 ± 2
0.01	35 ± 7
0.1	30 ± 6
1	22 ± 5

Table S5.1: Signal-to-Background in Ionic Strength.
The ionic strength of the secondary electrolyte was varied from distilled water (10^{-7} M) to Phosphate Buffered Saline (PBS 10x) (1 M). The signal is defined as the max ΔV_{out} under exposure to high concentrations of ricin (>1 μg/mL). The background is defined as the max ΔV_{out} when the blank buffer is flowed over the floating gate. Error is the standard deviation of 3 devices.

Experimental Methods

Materials. Poly(3-hexylthiophene) (P3HT) was purchased from Rieke Metals, Inc. and stored in an inert environment. 1-ethylmethyl imidazolium bis(trifluoromethyl)sulfonylimide (EMIM/TFSI) was purchased from EMD Millipore, Inc.

and stored in an inert environment. Polystryene-*b*-methylmethacrylate-stryene (SMS) was synthesized by a previously reported procedure by Zhang *et al.*[156] The ion-gel was a mixture of SMS and EMIM/TFSI at 1:9 by weight. Poly(ethylene glycol) methyl ethyl thiol (PEG-SH, M_n = 800) was purchased from Sigma-Aldrich and used as received. Aptamers were purchased from the Integrated DNA technologies with the sequence: HS-C_6H_{12}-5' – ACA-CCC-ACC-GCA-GGC-AGA-CGC-AAC-GCC-TCG-GAG-ACT-AGC-C-3'. Ricin B was purchased from Vector Laboratories.

Device Fabrication. Cr/Au (5 nm/30 nm) electrodes were photolithographically patterned onto a silicon wafer. Organic materials were printed with an Aerosol-Jet 200 Printer (Optomec, Inc.). For printing, P3HT was dissolved in chloroform at 1 mg/ml then terpineol was added as a cosolvent at 0.1 ml per ml of chloroform solution. The solution was printed with a 150 µm nozzle using a carrier gas flow rate of 10 ccm and a sheath gas

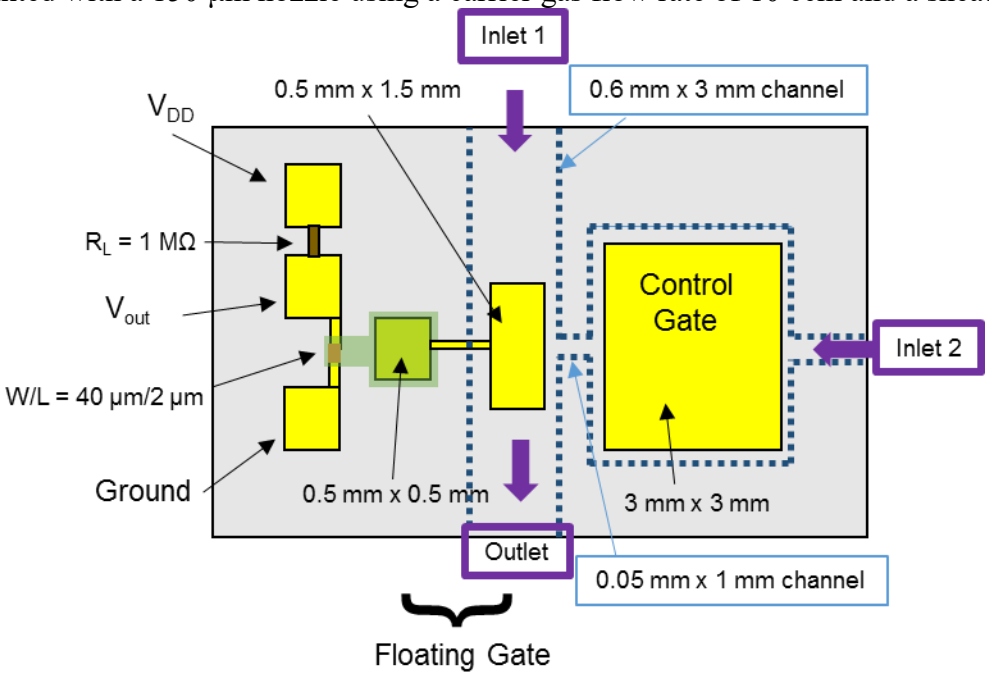

Figure S5.3: Schematic of Floating-Gate Transistor.
The sizes of electrodes are labeled in black, the geometry of microfluidic channels is outlined in blue, and the inlets/outlets are labeled in purple.

flow rate of 20 ccm. The ion-gel was mixed with ethyl acetate at a ratio of 1:9 by weight, stirred overnight, and then printed with a 150 μm nozzle, but with a carrier gas flow rate of 20 ccm and a sheath gas flow of 25 ccm. Poly(styrene) was dissolved in chloroform and terpineol (10:1 by volume) at a concentration of 5 mg/mL with the 150 μm at a carrier gas flow rate of 20 ccm and a sheath gas flow rate of 30 ccm. More details on the printing process have been reported previously.[144]

Microfluidics. Microfluidic flow channels were imprinted into poly(dimethylsiloxane) (PDMS) molds from an SU8 master.[263] The base and curing agent were poured onto the SU8 master at a ratio of 10:1 then heated at 75°C for 2 hours. The imprints were 150 μm high in a pattern that outlined the right arm of the floating-gate electrode and control gate electrode. The imprints over the floating-gate electrode were extended to two inlets/outlets such that a solution injected through one inlet (Inlet 1, Figure S5.3) interacted with the right arm of the floating gate. Another inlet (Inlet 2, Figure S5.3) was imprinted above the control gate so that solution will flow over the control gate to the outlet (Outlet, Figure S5.3).

Interface Functionalization. Once fabricated, the right arm of the floating gate is cleaned by flowing sodium borohydride at 0.5 M for 1 hour, then rinsed with distilled water. Aptamers are then dissolved in Tris buffer with 0.1 M NaCl and flowed over the right arm of the floating gate overnight (>16 hours) to give a resulting coverage of ~2 pmol/cm^2.[264] PEG-SH is then dissolved in distilled water at 1 mM and flowed over the right arm of the floating gate for 2 hours. Finally, the interface was rinsed with buffer. This strategy was used to fabricate the Test Sensor. The Reference Sensor was fabricated in the

same manner but without aptamers so that only the PEG-SH blocking layer was on the floating gate.

Testing. An input voltage ($V_{in} = V_0 + V_1 \sin(\omega t)$) is applied to the control gate of each device. At the same time, the output voltage between the transistor and a constant resistor loaded inverter (R_L = 1 MΩ) is measured. V_1 is fixed at 0.3 V, while V_0 is tuned so that the resistance of the transistor is equal to R_L when $V_{in} = V_0$ (typically, V_0 = -0.1 V to +0.1 V). This way, the resulting ΔV_{out} is approximately zero for all V_{in}. PBS buffer (0.1 M) is then flowed over the right arm of the floating gate at 1 μL/min in one stream (Inlet 1 to Outlet) and over the control gate (Inlet 2 to Outlet) at 0.1 μL/min and while monitoring ΔV_{out} to measure the background. Then, ricin is flowed at 1 μL/min over the floating gate (Inlet 1 to Outlet) at various concentrations in either PBS, orange juice, or milk and ΔV_{out} is monitored until it reaches a stable value for ~10 minutes.

Acknowledgements. We acknowledge funding from the National Science Foundation (Predoctoral Fellowship for SPW), the Office of Naval Research through the Multi-University Research Initiative (CDF) and the David and Lucile Packard Foundation (KDD). A portion of this work was performed at the University of Minnesota Nanofabrication Center which received partial support from the NSF through NNIN.

6. Detection and Sourcing of Gluten in Grain with Multiple, Tunable Floating-Gate Transistor Biosensors

6.1 Abstract

We report a chemically tunable electronic sensor for quantitation of gluten based on a floating-gate transistor (FGT) architecture. The FGTs are fabricated in parallel and each one is functionalized with a different chemical moiety designed to preferentially bind a specific grain source of gluten. The resulting set of FGT sensors can detect both wheat and barley below the gluten-free limit of 20 ppm while providing a source-dependent signature for improved accuracy. This label-free transduction method does not require any secondary binding events, resulting in a circa 45 min reduction in analysis time relative to state-of-the-art ELISA kits with a simple and easily implemented workflow.

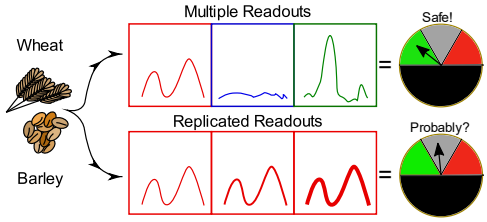

Figure 6.0: Overview Sketch.

6.2 Introduction

Gluten is an umbrella term for a variety of storage proteins found in plants such as wheat, barley, and oats.[265,266] Gluten elicits an allergenic response in people who suffer from celiac disease, comprising ~1% of the population.[267,268] Gluten exposure is a serious health issue for this population, whose collective hospital visits amount to thousands of dollars per patient (billions of dollars in total) due to dietary complications.[269,270] An additional ~10% of the population is suspected to have at least a mild gluten sensitivity.[271]

Enzyme-linked immunosorbent assays (ELISA) are the dominant method for gluten detection[272] but they suffer from poor quantitation,[273] inconsistencies in varied media,[274,275] and variability across manufacturers.[48] The analytical challenge arises from

the variable chemistry of the gluten proteins found in the endosperm of plants such as wheat, barley, and some oats.[265,266] They all share chemical commonalities that trigger an allergenic response in celiac disease but their structural chemistry varies as a function of plant source,[266,276] cultivar,[277] and processing conditions.[278] As a result, different antibodies, such as the Skerrit antibody,[279] the G12 antibody,[53] and the R5 antibody,[53] have been developed for gluten ELISA. Inevitably, different gluten sources have different dissociation constants for a given antibody,[280] making it challenging to establish a gluten-free limit of < 20 ppm in all food sources using a single ELISA test. For example, the Skerrit antibody was developed from an immune reaction to ω-gliadin. While an excellent antibody for detecting ω-gliadin, the Skerrit antibody also binds other gluten sources.[279] When the Skerrit antibody is used as a generic binding agent for gluten, sources that are not dominantly ω-gliadin but otherwise above the gluten-free limit result in false negatives.[281]

The extraction of solid gluten proteins into a liquid matrix poses another considerable challenge.[280] Gluten is generally divided into two fractions: the ethanol soluble prolamin fraction and the insoluble glutenin fraction.[266,277,280] The ratio of these fractions in plants is assumed to be 1:1 but has been reported up to 1.5:1 or 1.7:1 in various conditions.[280] The convolution of the variability of the gluten chemistry and the variability of extracted proteins leads to significant variability when the same sample is tested using different gluten immunoassay kits, up to 50% or even 100%.[48]

The limitations in ELISA have motivated the development of new methods for gluten detection. One approach uses DNA-based sensors for cases where antibody-based methods fail due to changes during food processing, for example during beer

production.[282,283] A second approach replaces the antibody with a DNA aptamer having enhanced stability.[87,284] Impedimetric[285] and electrochemical[286] sensors using DNA aptamers for gluten have achieved improved limits of detection for common gluten samples when compared to conventional ELISA.[287,288] However, the sensitivity of a binding-based assay is always limited by the affinity of the binding agent for the target. If one wants to comprehensively assess the gluten content in food, more sophisticated proteomic methods that do not rely on affinity, such as mass spectrometry, are required[277,289,290] to overcome the limited reactivity of a single binding agent with classes of gluten samples that are not optimal for that binder.[287,291] In addition to detecting the presence of gluten, mass spectrometry can also provide information about the gluten source (e.g. wheat gluten or barley gluten). Unfortunately, current proteomic methods require a substantial increase in time, cost, and operator expertise relative to immunological methods, limiting their impact in practical applications.[282]

Motivated by the limitations of existing methods, we have developed an immunological assay based on floating gate transistors (FGTs) that bridges the gap between ELISA and mass spectrometrometry.[48,277,282] Compared to commercial ELISA kits, our method better quantifies gluten in less time, while also being far easier to use than mass spectrometers due to the minimal number of processing steps and automated sample handling. We have previously shown how this rapid, FGT biosensing technology, which combines printed electronics and microfluidics, leads to a label-free, potentiometric transducer for sensing biomacromolecules such as DNA[3] and proteins.[4,5] In contrast to conventional ELISA methods, the FGT signal depends on intrinsic changes at the sensor surface. As a result, secondary binding events[48,292] are not necessary. This reduces the time

to transduction by at least 30 min, an improvement similar to advanced microfluidic-ELISAs,[293] and also circumvents problems when the secondary epitope is altered during processing, for example when cooking food. Eliminating the need for a secondary binding event also permits detection directly from gluten extraction cocktails, which contain high concentrations of reducing agents that can sometimes interfere with complex protein-protein ligand binding, thereby minimizing the reaction time.[280] The set of FGT sensors developed here represent a developmental step of immunoassays analogous to those by Luminex Multiplex Assays[294,295] but with streamlined manufacturing and operating protocols. By systematically altering the binding chemistry of the sensor and comparing the response as a function of gluten source, we demonstrate that our approach can not only determine the presence of gluten, but also has the sensitivity to provide a chemical fingerprint for the gluten source.

6.3 Experimental Methods

Materials. Poly(3-hexylthiophene) (P3HT) was purchased from Rieke Metals, Inc. and stored in an inert environment. 1-ethylmethyl imidazolium bis(trifluoromethyl)sulfonylimide (EMIM/TFSI) was purchased from EMD Millipore, Inc. and stored in an inert environment. Polystryene-*b*-methylmethacrylate-stryene (SMS) was synthesized by a previously reported procedure by Zhang *et al.*[296] The ion-gel was a mixture of SMS and EMIM/TFSI at 1:9 by weight.

Gliadin (PWG) was purchased from Prolamin Working Group as a mixture of various plant sources.[297] Wheat gluten and barley gluten were obtained from a local Co-op as ground baking ingredients. The gli4 aptamer developed by Amaya-Gonzalez *et al.*[284] was purchased from Integrated DNA Technologies with the sequence: HS-C_6H_{12}-5' –

CCA-GTC-TCC-CGT-TTA-CCG-CGC-CTA-CAC-ATG-TCT-GAA-TGC-C-3'. Wheat antibody G12 was purchased from Biomedal. A custom barley antibody (BAb) was obtained from Pacific Immunology Inc. by sending them the barley extract (from the local Co-op baking ingredient) and receiving the purified immune response of rabbits. The gluten extraction matrix (often referred to as a "cocktail") was an established recipe[280] comprising 250 mM of beta-mercaptohexanol (Sigma Aldrich) and 2 M Guanidine HCl (Sigma Aldrich). 11-mercaptoundecanoic acid and poly(ethylene glycol) methyl ethyl thiol (PEG-ylated thiol, M_n = 800) were purchased from Sigma-Aldrich and used as received.

Device Fabrication. Devices were fabricated using the printing process reported previously[298] by first photolithographically patterning a chrome adhesion layer for gold electrodes (5 nm/30 nm) and then printing the organic materials with an Aerosol-Jet 200 Printer (Optomec, Inc.) using a 150 μm nozzle. For printing, P3HT was dissolved first in chloroform at 1 mg/ml and then terpineol was added as a co-solvent at 0.1 ml per ml of chloroform solution. The solution was printed using a carrier gas flow rate of 10 ccm and a sheath gas flow rate of 20 ccm. The ion-gel was mixed with ethyl acetate at a ratio of 1:9 by weight, stirred overnight, and then printed using a carrier gas flow rate of 20 ccm and a sheath gas flow of 25 ccm. Poly(styrene) was dissolved in chloroform and terpineol (10:1 by volume) at a concentration of 5 mg/mL at a carrier gas flow rate of 20 ccm and a sheath gas flow rate of 30 ccm. More details on the printing process have been reported previously.[298]

Microfluidics. Microfluidic flow channels were imprinted into poly(dimethylsiloxane) (PDMS) molds from an SU8 master.[299] The base and curing agent were poured onto the SU8 master at a ratio of 10:1 then heated at 75 °C for 2 h. The imprints

were 150 μm high in a pattern that outlined the right arm of the floating-gate electrode (FG-R, Figure 6.1C) and the control gate electrode. The imprints over the floating-gate electrode were extended to one inlet port and one outlet port such that a solution injected through the inlet flows over FG-R. Another inlet was imprinted above the control gate so that solution flows over the control gate to the outlet.[5]

Interface Functionalization. Once fabricated, FG-R was cleaned by flowing sodium borohydride at 0.5 M for 1 h, then rinsed with distilled water.

For aptamer functionalization, aptamers were dissolved in Tris buffer with 0.1 M NaCl at 1 μM and flowed over FG-R overnight (>16 h), leading to a coverage of ~2 pmol/cm^2.[300] PEG-ylated thiol was then dissolved in distilled water at 1 mM and flowed over FG-R and the Control Gate for 2 h. Finally, the interface was rinsed with buffer.

For antibody conjugation, FG-R was functionalized first with 11-mercaptoundecanoic acid (-COOH) and PEG-ylated thiol at a concentration of 1 mM in ethanol/water (50/50 v/v) and a acid:PEG ratio of 1:9. The surface was rinsed and then reacted with 1-ethyl-3-(3-dimethylaminopropyl)carbodiimide hydrochloride (EDC) at 5 mM and N-Hydroxysuccinimide (NHS) at 2 mM in MES buffer for 15 min. Following the reaction, the surface was rinsed with phosphate buffered saline solution. The activated surface was then exposed to an antibody solution at a concentration of 0.1 mg/mL for 2 h to form an amide bond with the -COOH groups on the electrode surface.[301] The concentration of the protein solutions was confirmed using a Thermo-Fisher Nanodrop to measure the absorbance of protein solutions at 280 nm.

These strategies were used to fabricate the Test Sensor. The Reference Sensor was fabricated in the same manner but without aptamers (or antibodies), so that only the PEG-ylated thiol blocking layer was on the floating gate.

Testing Protocol. The gluten samples were extracted with the extraction cocktail following established protocols.[280] For the PWG gliadin sample, the powder was simply massed and then diluted to a desired concentration followed by vortex mixing. For the wheat and barley samples, 100 mg were massed and then diluted in 1 mL of extraction cocktail, vortexed, allowed to dissolve at room temperature for 30 min, and centrifuged for 10 min. The resulting solution was diluted to the desired protein concentration based on the gluten concentration determined by ELISA.

To measure a baseline, the microfluidic channels on a test and reference FGT were first filled with extraction cocktail without any gluten sample. An input voltage, $V_{in} = V_0 + V_1 \sin(\omega t)$, was applied to the control gate of each device (Figure 6.1C). At the same time, the output voltage between the transistor and the resistor (R_L = 1 MΩ) in Figure 6.1C was measured. V_1 was fixed at 0.4 V, while V_0 was tuned so that the resistance of the transistor was equal to R_L when $V_{in} = V_0$. Typically, this requires that V_0 be between -0.3 V and+0.3 V. The resulting $\Delta V_{out} = V_{out,\ Test\ FGT} - V_{out,\ Ref.\ FGT}$ is then approximately zero for all V_{in}. The frequency is ω = 13 Hz. The measurement was repeated 5-10 times at a rate of once per min. This procedure is very similar to that reported elsewhere.[5]

The equivalent circuit for our device is outlined in Figure 6.1B. The resulting ΔV_{out} waveforms are averaged and recorded as the "blank" in Figure 6.2A. This step occurs during the centrifugation or dissolution of the gluten sample.

In the second step of the measurement, FG-R was exposed to the gluten sample through microfluidic sample delivery for 30 min at a rate of 1 μL/min, and then rinsed with blank extraction cocktail. The flow was stopped and then the same input waveform used in the first step was applied for 5-10 min at a rate of once per min. The resulting ΔV_{out} waveforms were averaged and the peak ΔV_{out} was recorded as the signal corresponding to the input concentration of gluten.

ELISA. GlutenTox® Sandwich ELISA kits were purchased from Biomedal and used according to the manufacturer protocol.[292]

6.4 Results

The FGT biosensor is depicted in Figure 6.1. The sensors are fabricated in parallel with each "pixel" defined by the chemistry of the sensor surface (Figure 6.1A). The core of the sensor is a floating gate electrode with two arms. The left arm (FG-L) is connected to a printed semiconductor (poly(3-hexylthiophene) or P3HT) via an ion-gel electrolyte that permits very low voltage operation (<1 V) (Figure 6.1A-C).[3,5,298] The right arm (FG-R) is connected to the microfluidic network via an aqueous electrolyte that, in this work, is an extraction cocktail that solubilizes gluten proteins in food samples (250 mM of beta-mercapto hexanol and 2 M of guanidine HCl in water).[280] The gluten extract is contained by PDMS microchannels that guide the flow of the sample over FG-R only (Figure 6.1C). The flow decrease the binding time relative to ELISA by at least 15 min.[293]

The sensor surface on FG-R is functionalized to specifically capture gluten from the extract while minimizing non-specific adsorption. The capture agents were: (i) an aptamer (gli4) designed to bind the active 33-mer epitope of gluten developed by Amaya-

Gonzalez *et al.*;[87,287] (ii) the commercially available G12 antibody generated to bind wheat gluten;[53] and (iii) a custom barley antibody developed by Pacific Immunology Inc. (BAb).

Upon binding, the gluten proteins are concentrated at the sensor surface, raising the interfacial charge;[4] the high proline content of soluble gluten renders it negatively charged at neutral pH.[266] This alteration in interfacial charge distribution changes the surface potential relative to the bulk of the aqueous electrolyte, illustrated schematically by the voltage shift δ in Figure 6.1D.[299] The potentiometric perturbation alters the output of the device at a given V_{in}. The experiment is conducted on a Test Sensor and a Reference Sensor in parallel, leading to the equivalent circuit in Figure 6.1B. The output of the device is obtained as the difference between the responses of the two devices, which we denote as ΔV_{out}.

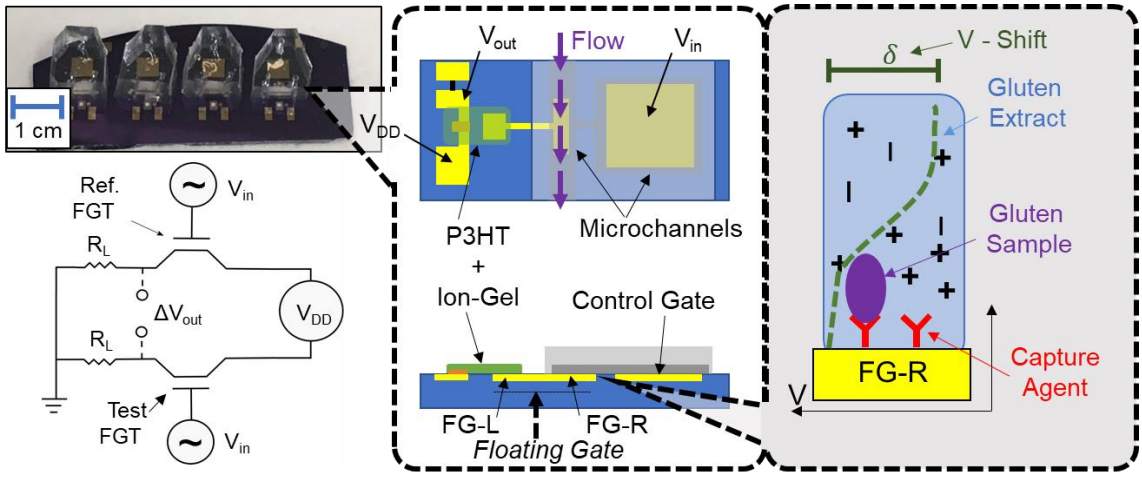

Figure 6.1: Device Architecture.
(a) Photograph of a set of FGTs. **(b)** Equivalent circuit for a pair of FGTs that are placed in parallel with a load resistance (R_L) and a driving voltage (V_{DD}) set across them. The Reference FGT is functionalized with only PEG-ylated thiol while the Test FGT has PEG and chemical binders for gluten. The input voltage (V_{in}) modulates the conductivity of the FGTs and the response is read as a ΔV_{out} between the two sensors. **(c)** Schematic of a single FGT with materials and electrodes labeled along with the flow path of the sample. **(d)** Schematic illustration of the active sensor surface with a capture agent (antibody or aptamer) on FG-R. The binding of gluten to the surface causes a change in the potential (green curve) that leads to a voltage shift.

For our experiments, we would like to determine the relationship between ΔV_{out} and the gluten concentration. This requires knowledge of the mass fraction of gluten in the grain sample and the solubility factor,

$$C_{\mathrm{i}}^{*} = \frac{m_0 X_0 f_0}{(1+D)V_0} \tag{1}$$

where m_o is the mass of grain, V_0 is the volume of extraction cocktail, f_0 is the fraction of gluten that is soluble in the extraction cocktail (assumed to be 0.5 here[266]), X_0 is the weight fraction of gluten in the stock (w/w) determined from standard ELISA kits, D is the dilution, and C_i^* is referred to as the "true concentration" of gluten exposed to an FGT with functionalization i (i = Apt, G12, or BAb). We used two sources of grain gluten: wheat and barley. The gluten mass fractions of these sources were measured with a GlutenTox® ELISA kit to be $X_0^W = 1.3\%$ (w/w) in wheat and $X_0^B = 0.5\%$ (w/w) in barley.[292] Due to this disparity in gluten concentrations of the food material, the extracted supernatants were diluted differently (see Methods) in order to set the gluten concentration C_i^* exposed to the sensor to be within the desired range.

Note that, with this protocol, we are operating under the assumption that the ELISA kit provides an accurate measure of X_0. Ultimately this is not a limitation in our method, as it simply provides a convenient standard for plotting the gluten concentrations for the data that follow. We will discuss shortly how to operate the sensor without the need to calibrate it with an ELISA measurement.

Figure 6.2A shows the device output for a specific example where FG-R was functionalized with the gli4 aptamer. In these experiments, the microchannels were filled

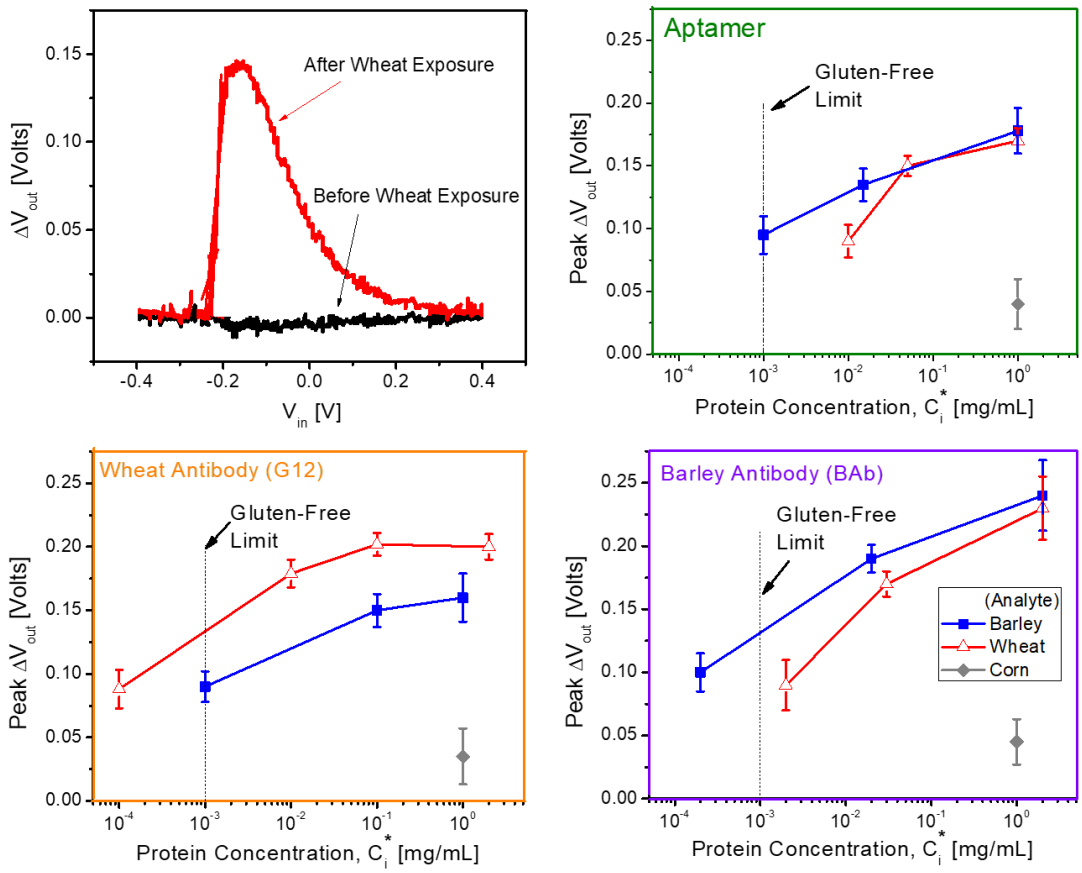

Figure 6.2: FGT Response.
(a) Example of the device response of an FGT functionalized with aptamers and exposed to wheat at 0.1 mg/mL. The curves are averaged over 5-10 min of testing. Dose-response curves for **(b)** an aptamer-functionalized FGT, **(c)** a G12-functionalized FGT and **(d)** a BAb-functionalized EGT when exposed to the wheat (red open triangles), barley (blue closed squares), and gluten-free corn (gray diamonds). Error bars are the standard deviation for 3 devices. The gluten concentrations on the x-axis of **(b)-(d)** are given by Equation 1 at various dilutions as determined by a GlutenTox® ELISA kit.

first with a blank extraction cocktail. A supply voltage of + 0.5 V was input at V_{DD}. The input voltage at the control gate was swept from +0.4 V to -0.4 V around a DC-bias. The value of the DC bias was tuned for each device to maximize the gain of the differential amplifier scheme and is 0.0 V for the example in Figure 6.2A. The output voltage is measured at V_{out} (Figure 6.1C), using a 1 MΩ resistor in series. The black data in Figure 6.2A show the result of this measurement of a blank sample. These curves vary about zero

with fluctuations of ~25 mV (see Supporting Information). Following this baseline measurement, FG-R was exposed to a gluten sample for 30 min. In this experiment, the sample was gluten extracted from wheat and diluted to a concentration of C_i^* = 0.1 mg/mL. The red data in Figure 6.2A show the output of the device when exposed to the gluten sample. The displayed curve is constructed by subtracting the output of the reference device from the test device each min for 5-10 min and then averaging the resulting curves. The maximum value of the red waveform is the value of ΔV_{out}; we thus conclude that ΔV_{out} = 0.15 V for wheat gluten at C_i^* = 0.1 mg/mL using an aptamer-functionalized FGT.

We repeated these measurements for different gluten sources over several orders of magnitude of total protein concentration using two antibodies and a DNA aptamer. For each gluten source and binding agent, the FGT response was measured at (i) the limit of detection (0.1–1.0 μg/mL); (ii) above the gluten-free limit (10-100 μg/mL); and (iii) a very high concentration outside the quantitation regime (≥ 1 mg/mL). As a control experiment, we also used corn (non-celiac active) as a gluten-free food sample. Control experiments measured signals that would correspond to gluten samples at 3-4 orders of magnitude lower concentration.

The aggregated data are shown in Figure 6.2: aptamers in Figure 6.2B (green highlight), wheat antibody (G12) in Figure 6.2C (orange highlight), and barley antibody (BAb) in Figure 6.2D (magenta highlight). Each sensor was exposed to two different sources of grain: ground wheat from a local Co-op (red open triangles), and ground barley flakes from a local Co-op (blue squares) yielding the six curves shown in Figures 6.2B-D. The concentration displayed on the x-axis of Figure 6.2B-D, C_i^*, corresponds to the value we expect to have in the solution based on the gluten content measured by ELISA following

Equation 6.1. The gluten samples were detectable below the gluten free limit on at least one of the FGT sensors. With the exception of the detection of wheat using the G12 antibody (Figure 6.2C), we obtained points that appear to be in the quantitative regime of each sensor. Rigorously pinpointing these boundaries would require ~5-10x more data, and the concomitant technological advancements that will enable the requisite higher throughput for both device manufacture and measurement will be a focus of future work.

6.5 Discussion

Figure 6.2 makes clear that the value of the measured signal ΔV_{out} for a given capture agent depends on the gluten source. For example, in Figure 6.2C (orange border), the wheat antibody elicited the strongest response from wheat and a considerably lower response to barley. The opposite trend is observed in Figure 6.2D (magenta border) with BAb eliciting a stronger response to barley relative to wheat. These results are expected, as these antibodies were developed to best bind a particular gluten source.

The dependence of the signal on the gluten source can be exploited to source the gluten in a sample. In order to execute this task, the measured signals need to be compared to a reference material within the quantitation regime of the respective dose-response curves. There is no consensus reference material for gluten,[297] so we used the PWG gliadin in order to discriminate the relative signals of wheat and barley samples.

Figure 6.3 is the calibration curve with PWG exposed to each FGT functionalization at various dissolutions. The x-axis is presented as a protein concentration that refers to the concentration of the PWG standard obtained from Equation 6.1 with the assumptions that the PWG solid is 100% gluten and completely soluble ($X_0^{PWG} = 1.0$, $f_0^{PWG} = 1.0$). The curves in Figure 6.3 correspond to the different FGT functionalizations

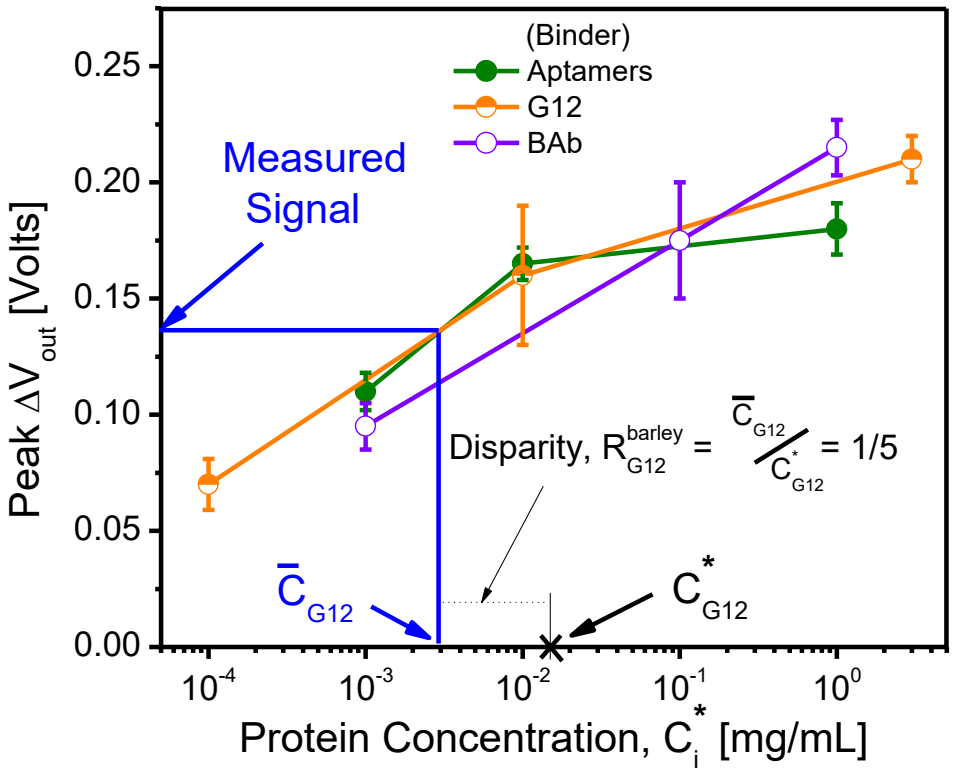

Figure 6.3: Calibration Curve.
The peak ΔV_{out} is plotted with respect to the PWG protein concentration for the three different binders: aptamers in green filled circles, G12 antibody in orange half-filled circles, and BAb in magenta open circles. An example is shown in blue where the measured signal for a barley sample is connected to a measured concentration, $\bar{C}_i$, that is 5x lower than the actual concentration, C_i^*.

(green filled circles for aptamers, orange half-filled circles for G12, and magenta open circles for BAb). Note that the latter curves overlap much more than those in Figure 6.2, reflecting the utility of using PWG across many gluten binders and the reason why PWG has been adopted in many studies as a reference gluten material.

We can use the data in Figure 6.2 and Figure 6.3 to construct a fingerprint for the gluten source based on the measurement disparity between the FGT with functionalization i and the concentration C_i^* obtained from ELISA and Eq. 6.1. To do so, we assume that we know the relevant boundaries of the quantitation regimes for each binder-analyte pair. In

this regime the measurement disparity depends only on the gluten source not the (unknown) concentration. The signal ΔV_{out} from FGT functionalization i when exposed to a gluten concentration C_i^*, can be compared to the concentration of PWG, $\bar{C}_i$, that elicits the same signal ΔV_{out} from FGT functionalization i. To provide a concrete example, this is indicated by the blue line in Figure 6.3 where the ΔV_{out} that produced a C_{Apt}^* = 15 µg/mL when the aptamer-functionalized FGT is exposed to barley gluten (Figure 6.2B) produces a $\bar{C}_{Apt}$ = 3.0 µg/mL for the aptamer-functionalized FGT exposed to PWG. This disparity is represented by the ratio

$$R_i^s = \bar{C}_i / C_i^* \quad (2)$$

where R refers to the disparity from FGT functionalization i when it exposed to gluten from grain source s. The example in Figure 6.3 yields $R_{Apt}^{barley} = \bar{C}_{Apt} / C_{Apt}^* = 1/5$, assuming both $\bar{C}_{Apt}$ and C_{Apt}^* lie in the quantitation regime of their respective curves. A high value of R_i^s means the FGT functionalization i more strongly prefers the target gluten s relative to the PWG standard because a larger amount of PWG ($\bar{C}_{Apt}$) is required to elicit the same FGT signal as the grain gluten (C_{Apt}^*).

Figure 6.4 presents the resulting signal disparities from Equation 6.2 as a function of FGT functionalization and gluten source, which we can interpret as chemical signatures for wheat and barley produced by the FGT sensor. The inset shows the concentration of gluten exposed to the sensors (C_i^*) for the disparity calculation and is assumed to reside in the quantitation regime of the sensors (C_i^* = 1-30 µg/mL). For clarity, ratios less than one are oriented downwards. With this convention, a large up-oriented bar means the FGT functionalization binds more strongly to the gluten

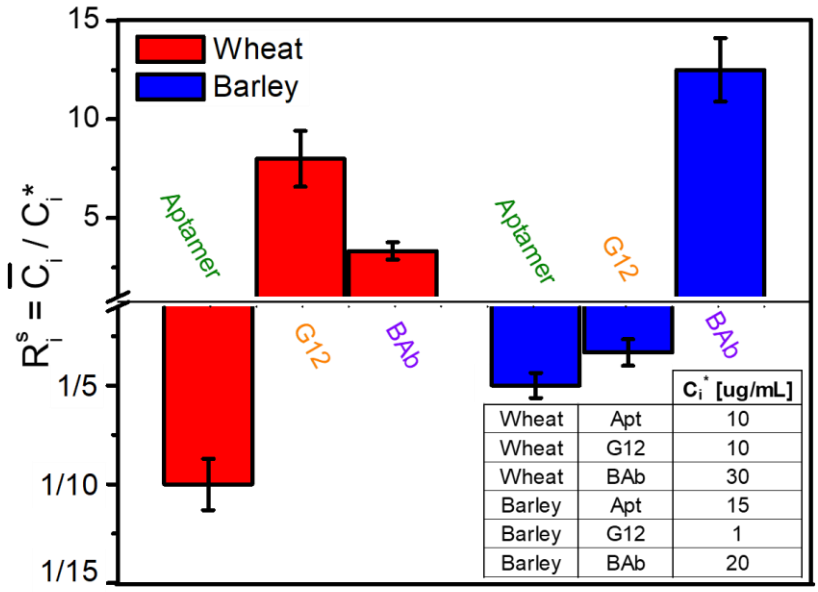

Figure 6.4: Gluten Signatures.
The resulting ratios (R_i^s) of measured concentration ($\overline{C}_i$) relative to the initial concentration (C_i^*) are presented when the set of FGTs are exposed to wheat gluten (red bars) and barley gluten (blue bars). Up-oriented bars represent a stronger preference for wheat/barley relative to the PWG standard. The inset lists the initial concentrations (C_i^*) used from Figure 6.2.

source rather than the PWG reference. A down-oriented bar means the FGT functionalization binds more strongly to the PWG. The red bars represent the disparities from wheat gluten and highlight the preference of G12 and BAb to bind wheat gluten relative to the PWG reference while the opposite is true for aptamers. The blue bars represent the disparities for barley gluten and highlight the ability of BAb to strongly transduce barley gluten relative to the reference PWG while both aptamers and G12 prefer the PWG reference.

The phenomenon in Figure 6.4 arises naturally from the procedures used to synthesize the different binders.[53,87,279,284] The custom barley antibody (BAb) was extracted from an immunogenic response to the very same barley source used in this report. As such, it binds much more strongly to the barley gluten relative to the other analytes.[87] However,

this strong specificity is expected to be very limited and should not be extrapolated to other sources of gluten, even other barley sources of gluten. The G12 functionalized FGT yields the strongest response to wheat gluten which also reflects the origin of the binder as a product of an immune response to wheat gluten.[53] Unlike the BAb, the wheat source for G12 was more generalizable resulting in a broader reactivity profile for G12 compared to BAb and relatively lower preference for G12 compared to the preference of BAb to barley. In isolation, these binder features have their pros and cons but a set of sensors can leverage them to simultaneously assess the source and amount of gluten under investigation.[291,294]

For routine analysis, using a set of FGTs can improve further the accuracy of gluten quantitation by combining the disparities in Figure 6.4 with the raw device responses in Figure 6.2 and Figure 6.3. When exposed to an unknown amount of gluten from an unknown grain source, C, the set of FGT sensors will yield three values of $\overline{C_\iota}$ that can be extracted from the known calibration curves (Figure 6.3). The measured values of $\overline{C_\iota}$ can be then be equated to C with disparities, $\bar{R}_i = \overline{C_\iota}/C$,

$$\bar{C}_i = \bar{R}_i C \quad \text{for } i = 1,2,\ldots,n \tag{6.3}$$

Equation 6.3 is valid provided the measured values of $\overline{C_\iota}$ are in the quantitation regime. This is not a particularly strong restriction, since its satisfaction can be ensured through serial dilutions of a high concentration sample. With an unknown value of C, Equation 6.3 is underspecified, having n independent equations for $n + 1$ unknowns, in effect leaving the unknown concentration undefined. In this work we used n = 3 but the procedure is generalizable to an arbitrary number of FGT functionalizations.

To estimate the unknown concentration *C,* as well as the source of gluten, we also require a library o*f* k reference R_i^S values, such as what we obtained in Figure 6.4 using k

= 2 gluten sources and three FGT functionalizations. To complete the set of equations, we vary C such that the resulting disparities satisfy

$$\min \sum_i \left(\bar{R}_i - R_i^S\right)^2 \tag{6.4}$$

for each source s in the library, yielding k estimates for C and residuals from Eq. 6.4 corresponding to each of those k estimates. The source s whose minimization yields the smallest residual is identified as the source of the gluten, and the corresponding value of C from that minimization is the gluten concentration.

The resulting value of C will be more accurate than any of the measured values, $\bar{C}_i$, because it properly accounts for the disparity in measurements due to source-dependent gluten chemistry. Additionally, the set of R_i^s in Figure 6.4 that minimizes the error provides strong evidence of the source of the gluten sample which can be useful for identifying the cause of an unexpected contamination. Naturally, this approach improves as the size k of the library increases.

In food safety applications, choosing an appropriate set of functionalized FGTs can minimize both false negatives and false positives. For example, if an unknown sample yielded $\bar{C}_i$ values both above or below the gluten-free limit then the set of $\bar{R}_i$ found from Equation 6.3 would result in a more accurate measure of concentration C, that pinpoints it in the proper regime. This practice also alleviates the challenge of identifying a proper gluten reference material provided the standard used in the FGT kit has previously been calibrated using a more accurate proteomic method.[297] While we used ELISA as the benchmark to produce the data in Figure 6.4, one could use a more sophisticated method such as mass spectrometry to produce more reliable data for the library of R_i^s values.

6.6 Conclusions

In this work, we have leveraged the parallelizability and versatility of FGTs to create a set of sensors for gluten detection and sourcing. In the present prototype method, the analysis takes ~1.5 h to quantify a raw food sample – a reduction of ~45 min compared to commercial, optimized ELISA kits. Further work will compartmentalize the electronics equipment and fluidic handling system in order to parallelize the measurement protocols to create a fully multiplexed FGT sensor for gluten. In such a device, the time and effort required to measure the response at one FGT pixel will be equivalent to the measurement of *n* FGTs. The dose-response curves in Figure 6.2 will be further resolved and the signal disparities for other gluten sources (e.g. oats) will be combined to the signatures in Figure 6.4. The expanded capabilities will advance the analytical capabilities of the food sector leading to safer products for the public.[291]

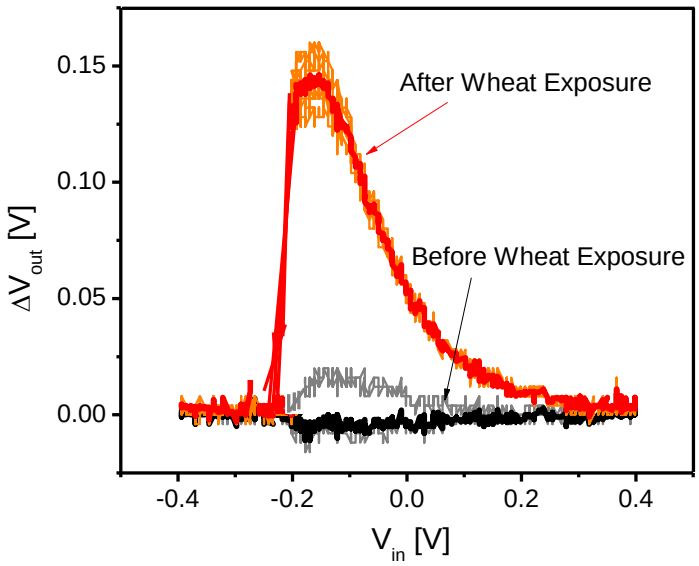

Figure S6.1: Individual Traces for Sensor Response.
An example of the device response of an FGT functionalized with aptamers and exposed to wheat at 0.1 mg/mL, the same case as the device shown in Figure 6.2A. The gray traces are recorded every minute for 5 min before wheat exposure. The black trace is the average of all the gray traces. The gray traces fluctuate about the average by ~25 mV. The orange traces are recorded every minute for 5 min after wheat exposure. The red trace is the average of all the orange traces. The orange traces fluctuate about the average by ~30-40 mV.

7. Future Directions

Various pathways for continued work are laid out in the final chapter of this thesis. They are organized by research topic and research timescale. However, the impact or difficulty of the work does not necessarily scale with the timeline of the work. Some potential obstacles are identified along with corresponding solutions. Of course, the solutions should be considered with only a limited degree of confidence as the path of research is incredibly difficult to predict.

7.1 Advancements in Electronic Performance

Gain. The results presented so far exhibit gains on the order of 1-2 with gain defined as the measured change in voltage divided by the intrinsic potentiometric perturbation due to molecular binding (gain $\cong \Delta V/\delta\phi$).[5] Improvements in this sensor metric directly translate to lower limits of detection due to an enhanced signal-to-noise ratio. This assumption holds provided the noise is not amplified in tandem with the signal amplification. For this reason, the improvements of gain need to come as close to the source of the signal as possible in contrast to downstream circuitry amplification. Improvements in device gain can be achieved by three independent pathways: improved EGT materials and architecture, reduction of parasitic capacitance, improved signal extraction. The results of these experiments are independent so that success in each pathway expands the gain additively.

The most straightforward improvement in gain can be achieved by substituting the P3HT semiconducting film with a higher mobility material that conserves the high capacitance of the dielectric layer ($gain \sim \mu C_i$).[302] Various oxides of Zinc and Indium have

demonstrated mobilities approaching 10 cm^2/V-s or approximately ten times higher than that exhibited for P3HT.[303,304] These have also been demonstrated to be compatible with the aerosol jet printing technique outlined previously.[303] However, the long-term stability of these devices under ambient conditions is still subject to research and will likely require an encapsulation layer of polystyrene to be usable.[305] Additionally, as addressed in the introduction, the specific capacitance of the ion-gel depends on the properties of the semiconducting film.[306] Specifically, whether the gating action is governed by electric double layer formation or it exhibits three-dimensional doping. I estimate the gain can be improved by a factor of 2-10 by optimization of semiconducting/dielectric materials.

Along with material substitution, the device architecture of the FGT strategy can converted from a resistor loaded inverter to a complementary inverter outlined in Figure 7.1. The gain of a resistor loaded inverter is limited by the FGT switching conductivity about the constant value of the resistor. In a complementary inverter, the resistor is replaced with an EGT with semiconductor polarity opposite of the test FGT (e.g. n-type EGT vs. p-

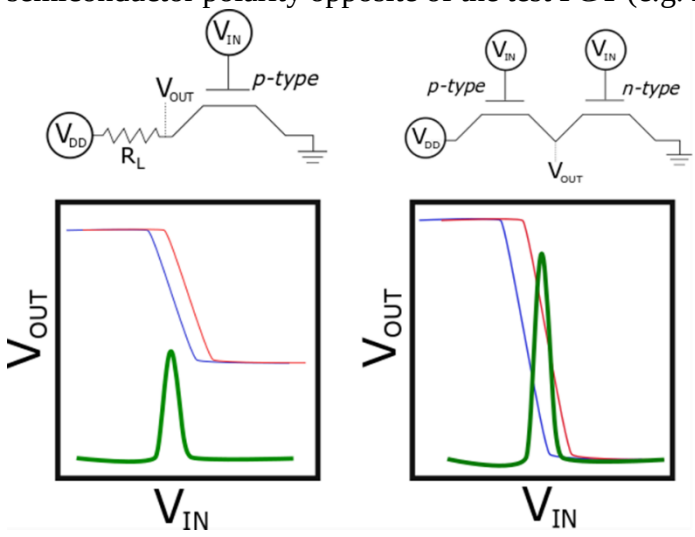

Figure 7.1: Complementary Inverter.
The incorporation of an inverse polarity transistor will amplify the gain of the FGT scheme as outlined in green.

type FGT).[303,304] The corresponding perturbation of the FGT is amplified by shifting it out of phase with the baseline complementary inverter (before analyte addition). I estimate the gain will improve by a factor of 2-5 upon complementary inverter incorporation. The addition of a complementary EGT complicates the fabrication procedure and device operation but the challenges are certainly surmountable given our previous successes.[5]

Finally, improvements in gain can be achieved by chemical labeling. This strategy parallels those used by E-AB sensors by amplifying an intrinsic change in molecular properties through an additional chemical that leads to multiplicative changes in the relevant property.[307] The results presented in Chapter 4 suggest that interfacial charge exhibits the strongest sensitivity to device output.[4] The strategies followed by E-AB sensors suggest the labeling can take place under two mechanisms: the charged label can be bound to the analyte before it reaches the sensor surface, or it can be tethered to the surface and reconfigured upon analyte binding[85,308,309] (See Figure 7.2).

The more successful pathway for E-AB sensors is the tethering mechanism and is expected to transfer for FGT amplification.[84] To appreciate this strategy, note that the potentiometric perturbations due to analyte binding are changes between an interface with only chemical binders and an interface with chemical binder/target analyte complexes (i.e. not simply without and with an analyte). As such, significant amplification could be observed if the binding of a target analyte triggered the release of a molecule with opposite charge polarity of the target analyte. The proposed scheme is outlined in Figure 7.2 where a positively charged chemical is reversibly bound to the specific binder and is released when the negatively charged analyte displaces it. The corresponding gain improvements are expected to be multiplicative so that a change from +q to -q results in at least a 2-fold

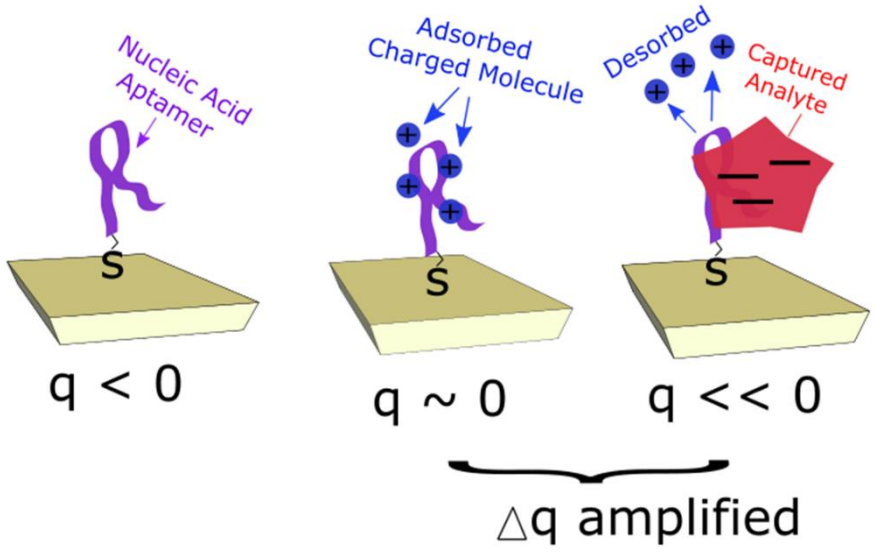

Figure 7.2: Reversible Electrochemical Labeling.
The left panel shows an electrode surface functionalized with aptameric binders. The middle panel shows adsorbed electrochemical molecules that are desorbed when the analyte is bound in the right panel.

improvement in gain relative to a change from 0q to -q. To demonstrate this principle, I would suggest utilizing a DNA aptamer as the chemical binder and a negatively charged protein as the target analyte. Ruthenium Hexamine (RH) could then be reversibly bound to the tethered aptamers before protein exposure and released when they are bound.[310] Potential problems include the diminished binding affinity of the binder when amplification labels are complexed (poorer detection limits) and insufficient release of labels when the target is bound (leading to no amplification). However, the alternative scenario is possible where the addition of positive ions leads to a higher binding affinity with the negatively charged analytes.

Improved manufacturing processes. The promise of printed electronics and solution processable materials is their enhanced manufacturing capabilities. Specifically, their potential to be fabricated on a cheap, flexible substrate in a continuous process. At

present the FGTs are printed in a "semi-batch" process with ~20-30 FGTs manufactured at a time. The difficulty to transition this process to a continuous mode rests on the benchtop aerosol jet printer. The equipment used in this work is designed primarily for rapid prototyping with pronounced manufacturing flexibility (easy to change materials, speeds, etc.) at the sacrifice of throughput.[115,129] Realizing the full potential of the manufacturability promised by printed electronics requires a transition to a high throughput, roll-to-roll (R2R) processing line. This requires three improvements presented with increasing difficulty: transfer to a flexible substrate, multi-layer registration of EGT materials, and continuous manufacturing of the microfluidic system.

The compatibility of EGT materials with plastic substrates has already been demonstrated but the incorporation of microfluidics is less certain. The current methods utilize an oxygen plasma treatment to irreversibly bond the PDMS channels to the wafer substrate. Transferring this procedure to organic or plastic substrates requires chemical functionalizations of substrate/PDMS interfaces with a "chemical glue" such as amine and/or carboxylic acid terminated monolayers that for an amide bond upon exposure.[299,311]

Multi-layer registration of printed materials is an ongoing challenge in printed electronics manufacturing.[124,312] The FGT presents stringent requirements on spatial resolution with the P3HT film only measuring ~20 μm x 50 μm.[5] The Frisbie and Francis groups at the University of Minnesota have recently acquired a R2R printing line that has manufactured single-layer, single material arrays of resistors embedded in plastic (unpublished). Expanding these capabilities to printed FGTs represents a considerable, but surmountable challenge for aerosol jet printing with a R2R manufacturing line.

An alternative manufacturing strategy involves capillary flow of solution processable materials into microfabricated channels embedded into a flexible plastic. The technique is termed Self-Aligned Capillary Assisted Lithography for Electronics (SCALE) and has demonstrated the fabrication of fully printed devices.[313] The principle obstacle to transfer SCALE technology to FGT biosensors lies in the active sensor surface. The published results utilize monolayers formed on evaporated gold that is approximately planar.[3,5] However, the electrodes deposited via SCALE result in very rough surfaces of silver or copper.[313] The successful implementation of FGT biosensors into SCALE requires a robust implementation of monolayer formation onto these non-ideal surfaces. Optimistic scenarios anticipate little complications when utilizing thiol SAMs on rough electrode implemented via SCALE. However, more likely scenarios warrant sophisticated construction of tethered chemical binders and a more robust passivation layer to prevent non-specific adsorption. Polymer brushes present a promising approach that have versatile chemistry for various substrates and profound passivation capabilities.[314]

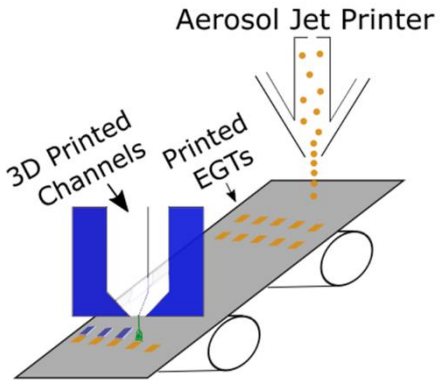

Figure 7.3: R2R Manufacturing.
The aerosol jet printing technique is compatible with an R2R manufacturing line. A 3D printer could be incorporated downstream to fabricate a complete FGT in a continuous process.

Continuous manufacturing of microfluidic channels can be achieved by incorporating 3D printing techniques. 3D printers are a very nascent, promising technology that is commonly used in prototyping or batch processing.[315,316] However, the incorporation of 3D printing into a R2R line is far from fundamentally prohibited. 3D printing of microfluidic channels has been demonstrated with spatial resolutions that far exceed the requirements of FGT biosensors.[315–317] Obstacles remain including the compatibility between the printed material and the underlying substrate in terms of bonding strength but they material flexibility of 3D printers presents many viable candidates such as poly-ethylene-glycol-diacrylate (PEG-DA).[315] As a result, the realization of 3D printed microfluidics in a R2R line is a very promising, viable strategy for improved manufacturing of FGT biosensors.

3D electrodes for improved mass transfer. A principle feature FGT biosensors and next-generation biosensors are their improved speed or reduced time-to-transduction compared to conventional methods.[318–320] The current FGT technology minimizes time by reducing mass transport limitations to the active surface and bypassing chemical labeling steps. However, transport of analytes to the surface remains the dominate fraction of the testing time. It scales with the reaction binding constant and concentration of the analyte ($\sim 1/kC$ where $k \sim 10^6$ $M^{-1}s^{-1}$ and $C \sim 10^{-9}$ M resulting in a test of ~0.5 hours).[321] Improvements in this reaction rate can be achieved by increasing the effective area of transport by increasing the dimensionality with a 3D electrode as the sensor surface.[320] These improvements are, at a minimum, expected to scale by an exponent of 3/2. A 100 second test with a planar sensor surface would take ~20 seconds with the increased

dimensionality.[321] Electrochemical sensors have benefitted from this technique by using nanostructured electrodes.

The fabrication of 3D electrodes is constrained by the microfluidics and presents a challenging research problem. The ideal design is depicted in Figure 7.4. and resembles a packed-bed reactor with gold nanoparticles packing the microfluidic channel with surfaces functionalized with chemical binders.[322] Important design parameters include the particle size and the void space of the channel. Small void space and the corresponding small distance between particles will decrease the transport time to the activated surface.[323] However, small void spaces require substantial pressures to drive flow through them which is constrained by the binding strength of the channels to the substrate.[321] The improvements to the FGT performance would be transformative if the 3D electrodes were incorporated.

7.2 Expansion to other Biological Problems

Whole Cell Detection. The current results represent the successful transduction of DNA[3] and proteins.[5] The expansion to whole cell detection would drastically expand the application of FGTs and allow its features to be applied to infection monitoring,[324] food

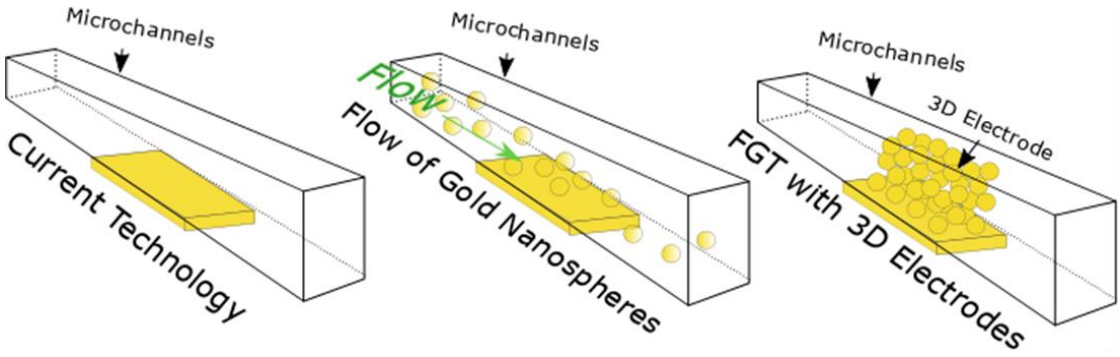

Figure 7.4: 3D Electrodes.
The planar technology (left panel) will be subjected to gold nanoparticles in solution that coalesce onto the FG surface. The resulting suspension of particles form a 3D electrode (right panel) that is formed from a technique such as chemical tethering or smelting.

microbiology,[325] and environmental monitoring.[19,326] Next generation sensors for cellular detection have been limited and typically target biomarkers of a specific species like Shiga toxins.[327] The current working model of FGT biosensors suggests that whole cells specifically bound to the sensor surface would yield clear, discernable signals. The intracellular potential of bacterial cells is ~70 mV due to differences in charge concentration inside the cell versus outside.[328,329] This is expected to shift the threshold voltage of the FGT commensurately. Complications arise from the quantitative relationship between (i) the number of cells in solution, (ii) the number of cells bound to the surface, and (iii) the resulting signal.[328–330] The relationship between the cells in solution and those bound on the surface is expected to follow one of a variety of isotherms but in a highly

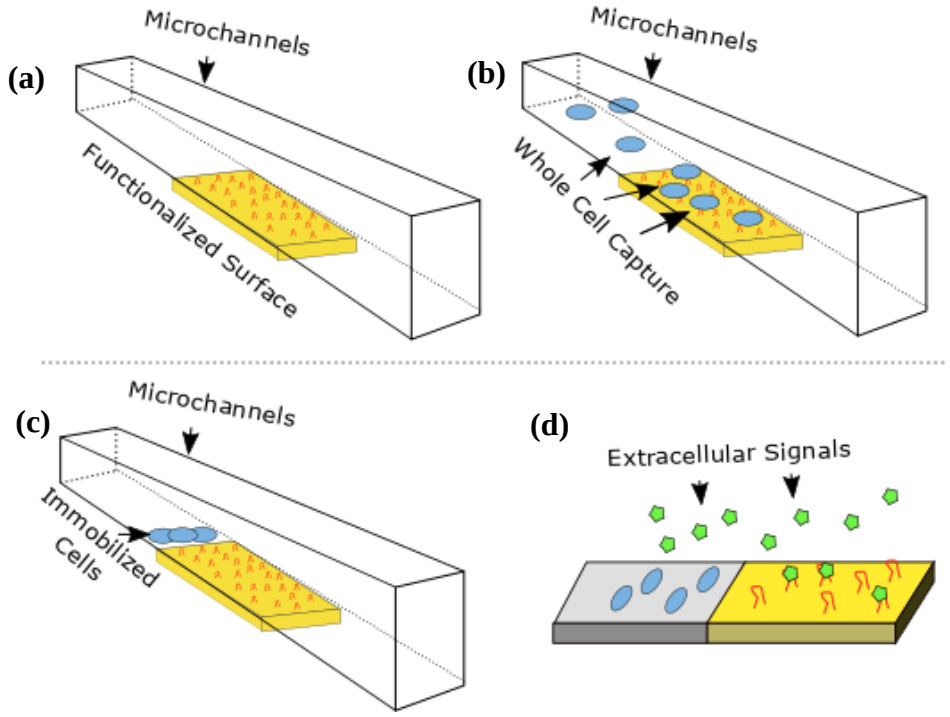

Figure 7.5: Cellular Detection.
(a) shows the microfluidic channel over a functionalized sensor surface. The surface can then be exposed to whole cells in solution in the standard FGT format in (b). Alternatively, the cells can be immobilized near the surface in (b) and extracellular signal can diffuse out and onto the surface in (d) leading to an *in-situ* measurement of extracellular signaling.

non-ideal fashion due to the formation of biofilms or interactions between neighboring surface-bound cells.[331,332] Establishing the relationship between the number of bound cells and corresponding electronic properties will be an essential aspect of FGT adoption to bacteria sensing. Reports suggest the change in properties per bound cell is greater with a lower coverage of surface bound cells.[329] If this holds for FGTs it would lead to attractively low limits of detection when they are applied to cells.

***In situ* Monitoring.** The application of FGTs to cellular detection expands beyond whole cell quantitation. An electronic method that does not incorporate labeling steps (i.e. is label-free) could be used for *in situ* monitoring of extracellular signaling. In this scheme, the microfluidics that deliver the sample to the sensor surface are reconfigured to entrap and immobilize cells near the functionalized electrode.[333] The immobilized cells will then release some signaling molecule (e.g. protein or small molecule) either due to time or due to an altercation in the environmental conditions.[334] The molecules will then diffuse to the active sensor surface leading to a corresponding signal transduction. Monitoring the signal as a function of time enables the experimenter to calculate the rate of release of the signaling molecules or the local concentration of the molecule near the cell surface. This scheme is outlined in Figure 7.5 and would allow for *in situ* monitoring of cellular signaling providing profound insight into cellular dynamics and mechanisms.[335]

7.3 New Directions.

Faradaic Current Transduction. The present transduction by FGTs relies on static changes in potentiometric profiles due to molecular binding. The currents running from the gate electrode to the semiconductor are dominated by the capacitive coupling of

the electrolyte phases $\left(I \sim C\frac{dV}{dt}\right)$. Enhanced amplification could be achieved if a Faradaic current was triggered due to interfacial chemistry altercations. At present, these currents are intentionally mitigated by oversizing electrodes to prevent dielectric breakdown.[4]

The tuning of electrode areas can induce significant interfacial potentials at the floating-gate electrode/aqueous electrolyte interface. This potential can induce redox reactions across the interface provided electrochemically active molecules were incorporated into the sensing medium.[84,86,318] The effective voltage that induces a faradaic current is dependent on the molecular properties and will shift in accordance with analyte binding. The general schema is outlined in Figure 7.6 along with a hypothetical output. The

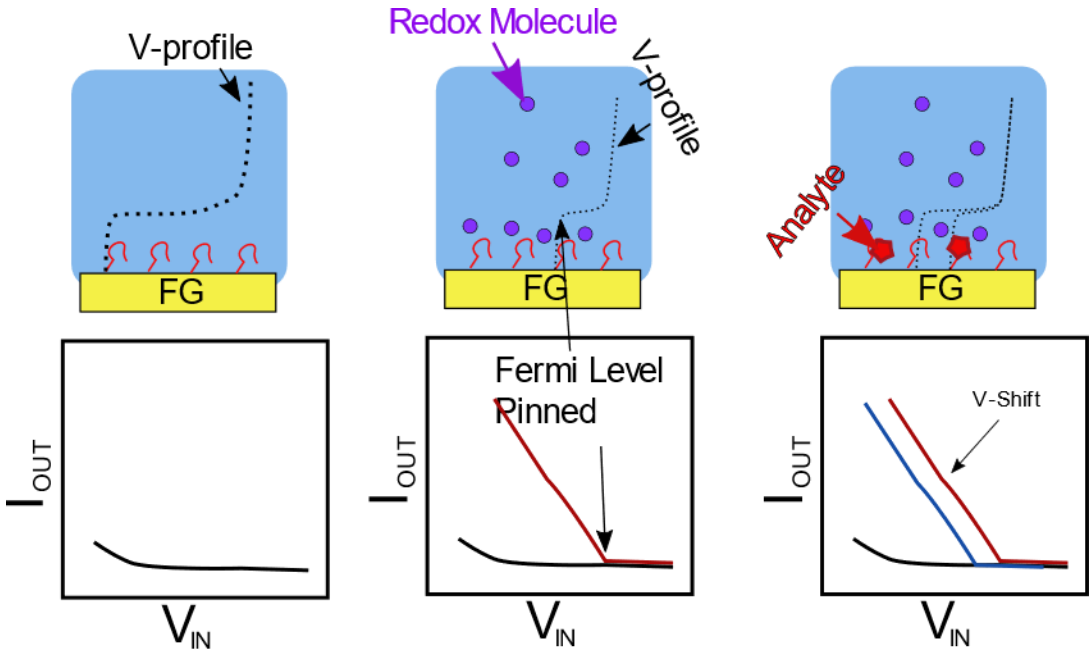

Figure 7.6: Redox FGT.
The left panel shows the response from a conventional FGT that has been resized so there is a significant potential drop across the sensor surface. The middle panel shows how the potential difference between the aqueous bulk and FG can pin the fermi-level or fill interfacial states when a redox active molecule is incorporated. The binding of analyte shifts the applied voltage leading to an amplified response.

faradaic current into the floating gate will manifest as a highly amplified change in potentiometric properties.

Piezoelectric Signaling. To date, FGTs have been applied as chemical detectors for DNA and proteins. Their success is due to the versatility of the transduction mechanism, the rapid signal extraction due to label-free sensing, and the ease-of-operation engendered by microfluidics. However, the mechanical flexibility of organic electronic materials has not been fully utilized in the presented schema. Emerging applications of flexible electronics impact fields of robotics and prosthetics with electronic skin (e-skin).[336] The core technology is a piezoelectric sensor with a mechanical pressure transduced as an electronic output.

The amplification capabilities of the FGT platform can be applied to e-skin or pressure sensing applications by incorporating a piezoelectric material. Materials such as

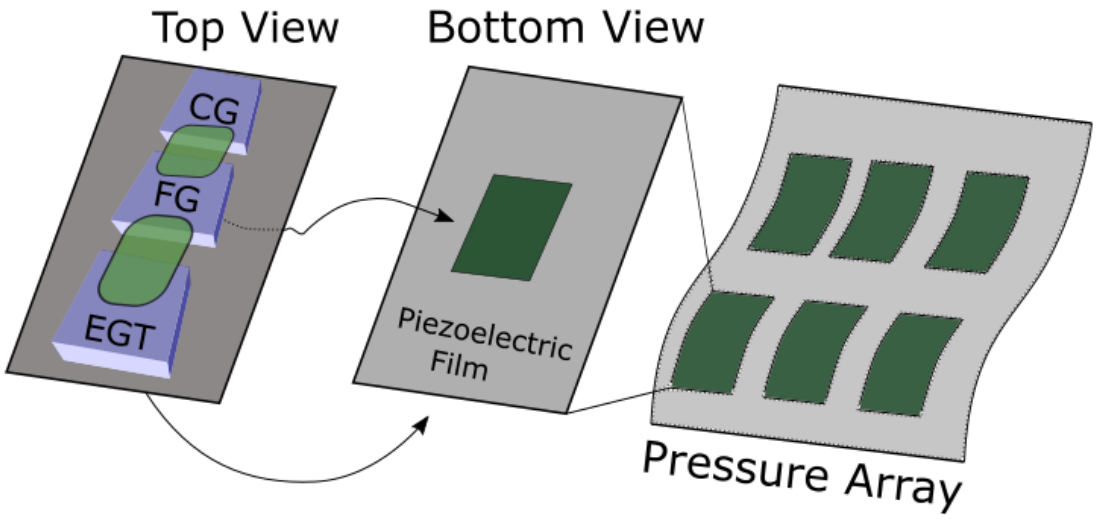

Figure 7.7: Piezoelectric FGT Array.
The proposed layout of a piezoelectric pressure sensor is presented. The FGT are fabricated in the conventional, side-gated architecture (left, Top-View). The underside of the floating-gate is interfaced with a piezoelectric film (middle, bottom-view). These FGTs make up an array on a flexible substrate that can be used in e-skin applications (right).

PVDF have demonstrated clear piezoelectric properties due to the oriented dipoles in a semi-crystalline film.[337] A pressure shifts this dipole orientation and manifests as a change in voltage across the film.[337] A film of piezoelectric material can be incorporated onto the floating-gate leading to induced voltage shifts in the coupled FGT. Figure 7.7 outlines a proposed schematic that exploits the mechanical and geometric flexibility of organic electronics. The piezoelectric film can be fabricated on the "back-side" of an FGT array onto a flexible substrate. The resulting e-skin represents a large-area array of spatially resolved pressure sensors that can be applied in various prosthetic or robotics applications.

8. Bibliography

1. Simon, D. T., Gabrielsson, E. O., Tybrandt, K. & Berggren, M. Organic Bioelectronics: Bridging the Signaling Gap between Biology and Technology. *Chem. Rev.* (2016). doi:10.1021/acs.chemrev.6b00146
2. Sackmann, E. K., Fulton, A. L. & Beebe, D. J. The present and future role of microfluidics in biomedical research. *Nature* **507,** 181–189 (2014).
3. White, S. P., Dorfman, K. D. & Frisbie, C. D. Label-Free DNA Sensing Platform with Low-Voltage Electrolyte-Gated Transistors. *Anal. Chem.* **87,** 1861–1866 (2015).
4. White, S. P., Dorfman, K. D. & Frisbie, C. D. Operating and Sensing Mechanism of Electrolyte-Gated Transistors with Floating Gates: Building a Platform for Amplified Biodetection. *J. Phys. Chem. C* **120,** 108–117 (2016).
5. White, S. P., Sreevatsan, S., Frisbie, C. D. & Dorfman, K. D. Rapid, Selective, Label-Free Aptameric Capture and Detection of Ricin in Potable Liquids Using a Printed Floating Gate Transistor. *ACS Sens.* **1,** 1213–1216 (2016).
6. Wang, S., Ha, M., Manno, M., Frisbie, C. D. & Leighton, C. Hopping transport and the Hall effect near the insulator–metal transition in electrochemically gated poly(3-hexylthiophene) transistors. *Nature Communications* **3,** ncomms2213 (2012).
7. Johnston, I. D. *et al.* Dean flow focusing and separation of small microspheres within a narrow size range. *Microfluid Nanofluid* **17,** 509–518 (2014).
8. Volpatti, L. R. & Yetisen, A. K. Commercialization of microfluidic devices. *Trends Biotechnol.* **32,** 347–350 (2014).
9. Hedley, G. J., Ruseckas, A. & Samuel, I. D. W. Light Harvesting for Organic Photovoltaics. *Chem. Rev.* **117,** 796–837 (2017).
10. Perelaer, J. *et al.* Printed electronics: the challenges involved in printing devices, interconnects, and contacts based on inorganic materials. *J. Mater. Chem.* **20,** 8446–8453 (2010).
11. Dastoor, P. C. Solar paint: Harvesting light. *Nature Photonics* **7,** nphoton.2013.130 (2013).

12. Sharma, S., Zapatero-Rodríguez, J., Estrela, P. & O'Kennedy, R. Point-of-Care Diagnostics in Low Resource Settings: Present Status and Future Role of Microfluidics. *Biosensors (Basel)* **5,** 577–601 (2015).
13. Small but Perfectly Formed? Successes, Challenges, and Opportunities for Microfluidics in the Chemical and Biological Sciences: Chem. Available at: http://www.cell.com/chem/pdf/S2451-9294(17)30033-5.pdf. (Accessed: 13th November 2017)
14. Ping, J., Vishnubhotla, R., Vrudhula, A. & Johnson, A. T. C. Scalable Production of High-Sensitivity, Label-Free DNA Biosensors Based on Back-Gated Graphene Field Effect Transistors. *ACS Nano* **10,** 8700–8704 (2016).
15. Chen, P.-C. *et al.* Editors' Choice—Field-Effect Transistor-Based Biosensors and a Portable Device for Personal Healthcare. *ECS J. Solid State Sci. Technol.* **6,** Q71–Q76 (2017).
16. Sarkar, D. *et al.* MoS2 Field-Effect Transistor for Next-Generation Label-Free Biosensors. *ACS Nano* **8,** 3992–4003 (2014).
17. Kilic, M. S., Bazant, M. Z. & Ajdari, A. Steric effects in the dynamics of electrolytes at large applied voltages. I. Double-layer charging. *Phys Rev E Stat Nonlin Soft Matter Phys* **75,** 021502 (2007).
18. Luka, G. *et al.* Microfluidics Integrated Biosensors: A Leading Technology towards Lab-on-a-Chip and Sensing Applications. *Sensors (Basel)* **15,** 30011–30031 (2015).
19. Kumar, A., Kim, H. & Hancke, G. P. Environmental Monitoring Systems: A Review. *IEEE Sensors Journal* **13,** 1329–1339 (2013).
20. Rodriguez-Mozaz, S., Alda, M. J. L. de, Marco, M.-P. & Barceló, D. Biosensors for environmental monitoring: A global perspective. *Talanta* **65,** 291–297 (2005).
21. Alocilja, E. C. & Radke, S. M. Market analysis of biosensors for food safety. *Biosens Bioelectron* **18,** 841–846 (2003).
22. Yasmin, J., Ahmed, M. R. & Cho, B.-K. Biosensors and their Applications in Food Safety: A Review. *J. of Biosystems Eng.* **41,** 240–254 (2016).
23. Patel, S., Nanda, R., Sahoo, S. & Mohapatra, E. Biosensors in Health Care: The Milestones Achieved in Their Development towards Lab-on-Chip-Analysis. *Biochem Res Int* **2016,** (2016).

24. Darbeau, R. W. Nuclear Magnetic Resonance (NMR) Spectroscopy: A Review and a Look at Its Use as a Probative Tool in Deamination Chemistry. *Applied Spectroscopy Reviews* **41,** 401–425 (2006).
25. Peterson, E. M., Manhart, M. W. & Harris, J. M. Competitive Assays of Label-Free DNA Hybridization with Single-Molecule Fluorescence Imaging Detection. *Anal. Chem.* **88,** 6410–6417 (2016).
26. Bai, X., McMullan, G. & Scheres, S. H. W. How cryo-EM is revolutionizing structural biology. *Trends in Biochemical Sciences* **40,** 49–57 (2015).
27. Vojinović, V., Cabral, J. M. S. & Fonseca, L. P. Real-time bioprocess monitoring: Part I: In situ sensors. *Sensors and Actuators B: Chemical* **114,** 1083–1091 (2006).
28. Wang, J. From DNA biosensors to gene chips. *Nucleic Acids Res* **28,** 3011–3016 (2000).
29. Vestergaard, M., Kerman, K. & Tamiya, E. An Overview of Label-free Electrochemical Protein Sensors. *Sensors* **7,** 3442–3458 (2007).
30. Vigneshvar, S., Sudhakumari, C. C., Senthilkumaran, B. & Prakash, H. Recent Advances in Biosensor Technology for Potential Applications – An Overview. *Front Bioeng Biotechnol* **4,** (2016).
31. Pfeiffer, F. & Mayer, G. Selection and Biosensor Application of Aptamers for Small Molecules. *Front Chem* **4,** (2016).
32. Raj, A. *et al.* Comparative Evaluation of Several Gene Targets for Designing a Multiplex-PCR for an Early Diagnosis of Extrapulmonary Tuberculosis. *Yonsei Med J* **57,** 88–96 (2016).
33. Yamamoto, Y. PCR in Diagnosis of Infection: Detection of Bacteria in Cerebrospinal Fluids. *Clin Diagn Lab Immunol* **9,** 508–514 (2002).
34. Heather, J. M. & Chain, B. The sequence of sequencers: The history of sequencing DNA. *Genomics* **107,** 1–8 (2016).
35. Shendure, J. & Ji, H. Next-generation DNA sequencing. *Nature Biotechnology* **26,** nbt1486 (2008).
36. Feng, Y., Zhang, Y., Ying, C., Wang, D. & Du, C. Nanopore-based Fourth-generation DNA Sequencing Technology. *Genomics, Proteomics & Bioinformatics* **13,** 4–16 (2015).

37. Gresham, D., Dunham, M. J. & Botstein, D. Comparing whole genomes using DNA microarrays. *Nature Reviews Genetics* **9,** nrg2335 (2008).
38. Maruyama, K., Yamaguchi-Shinozaki, K. & Shinozaki, K. Gene expression profiling using DNA microarrays. *Methods Mol. Biol.* **1062,** 381–391 (2014).
39. Lee, P. Y., Costumbrado, J., Hsu, C.-Y. & Kim, Y. H. Agarose Gel Electrophoresis for the Separation of DNA Fragments. *J Vis Exp* (2012). doi:10.3791/3923
40. Dorfman, K. D., King, S. B., Olson, D. W., Thomas, J. D. P. & Tree, D. R. Beyond Gel Electrophoresis: Microfluidic Separations, Fluorescence Burst Analysis, and DNA Stretching. *Chem. Rev.* **113,** 2584–2667 (2013).
41. Wellhausen, R. & Seitz, H. Facing Current Quantification Challenges in Protein Microarrays. *BioMed Research International* (2012). doi:10.1155/2012/831347
42. Steen, H. & Mann, M. The abc's (and xyz's) of peptide sequencing. *Nature Reviews Molecular Cell Biology* **5,** nrm1468 (2004).
43. Law, K. P. & Lim, Y. P. Recent advances in mass spectrometry: data independent analysis and hyper reaction monitoring. *Expert Rev Proteomics* **10,** 551–566 (2013).
44. Gundry, R. L. *et al.* Preparation of Proteins and Peptides for Mass Spectrometry Analysis in a Bottom-Up Proteomics Workflow. *Curr Protoc Mol Biol* **CHAPTER,** Unit10.25 (2009).
45. Bantscheff, M., Schirle, M., Sweetman, G., Rick, J. & Kuster, B. Quantitative mass spectrometry in proteomics: a critical review. *Anal Bioanal Chem* **389,** 1017–1031 (2007).
46. Chappell, D. L. *et al.* Quantitation of human peptides and proteins via MS: review of analytically validated assays. *Bioanalysis* **6,** 1843–1857 (2014).
47. Fricker, L. D. Limitations of Mass Spectrometry-Based Peptidomic Approaches. *J. Am. Soc. Mass Spectrom.* **26,** 1981–1991 (2015).
48. Bruins Slot, I. D., Bremer, M. G. E. G., van der Fels-Klerx, I. & Hamer, R. J. Evaluating the Performance of Gluten ELISA Test Kits: The Numbers Do Not Tell the Tale. *Cereal Chemistry Journal* **92,** 513–521 (2015).
49. Massai, L. *et al.* Development of an ELISA assay for the quantification of soluble huntingtin in human blood cells. *BMC Biochem* **14,** 34 (2013).

50. Karanikola, S. N. *et al.* Development of a multiplex fluorescence immunological assay for the simultaneous detection of antibodies against Cooperia oncophora, Dictyocaulus viviparus and Fasciola hepatica in cattle. *Parasit Vectors* **8,** (2015).
51. Zhu, L. *et al.* Development of a double-antibody sandwich ELISA for rapid detection of *Bacillus Cereus* in food. *Scientific Reports* **6,** srep16092 (2016).
52. Afshar, A. *et al.* Comparison of competitive and indirect enzyme-linked immunosorbent assays for detection of bluetongue virus antibodies in serum and whole blood. *J. Clin. Microbiol.* **25,** 1705–1710 (1987).
53. Hochegger, R., Mayer, W. & Prochaska, M. Comparison of R5 and G12 Antibody-Based ELISA Used for the Determination of the Gluten Content in Official Food Samples. *Foods* **4,** 654–664 (2015).
54. Cifuentes, A. Food Analysis: Present, Future, and Foodomics. *International Scholarly Research Notices* (2012). doi:10.5402/2012/801607
55. Borrebaeck, C. A. K. Antibodies in diagnostics – from immunoassays to protein chips. *Immunology Today* **21,** 379–382 (2000).
56. Hsieh, H. V., Dantzler, J. L. & Weigl, B. H. Analytical Tools to Improve Optimization Procedures for Lateral Flow Assays. *Diagnostics* **7,** 29 (2017).
57. Posthuma-Trumpie, G. A., Korf, J. & Amerongen, A. van. Lateral flow (immuno)assay: its strengths, weaknesses, opportunities and threats. A literature survey. *Anal Bioanal Chem* **393,** 569–582 (2009).
58. Emerson, D., Agulto, L., Liu, H. & Liu, L. Identifying and Characterizing Bacteria in an Era of Genomics and Proteomics. *BioScience* **58,** 925–936 (2008).
59. Love, B. C. & Rostagno, M. H. Comparison of Five Culture Methods for Salmonella Isolation from Swine Fecal Samples of Known Infection Status. *J VET Diagn Invest* **20,** 620–624 (2008).
60. Curtis, G. D. & Lee, W. H. Culture media and methods for the isolation of Listeria monocytogenes. *Int. J. Food Microbiol.* **26,** 1–13 (1995).
61. Molina, F. *et al.* Improved detection of Escherichia coli and coliform bacteria by multiplex PCR. *BMC Biotechnology* **15,** 48 (2015).
62. Nelis, H. & Poucke, S. V. Enzymatic Detection of Coliforms and Escherichia coli within 4 Hours. *Water, Air, & Soil Pollution* **123,** 43–52 (2000).

63. Omidbakhsh, N., Ahmadpour, F. & Kenny, N. How Reliable Are ATP Bioluminescence Meters in Assessing Decontamination of Environmental Surfaces in Healthcare Settings? *PLoS One* **9,** (2014).
64. Zuo, X. *et al.* A Target-Responsive Electrochemical Aptamer Switch (TREAS) for Reagentless Detection of Nanomolar ATP. *J. Am. Chem. Soc.* **129,** 1042–1043 (2007).
65. Yang, Y. *et al.* Advances in nanopore sequencing technology. *J Nanosci Nanotechnol* **13,** 4521–4538 (2013).
66. Dorfman, K. D. The fluid mechanics of genome mapping. *AIChE J.* **59,** 346–354 (2013).
67. Lebonah, D. E. *et al.* DNA Barcoding on Bacteria: A Review. *Advances in Biology* (2014). doi:10.1155/2014/541787
68. Lubin, A., Sheng, S., Cabooter, D., Augustijns, P. & Cuyckens, F. Flexible nano- and microliter injections on a single liquid chromatography–mass spectrometry system: Minimizing sample preparation and maximizing linear dynamic range. *Journal of Chromatography A* **1524,** 101–107 (2017).
69. Hsu, C.-K. *et al.* Paper-Based ELISA for the Detection of Autoimmune Antibodies in Body Fluid—The Case of Bullous Pemphigoid. *Anal. Chem.* **86,** 4605–4610 (2014).
70. Yetisen, A. K., Akram, M. S. & Lowe, C. R. Paper-based microfluidic point-of-care diagnostic devices. *Lab Chip* **13,** 2210–2251 (2013).
71. Jarvis, N. A., O'Bryan, C. A., Ricke, S. C., Johnson, M. G. & Crandall, P. G. A review of minimal and defined media for growth of Listeria monocytogenes. *Food Control* **66,** 256–269 (2016).
72. Daquigan, N., Grim, C. J., White, J. R., Hanes, D. E. & Jarvis, K. G. Early Recovery of Salmonella from Food Using a 6-Hour Non-selective Pre-enrichment and Reformulation of Tetrathionate Broth. *Front Microbiol* **7,** (2016).
73. Kim, E., Baaske, M. D. & Vollmer, F. Towards next-generation label-free biosensors: recent advances in whispering gallery mode sensors. *Lab Chip* **17,** 1190–1205 (2017).

74. Shrivastava, S., Jadon, N. & Jain, R. Next-generation polymer nanocomposite-based electrochemical sensors and biosensors: A review. *TrAC Trends in Analytical Chemistry* **82,** 55–67 (2016).
75. Rodbard, D. Continuous Glucose Monitoring: A Review of Successes, Challenges, and Opportunities. *Diabetes Technol Ther* **18,** S2-3-S2-13 (2016).
76. Abdulbari, H. A. & Basheer, E. A. M. Electrochemical Biosensors: Electrode Development, Materials, Design, and Fabrication. *CBEN* **4,** 92–105 (2017).
77. Zhou, J. & Rossi, J. Aptamers as targeted therapeutics: current potential and challenges. *Nature Reviews Drug Discovery* **16,** nrd.2016.199 (2016).
78. Zhu, G. *et al.* Combinatorial Screening of DNA Aptamers for Molecular Imaging of HER2 in Cancer. *Bioconjug. Chem.* **28,** 1068–1075 (2017).
79. Baker, M. Reproducibility crisis: Blame it on the antibodies. *Nature* **521,** 274–276 (2015).
80. Darmostuk, M., Rimpelova, S., Gbelcova, H. & Ruml, T. Current approaches in SELEX: An update to aptamer selection technology. *Biotechnol. Adv.* **33,** 1141–1161 (2015).
81. Rotem, D., Jayasinghe, L., Salichou, M. & Bayley, H. Protein detection by nanopores equipped with aptamers. *J. Am. Chem. Soc.* **134,** 2781–2787 (2012).
82. Cho, E. J., Collett, J. R., Szafranska, A. E. & Ellington, A. D. Optimization of aptamer microarray technology for multiple protein targets. *Anal. Chim. Acta* **564,** 82–90 (2006).
83. Daniel, J., Fetter, L., Jett, S., Rowland, T. J. & Bonham, A. J. Electrochemical Aptamer Scaffold Biosensors for Detection of Botulism and Ricin Proteins. *Methods Mol. Biol.* **1600,** 9–23 (2017).
84. Hsieh, K., Ferguson, B. S., Eisenstein, M., Plaxco, K. W. & Soh, H. T. Integrated Electrochemical Microsystems for Genetic Detection of Pathogens at the Point of Care. *Acc. Chem. Res.* **48,** 911–920 (2015).
85. Patterson, A. S., Hsieh, K., Soh, H. T. & Plaxco, K. W. Electrochemical real-time nucleic acid amplification: towards point-of-care quantification of pathogens. *Trends in Biotechnology* **31,** 704–712 (2013).

86. Zhang, S. *et al.* Development of an electrochemical aptamer-based sensor with a sensitive Fe3O4 nanopaticle-redox tag for reagentless protein detection. *Electrochemistry Communications* **13,** 928–931 (2011).
87. Amaya-González, S. *et al.* Affinity of aptamers binding 33-mer gliadin peptide and gluten proteins: Influence of immobilization and labeling tags. *Analytica Chimica Acta* **873,** 63–70 (2015).
88. Strakosas, X., Bongo, M. & Owens, R. M. The organic electrochemical transistor for biological applications. *J. Appl. Polym. Sci.* **132,** (2015).
89. Kim, S. H. *et al.* Electrolyte-gated transistors for organic and printed electronics. *Adv. Mater. Weinheim* **25,** 1822–1846 (2013).
90. Janata, J. Thirty Years of CHEMFETs – A Personal View. *Electroanalysis* **16,** 1831–1835 (2004).
91. Uzzal, M. M., Zarkesh-Ha, P., Edwards, J. S., Coelho, E. & Rawat, P. A highly sensitive ISFET using pH-to-current conversion for real-time DNA sequencing. in *2014 27th IEEE International System-on-Chip Conference (SOCC)* 410–414 (2014). doi:10.1109/SOCC.2014.6948964
92. Zarkesh-Ha, P., Edwards, J. & Szauter, P. Avalanche ISFET: A highly sensitive pH sensor for genome sequencing. in *2015 IEEE Biomedical Circuits and Systems Conference (BioCAS)* 1–4 (2015). doi:10.1109/BioCAS.2015.7348335
93. Wang, D., Noël, V. & Piro, B. Electrolytic Gated Organic Field-Effect Transistors for Application in Biosensors—A Review. *Electronics* **5,** 9 (2016).
94. Sin, M. L., Mach, K. E., Wong, P. K. & Liao, J. C. Advances and challenges in biosensor-based diagnosis of infectious diseases. *Expert Rev Mol Diagn* **14,** 225–244 (2014).
95. Berggren, M. & Richter-Dahlfors, A. Organic Bioelectronics. *Adv. Mater.* **19,** 3201–3213 (2007).
96. Newman, C. R. *et al.* Introduction to Organic Thin Film Transistors and Design of n-Channel Organic Semiconductors. *Chem. Mater.* **16,** 4436–4451 (2004).
97. Fang, Y., Li, X. & Fang, Y. Organic bioelectronics for neural interfaces. *J. Mater. Chem. C* **3,** 6424–6430 (2015).

98. Khodagholy, D. *et al. In vivo* recordings of brain activity using organic transistors. *Nature Communications* **4,** ncomms2573 (2013).
99. Aregueta-Robles, U. A., Woolley, A. J., Poole-Warren, L. A., Lovell, N. H. & Green, R. A. Organic electrode coatings for next-generation neural interfaces. *Front Neuroeng* **7,** (2014).
100. Chortos, A., Liu, J. & Bao, Z. Pursuing prosthetic electronic skin. *Nature Materials* **15,** nmat4671 (2016).
101. Wang, X. *et al.* Recent Progress in Electronic Skin. *Adv. Sci.* **2,** (2015).
102. Demelas, M. *et al.* Charge sensing by organic charge-modulated field effect transistors: application to the detection of bio-related effects. *J. Mater. Chem. B* **1,** 3811–3819 (2013).
103. Cramer, T. *et al.* Water-gated organic field effect transistors – opportunities for biochemical sensing and extracellular signal transduction. *J. Mater. Chem. B* **1,** 3728–3741 (2013).
104. Kergoat, L. *et al.* Tuning the threshold voltage in electrolyte-gated organic field-effect transistors. *Proc. Natl. Acad. Sci. U.S.A.* **109,** 8394–8399 (2012).
105. de Boer, B., Hadipour, A., Mandoc, M. M., van Woudenbergh, T. & Blom, P. W. M. Tuning of Metal Work Functions with Self-Assembled Monolayers. *Adv. Mater.* **17,** 621–625 (2005).
106. Justino, C. I. L., Gomes, A. R., Freitas, A. C., Duarte, A. C. & Rocha-Santos, T. A. P. Graphene based sensors and biosensors. *TrAC Trends in Analytical Chemistry* **91,** 53–66 (2017).
107. Kergoat, L., Piro, B., Berggren, M., Horowitz, G. & Pham, M.-C. Advances in organic transistor-based biosensors: from organic electrochemical transistors to electrolyte-gated organic field-effect transistors. *Anal Bioanal Chem* **402,** 1813–1826 (2012).
108. Guo, X., Gorodetsky, A. A., Hone, J., Barton, J. K. & Nuckolls, C. Conductivity of a single DNA duplex bridging a carbon nanotube gap. *Nat Nano* **3,** 163–167 (2008).
109. Li, J. *et al.* Carbon Nanotube Sensors for Gas and Organic Vapor Detection. *Nano Lett.* **3,** 929–933 (2003).

110. Tang, X. *et al.* Carbon Nanotube DNA Sensor and Sensing Mechanism. *Nano Lett.* **6,** 1632–1636 (2006).
111. Cho, J. H. *et al.* Printable ion-gel gate dielectrics for low-voltage polymer thin-film transistors on plastic. *Nat Mater* **7,** 900–906 (2008).
112. Choi, J.-H. *et al.* High Capacitance, Photo-Patternable Ion Gel Gate Insulators Compatible with Vapor Deposition of Metal Gate Electrodes. *ACS Appl. Mater. Interfaces* **6,** 19275–19281 (2014).
113. Khodagholy, D. *et al.* Organic electrochemical transistor incorporating an ionogel as a solid state electrolyte for lactate sensing. *J. Mater. Chem.* **22,** 4440–4443 (2012).
114. Bannock, J. H. *et al.* The influence of polymer purification on the efficiency of poly(3-hexylthiophene):fullerene organic solar cells. *Scientific Reports* **6,** srep23651 (2016).
115. Kim, S. H., Hong, K., Lee, K. H. & Frisbie, C. D. Performance and Stability of Aerosol-Jet-Printed Electrolyte-Gated Transistors Based on Poly(3-hexylthiophene). *ACS Appl. Mater. Interfaces* **5,** 6580–6585 (2013).
116. Marrocchi, A., Lanari, D., Facchetti, A. & Vaccaro, L. Poly(3-hexylthiophene): synthetic methodologies and properties in bulk heterojunction solar cells. *Energy Environ. Sci.* **5,** 8457–8474 (2012).
117. Braga, D., Ha, M., Xie, W. & Frisbie, C. D. Ultralow contact resistance in electrolyte-gated organic thin film transistors. *Appl. Phys. Lett.* **97,** 193311 (2010).
118. Xie, W., Wang, S., Zhang, X., Leighton, C. & Frisbie, C. D. High Conductance 2D Transport around the Hall Mobility Peak in Electrolyte-Gated Rubrene Crystals. *Phys. Rev. Lett.* **113,** 246602 (2014).
119. Fukuda, K. *et al.* Printed Organic Transistors with Uniform Electrical Performance and Their Application to Amplifiers in Biosensors. *Adv. Electron. Mater.* **1,** (2015).
120. Kergoat, L. *et al.* A Water-Gate Organic Field-Effect Transistor. *Adv. Mater.* **22,** 2565–2569 (2010).
121. Hlaing, H. *et al.* Low-Voltage Organic Electronics Based on a Gate-Tunable Injection Barrier in Vertical graphene-organic Semiconductor Heterostructures. *Nano Lett.* **15,** 69–74 (2015).

122. Minot, E. D. *et al.* Carbon nanotube biosensors: The critical role of the reference electrode. *Appl. Phys. Lett.* **91,** 093507 (2007).
123. Khan, S., Lorenzelli, L. & Dahiya, R. S. Technologies for Printing Sensors and Electronics Over Large Flexible Substrates: A Review. *IEEE Sensors Journal* **15,** 3164–3185 (2015).
124. Chang, J. S., Facchetti, A. F. & Reuss, R. A Circuits and Systems Perspective of Organic/Printed Electronics: Review, Challenges, and Contemporary and Emerging Design Approaches. *IEEE Journal on Emerging and Selected Topics in Circuits and Systems* **7,** 7–26 (2017).
125. Kim, S. H. *et al.* Electrolyte-Gated Transistors for Organic and Printed Electronics. *Adv. Mater.* **25,** 1822–1846 (2013).
126. Søndergaard, R. R., Hösel, M. & Krebs, F. C. Roll-to-Roll fabrication of large area functional organic materials. *J. Polym. Sci. B Polym. Phys.* **51,** 16–34 (2013).
127. Yin, Z., Huang, Y., Bu, N., Wang, X. & Xiong, Y. Inkjet printing for flexible electronics: Materials, processes and equipments. *Chin. Sci. Bull.* **55,** 3383–3407 (2010).
128. Grau, G. *et al.* Gravure-printed electronics: recent progress in tooling development, understanding of printing physics, and realization of printed devices. *Flex. Print. Electron.* **1,** 023002 (2016).
129. Mahajan, A., Frisbie, C. D. & Francis, L. F. Optimization of Aerosol Jet Printing for High-Resolution, High-Aspect Ratio Silver Lines. *ACS Appl. Mater. Interfaces* **5,** 4856–4864 (2013).
130. Dong, J., Liu, J., Kang, G., Xie, J. & Wang, Y. Pushing the resolution of photolithography down to 15nm by surface plasmon interference. *Scientific Reports* **4,** srep05618 (2014).
131. Hu, W. *et al.* Fabrication of Planar, Layered Nanoparticles Using Tri-layer Resist Templates. *Nanotechnology* **22,** 185302 (2011).
132. Sollier, E., Murray, C., Maoddi, P. & Di Carlo, D. Rapid prototyping polymers for microfluidic devices and high pressure injections. *Lab Chip* **11,** 3752–3765 (2011).

133. Thompson, B. L. *et al.* Inexpensive, rapid prototyping of microfluidic devices using overhead transparencies and a laser print, cut and laminate fabrication method. *Nature Protocols* **10,** nprot.2015.051 (2015).
134. Blank, S. Why the Lean Start-Up Changes Everything. *Harvard Business Review* (2013). Available at: https://hbr.org/2013/05/why-the-lean-start-up-changes-everything. (Accessed: 15th November 2017)
135. Grimme, J., King, T., Dong Jo, K., Cropek, D. & Timperman, A. T. Development of Fieldable Lab-on-a-Chip Systems for Detection of a Broad Array of Targets From Toxicants to Biowarfare Agents. *J. Nanotechnol. Eng. Med.* **4,** 020904–020904 (2013).
136. Patterson, A. S., Hsieh, K., Soh, H. T. & Plaxco, K. W. Electrochemical real-time nucleic acid amplification: towards point-of-care quantification of pathogens. *Trends in Biotechnology* **31,** 704–712 (2013).
137. Chan, C. P. Y. *et al.* Evidence-Based Point-of-Care Diagnostics: Current Status and Emerging Technologies. *Annual Review of Analytical Chemistry* **6,** 191–211 (2013).
138. Kergoat, L., Piro, B., Berggren, M., Horowitz, G. & Pham, M.-C. Advances in organic transistor-based biosensors: from organic electrochemical transistors to electrolyte-gated organic field-effect transistors. *Anal Bioanal Chem* **402,** 1813–1826 (2012).
139. Lin, P. & Yan, F. Organic Thin-Film Transistors for Chemical and Biological Sensing. *Adv. Mater.* **24,** 34–51 (2012).
140. Berggren, M. & Richter-Dahlfors, A. Organic Bioelectronics. *Adv. Mater.* **19,** 3201–3213 (2007).
141. Zheng, X.-J., Qiu, J.-D., Zhang, L., Wang, Z.-X. & Liang, R.-P. Label-free colorimetric assay for DNA methylation based on unmodified Au nanorods as a signal sensing probe coupled with enzyme-linkage reactions. *Chem. Commun.* **49,** 3546–3548 (2013).
142. Kim, S. H. *et al.* Electrolyte-Gated Transistors for Organic and Printed Electronics. *Adv. Mater.* **25,** 1822–1846 (2013).

143. Buth, F., Kumar, D., Stutzmann, M. & Garrido, J. A. Electrolyte-gated organic field-effect transistors for sensing applications. *Applied Physics Letters* **98,** 153302 (2011).
144. Kim, S. H., Hong, K., Lee, K. H. & Frisbie, C. D. Performance and Stability of Aerosol-Jet-Printed Electrolyte-Gated Transistors Based on Poly(3-hexylthiophene). *ACS Appl. Mater. Interfaces* **5,** 6580–6585 (2013).
145. Bernards, D. A. *et al.* Enzymatic sensing with organic electrochemical transistors. *J. Mater. Chem.* **18,** 116–120 (2008).
146. Khodagholy, D. *et al.* Organic electrochemical transistor incorporating an ionogel as a solid state electrolyte for lactate sensing. *J. Mater. Chem.* **22,** 4440–4443 (2012).
147. Mabeck, J. & Malliaras, G. Chemical and biological sensors based on organic thin-film transistors. *Anal Bioanal Chem* **384,** 343–353 (2006).
148. Lee, K. H., Zhang, S., Lodge, T. P. & Frisbie, C. D. Electrical Impedance of Spin-Coatable Ion Gel Films. *J. Phys. Chem. B* **115,** 3315–3321 (2011).
149. Lin, P., Luo, X., Hsing, I.-M. & Yan, F. Organic Electrochemical Transistors Integrated in Flexible Microfluidic Systems and Used for Label-Free DNA Sensing. *Advanced Materials* **23,** 4035–4040 (2011).
150. Tang, X. *et al.* Carbon Nanotube DNA Sensor and Sensing Mechanism. *Nano Lett.* **6,** 1632–1636 (2006).
151. Kergoat, L. *et al.* A Water-Gate Organic Field-Effect Transistor. *Adv. Mater.* **22,** 2565–2569 (2010).
152. Kim, D.-S. *et al.* An FET-type charge sensor for highly sensitive detection of DNA sequence. *Biosens Bioelectron* **20,** 69–74 (2004).
153. Lai, S. *et al.* Ultralow Voltage, OTFT-Based Sensor for Label-Free DNA Detection. *Advanced Materials* **25,** 103–107 (2013).
154. Khodagholy, D. *et al.* High transconductance organic electrochemical transistors. *Nat Commun* **4,** (2013).
155. Gaikwad, A. M., Steingart, D. A., Ng, T. N., Schwartz, D. E. & Whiting, G. L. A flexible high potential printed battery for powering printed electronics. *Applied Physics Letters* **102,** 233302 (2013).

156. Zhang, S., Lee, K. H., Sun, J., Frisbie, C. D. & Lodge, T. P. Viscoelastic Properties, Ionic Conductivity, and Materials Design Considerations for Poly(styrene-b-ethylene oxide-b-styrene)-Based Ion Gel Electrolytes. *Macromolecules* **44,** 8981–8989 (2011).
157. Peterson, A. W., Heaton, R. J. & Georgiadis, R. M. The effect of surface probe density on DNA hybridization. *Nucl. Acids Res.* **29,** 5163–5168 (2001).
158. Herne, T. M. & Tarlov, M. J. Characterization of DNA Probes Immobilized on Gold Surfaces. *J. Am. Chem. Soc.* **119,** 8916–8920 (1997).
159. Steel, A. B., Levicky, R. L., Herne, T. M. & Tarlov, M. J. Immobilization of nucleic acids at solid surfaces: effect of oligonucleotide length on layer assembly. *Biophys J* **79,** 975–981 (2000).
160. Hirons, G. T., Fawcett, J. J. & Crissman, H. A. TOTO and YOYO: New very bright fluorochromes for DNA content analyses by flow cytometry. *Cytometry* **15,** 129–140 (1994).
161. Gong, P. & Levicky, R. DNA surface hybridization regimes. *PNAS* **105,** 5301–5306 (2008).
162. Wong, I. Y. & Melosh, N. A. An electrostatic model for DNA surface hybridization. *Biophys. J.* **98,** 2954–2963 (2010).
163. Ethan D. Minot, A. M. J. Carbon nanotube biosensors: The critical role of the reference electrode. *Applied Physics Letters* 093507-093507-3 (2007). doi:10.1063/1.2775090
164. Tao, C., Chen, B., William, S. & Pandey, S. A novel floating-gate biosensing device with controlled charge-modulation. in *Life Science Systems and Applications Workshop, 2007. LISA 2007. IEEE/NIH* 257–260 (2007). doi:10.1109/LSSA.2007.4400933
165. Chou, C.-F. *et al.* Electrodeless dielectrophoresis of single- and double-stranded DNA. *Biophys J* **83,** 2170–2179 (2002).
166. Thompson, M. *et al.* Label-free detection of nucleic acid and protein microarrays by scanning Kelvin nanoprobe. *Biosens Bioelectron* **20,** 1471–1481 (2005).
167. Cai, L., Tabata, H. & Kawai, T. Self-assembled DNA networks and their electrical conductivity. *Applied Physics Letters* **77,** 3105–3106 (2000).

168. Chen, B., Parashar, A. & Pandey, S. Folded Floating-Gate CMOS Biosensor for the Detection of Charged Biochemical Molecules. *IEEE Sensors Journal* **11,** 2906–2910 (2011).
169. Li, C.-Z., Liu, Y. & Luong, J. H. T. Impedance Sensing of DNA Binding Drugs Using Gold Substrates Modified with Gold Nanoparticles. *Anal. Chem.* **77,** 478–485 (2005).
170. Rivera-Gandía, J. *et al.* Electrochemical Capacitance DNA Sensing at Hairpin-Modified Au Electrodes. *Journal of Sensors* **2011,** e735279 (2011).
171. Carrara, S. *et al.* Capacitance DNA bio-chips improved by new probe immobilization strategies. *Microelectronics Journal* **41,** 711–717 (2010).
172. Kim, B., Choi, S. H., Zhu, X.-Y. & Frisbie, C. D. Molecular Tunnel Junctions Based on π-Conjugated Oligoacene Thiols and Dithiols between Ag, Au, and Pt Contacts: Effect of Surface Linking Group and Metal Work Function. *J. Am. Chem. Soc.* **133,** 19864–19877 (2011).
173. Steel, A. B., Herne, T. M. & Tarlov, M. J. Electrochemical Quantitation of DNA Immobilized on Gold. **70,** 4670–4677 (1998).
174. Drummond, T. G., Hill, M. G. & Barton, J. K. Electrochemical DNA sensors. *Nat Biotech* **21,** 1192–1199 (2003).
175. Hölzel, R. Dielectric and dielectrophoretic properties of DNA. *IET Nanobiotechnol* **3,** 28–45 (2009).
176. Guo, X., Gorodetsky, A. A., Hone, J., Barton, J. K. & Nuckolls, C. Conductivity of a single DNA duplex bridging a carbon nanotube gap. *Nat Nanotechnol* **3,** 163–167 (2008).
177. Peterson, A. W., Wolf, L. K. & Georgiadis, R. M. Hybridization of mismatched or partially matched DNA at surfaces. *J. Am. Chem. Soc.* **124,** 14601–14607 (2002).
178. Sinensky, A. K. & Belcher, A. M. Label-free and high-resolution protein/DNA nanoarray analysis using Kelvin probe force microscopy. *Nat Nano* **2,** 653–659 (2007).
179. Sassolas, A., Leca-Bouvier, B. D. & Blum, L. J. DNA biosensors and microarrays. *Chem. Rev.* **108,** 109–139 (2008).

180. Friend, J. & Yeo, L. Fabrication of microfluidic devices using polydimethylsiloxane. *Biomicrofluidics* **4,** (2010).
181. Sackmann, E. K., Fulton, A. L. & Beebe, D. J. The present and future role of microfluidics in biomedical research. *Nature* **507,** 181–189 (2014).
182. Squires, T. M., Messinger, R. J. & Manalis, S. R. Making it stick: convection, reaction and diffusion in surface-based biosensors. *Nat Biotech* **26,** 417–426 (2008).
183. Lu, G. *et al.* Moderate doping leads to high performance of semiconductor/insulator polymer blend transistors. *Nat Commun* **4,** 1588 (2013).
184. White, H. S., Kittlesen, G. P. & Wrighton, M. S. Chemical derivatization of an array of three gold microelectrodes with polypyrrole: fabrication of a molecule-based transistor. *J. Am. Chem. Soc.* **106,** 5375–5377 (1984).
185. Thackeray, J. W., White, H. S. & Wrighton, M. S. Poly(3-methylthiophene)-coated electrodes: optical and electrical properties as a function of redox potential and amplification of electrical and chemical signals using poly(3-methylthiophene)-based microelectrochemical transistors. *J. Phys. Chem.* **89,** 5133–5140 (1985).
186. Natan, M. J., Mallouk, T. E. & Wrighton, M. S. The pH-sensitive tungsten(VI) oxide-based microelectrochemical transistors. *J. Phys. Chem.* **91,** 648–654 (1987).
187. Kim, S. H. *et al.* Electrolyte-Gated Transistors for Organic and Printed Electronics. *Adv. Mater.* **25,** 1822–1846 (2013).
188. Du, H., Lin, X., Xu, Z. & Chu, D. Electric double-layer transistors: a review of recent progress. *J Mater Sci* 1–33 (2015). doi:10.1007/s10853-015-9121-y
189. Khodagholy, D. *et al.* High transconductance organic electrochemical transistors. *Nat Commun* **4,** (2013).
190. Rivnay, J. *et al.* High-performance transistors for bioelectronics through tuning of channel thickness. *Science Advances* **1,** e1400251–e1400251 (2015).
191. Tang, X. *et al.* Carbon Nanotube DNA Sensor and Sensing Mechanism. *Nano Lett.* **6,** 1632–1636 (2006).
192. Caras, S. & Janata, J. Field effect transistor sensitive to penicillin. *Anal. Chem.* **52,** 1935–1937 (1980).

193. Kalantari, R. *et al.* Label-Free Voltammetric Detection Using Individually Addressable Oligonucleotide Microelectrode Arrays. *Anal. Chem.* **82,** 9028–9033 (2010).
194. Janata, J. & Josowicz, M. Organic semiconductors in potentiometric gas sensors. *J Solid State Electrochem* **13,** 41–49 (2008).
195. Janata, J. *Principles of Chemical Sensors*. (Springer Science & Business Media, 2010).
196. Manoli, K. *et al.* Printable Bioelectronics To Investigate Functional Biological Interfaces. *Angew. Chem. Int. Ed. Engl.* **54,** 12562–12576 (2015).
197. Cramer, T. *et al.* Water-gated organic field effect transistors – opportunities for biochemical sensing and extracellular signal transduction. *J. Mater. Chem. B* **1,** 3728–3741 (2013).
198. Demelas, M. *et al.* Charge sensing by organic charge-modulated field effect transistors: application to the detection of bio-related effects. *J. Mater. Chem. B* **1,** 3811–3819 (2013).
199. Spanu, A. *et al.* An organic transistor-based system for reference-less electrophysiological monitoring of excitable cells. *Sci. Rep.* **5,** (2015).
200. White, S. P., Dorfman, K. D. & Frisbie, C. D. Label-Free DNA Sensing Platform with Low-Voltage Electrolyte-Gated Transistors. *Anal. Chem.* **87,** 1861–1866 (2015).
201. Chaki, N. K. & Vijayamohanan, K. Self-assembled monolayers as a tunable platform for biosensor applications. *Biosensors and Bioelectronics* **17,** 1–12 (2002).
202. Wink, T., Zuilen, S. J. van, Bult, A. & Bennekom, W. P. van. Self-assembled Monolayers for Biosensors. *Analyst* **122,** 43R–50R (1997).
203. Mrksich, M. & Whitesides, G. M. Using self-assembled monolayers to understand the interactions of man-made surfaces with proteins and cells. *Annu Rev Biophys Biomol Struct* **25,** 55–78 (1996).
204. Zhang, S., Lee, K. H., Frisbie, C. D. & Lodge, T. P. Ionic Conductivity, Capacitance, and Viscoelastic Properties of Block Copolymer-Based Ion Gels. *Macromolecules* **44,** 940–949 (2011).

205. Kim, S. H., Hong, K., Lee, K. H. & Frisbie, C. D. Performance and Stability of Aerosol-Jet-Printed Electrolyte-Gated Transistors Based on Poly(3-hexylthiophene). *ACS Appl. Mater. Interfaces* **5,** 6580–6585 (2013).
206. Mahajan, A., Frisbie, C. D. & Francis, L. F. Optimization of Aerosol Jet Printing for High-Resolution, High-Aspect Ratio Silver Lines. *ACS Appl. Mater. Interfaces* **5,** 4856–4864 (2013).
207. Whitesides, G. M. The origins and the future of microfluidics. *Nature* **442,** 368–373 (2006).
208. Herne, T. M. & Tarlov, M. J. Characterization of DNA Probes Immobilized on Gold Surfaces. *J. Am. Chem. Soc.* **119,** 8916–8920 (1997).
209. Tada, A. *et al.* Interfacial modification of organic photovoltaic devices by molecular self-organization. *Phys. Chem. Chem. Phys.* **14,** 3713–3724 (2012).
210. Chen, C.-Y. *et al.* Concomitant tuning of metal work function and wetting property with mixed self-assembled monolayers. *Organic Electronics* **12,** 148–153 (2011).
211. Sayago, J., Soavi, F., Sivalingam, Y., Cicoira, F. & Santato, C. Low voltage electrolyte-gated organic transistors making use of high surface area activated carbon gate electrodes. *J. Mater. Chem. C* **2,** 5690–5694 (2014).
212. Kergoat, L. *et al.* Tuning the threshold voltage in electrolyte-gated organic field-effect transistors. *PNAS* **109,** 8394–8399 (2012).
213. Minot, E. D. *et al.* Carbon nanotube biosensors: The critical role of the reference electrode. *Applied Physics Letters* **91,** 093507 (2007).
214. Carr, J. A. & Chaudhary, S. On accurate capacitance characterization of organic photovoltaic cells. *Applied Physics Letters* **100,** 213902 (2012).
215. Choi, J.-H. *et al.* High Capacitance, Photo-Patternable Ion Gel Gate Insulators Compatible with Vapor Deposition of Metal Gate Electrodes. *ACS Appl. Mater. Interfaces* **6,** 19275–19281 (2014).
216. Cho, J. H. *et al.* Printable ion-gel gate dielectrics for low-voltage polymer thin-film transistors on plastic. *Nat Mater* **7,** 900–906 (2008).
217. Yuan, H. *et al.* Electrostatic and electrochemical nature of liquid-gated electric-double-layer transistors based on oxide semiconductors. *J. Am. Chem. Soc.* **132,** 18402–18407 (2010).

218. Lockett, V., Horne, M., Sedev, R., Rodopoulos, T. & Ralston, J. Differential capacitance of the double layer at the electrode/ionic liquids interface. *Phys. Chem. Chem. Phys.* **12,** 12499–12512 (2010).
219. Drüschler, M., Huber, B. & Roling, B. On Capacitive Processes at the Interface between 1-Ethyl-3-methylimidazolium tris(pentafluoroethyl)trifluorophosphate and Au(111). *J. Phys. Chem. C* **115,** 6802–6808 (2011).
220. Kornyshev, A. A. & Qiao, R. Three-Dimensional Double Layers. *J. Phys. Chem. C* **118,** 18285–18290 (2014).
221. Hong, K., Kim, S. H., Lee, K. H. & Frisbie, C. D. Printed, sub-2V ZnO Electrolyte Gated Transistors and Inverters on Plastic. *Adv. Mater.* **25,** 3413–3418 (2013).
222. Huang, W., Shi, W., Han, S. & Yu, J. Hysteresis mechanism and control in pentacene organic field-effect transistors with polymer dielectric. *AIP Advances* **3,** 052122 (2013).
223. Noh, Y. H., Young Park, S., Seo, S.-M. & Lee, H. H. Root cause of hysteresis in organic thin film transistor with polymer dielectric. *Organic Electronics* **7,** 271–275 (2006).
224. Kaake, L. G., Zou, Y., Panzer, M. J., Frisbie, C. D. & Zhu, X.-Y. Vibrational Spectroscopy Reveals Electrostatic and Electrochemical Doping in Organic Thin Film Transistors Gated with a Polymer Electrolyte Dielectric. *J. Am. Chem. Soc.* **129,** 7824–7830 (2007).
225. Wada, Y., Pu, J. & Takenobu, T. Strategy for improved frequency response of electric double-layer capacitors. *Applied Physics Letters* **107,** 153505 (2015).
226. Sekitani, T. *et al.* Organic Nonvolatile Memory Transistors for Flexible Sensor Arrays. *Science* **326,** 1516–1519 (2009).
227. Wang, W., Shi, J. & Ma, D. Organic Thin-Film Transistor Memory With Nanoparticle Floating Gate. *IEEE Transactions on Electron Devices* **56,** 1036–1039 (2009).
228. Strakosas, X., Bongo, M. & Owens, R. M. The organic electrochemical transistor for biological applications. *J. Appl. Polym. Sci.* **132,** (2015).

229. de Boer, B., Hadipour, A., Mandoc, M. M., van Woudenbergh, T. & Blom, P. W. M. Tuning of Metal Work Functions with Self-Assembled Monolayers. *Adv. Mater.* **17,** 621–625 (2005).
230. Heimel, G., Romaner, L., Zojer, E. & Bredas, J.-L. The interface energetics of self-assembled monolayers on metals. *Acc. Chem. Res.* **41,** 721–729 (2008).
231. Melitz, W., Shen, J., Kummel, A. C. & Lee, S. Kelvin probe force microscopy and its application. *Surface Science Reports* **66,** 1–27 (2011).
232. Salinas, M. *et al.* The Relationship between Threshold Voltage and Dipolar Character of Self-Assembled Monolayers in Organic Thin-Film Transistors. *J. Am. Chem. Soc.* **134,** 12648–12652 (2012).
233. Celle, C. *et al.* Self-assembled monolayers for electrode fabrication and efficient threshold voltage control of organic transistors with amorphous semiconductor layer. *Organic Electronics* **10,** 119–126 (2009).
234. Fenwick, O. *et al.* Modulating the charge injection in organic field-effect transistors: fluorinated oligophenyl self-assembled monolayers for high work function electrodes. *J. Mater. Chem. C* **3,** 3007–3015 (2015).
235. Mulla, M. Y. *et al.* Capacitance-modulated transistor detects odorant binding protein chiral interactions. *Nat Commun* **6,** 6010 (2015).
236. Steel, A. B., Herne, T. M. & Tarlov, M. J. Electrochemical Quantitation of DNA Immobilized on Gold. *Anal. Chem.* **70,** 4670–4677 (1998).
237. Bozza, W. P., Tolleson, W. H., Rivera Rosado, L. A. & Zhang, B. Ricin detection: Tracking active toxin. *Biotechnology Advances* **33,** 117–123 (2015).
238. Sharma, H. & Mutharasan, R. Review of biosensors for foodborne pathogens and toxins. *Sensors and Actuators B: Chemical* **183,** 535–549 (2013).
239. Liotta, L. A. *et al.* Protein microarrays: Meeting analytical challenges for clinical applications. *Cancer Cell* **3,** 317–325 (2003).
240. Welch, M. E., Doublet, T., Bernard, C., Malliaras, G. G. & Ober, C. K. A glucose sensor via stable immobilization of the GOx enzyme on an organic transistor using a polymer brush. *J. Polym. Sci. Part A: Polym. Chem.* **53,** 372–377 (2015).

241. Syahir, A., Usui, K., Tomizaki, K., Kajikawa, K. & Mihara, H. Label and Label-Free Detection Techniques for Protein Microarrays. *Microarrays* **4,** 228–244 (2015).
242. Chan, C. P. Y. *et al.* Development of a quantitative lateral-flow assay for rapid detection of fatty acid-binding protein. *Journal of Immunological Methods* **279,** 91–100 (2003).
243. Li, X., Luo, L. & Crooks, R. M. Low-voltage paper isotachophoresis device for DNA focusing. *Lab Chip* **15,** 4090–4098 (2015).
244. Moghadam, B. Y., Connelly, K. T. & Posner, J. D. Two Orders of Magnitude Improvement in Detection Limit of Lateral Flow Assays Using Isotachophoresis. *Anal. Chem.* **87,** 1009–1017 (2015).
245. Cunningham, J. C. *et al.* Paper diagnostic device for quantitative electrochemical detection of ricin at picomolar levels. *Lab Chip* **15,** 3707–3715 (2015).
246. Lamont, E. A., He, L., Warriner, K., Labuza, T. P. & Sreevatsan, S. A single DNA aptamer functions as a biosensor for ricin. *Analyst* **136,** 3884–3895 (2011).
247. Ruemmele, J. A., Hall, W. P., Ruvuna, L. K. & Van Duyne, R. P. A Localized Surface Plasmon Resonance Imaging Instrument for Multiplexed Biosensing. *Anal. Chem.* **85,** 4560–4566 (2013).
248. Zhou, J. *et al.* Ultratrace detection of C-reactive protein by a piezoelectric immunosensor based on Fe3O4@SiO2 magnetic capture nanoprobes and HRP-antibody co-immobilized nano gold as signal tags. *Sensors and Actuators B: Chemical* **178,** 494–500 (2013).
249. Hsieh, K., Ferguson, B. S., Eisenstein, M., Plaxco, K. W. & Soh, H. T. Integrated Electrochemical Microsystems for Genetic Detection of Pathogens at the Point of Care. *Acc. Chem. Res.* **48,** 911–920 (2015).
250. White, S. P., Dorfman, K. D. & Frisbie, C. D. Label-Free DNA Sensing Platform with Low-Voltage Electrolyte-Gated Transistors. *Anal. Chem.* **87,** 1861–1866 (2015).
251. Bangar, M. A. *et al.* Single Conducting Polymer Nanowire Based Sequence-Specific, Base-Pair-Length Dependant Label-free DNA Sensor. *Electroanalysis* **23,** 371–379 (2011).

252. Poghossian, A. & Schöning, M. J. Label-Free Sensing of Biomolecules with Field-Effect Devices for Clinical Applications. *Electroanalysis* **26,** 1197–1213 (2014).
253. Cho, E. J., Collett, J. R., Szafranska, A. E. & Ellington, A. D. Optimization of aptamer microarray technology for multiple protein targets. *Anal. Chim. Acta* **564,** 82–90 (2006).
254. Pappa, A.-M. *et al.* Organic Transistor Arrays Integrated with Finger-Powered Microfluidics for Multianalyte Saliva Testing. *Adv. Healthcare Mater.* (2016). doi:10.1002/adhm.201600494
255. White, S. P., Dorfman, K. D. & Frisbie, C. D. Operating and Sensing Mechanism of Electrolyte-Gated Transistors with Floating Gates: Building a Platform for Amplified Biodetection. *J. Phys. Chem. C* **120,** 108–117 (2016).
256. Wang, B., Guo, C., Chen, G., Park, B. & Xu, B. Following aptamer–ricin specific binding by single molecule recognition and force spectroscopy measurements. *Chem. Commun.* **48,** 1644–1646 (2012).
257. Wang, B., Guo, C., Zhang, M., Park, B. & Xu, B. High-Resolution Single-Molecule Recognition Imaging of the Molecular Details of Ricin–Aptamer Interaction. *J. Phys. Chem. B* **116,** 5316–5322 (2012).
258. Wang, B. *et al.* Surface conformations of an anti-ricin aptamer and its affinity for ricin determined by atomic force microscopy and surface plasmon resonance. *Phys. Chem. Chem. Phys.* **17,** 307–314 (2014).
259. Li, X. *et al.* Rapid Detection of Melamine in Milk Using Immunological Separation and Surface Enhanced Raman Spectroscopy. *Journal of Food Science* **80,** C1196–C1201 (2015).
260. Goda, T. & Miyahara, Y. Label-free and reagent-less protein biosensing using aptamer-modified extended-gate field-effect transistors. *Biosensors and Bioelectronics* **45,** 89–94 (2013).
261. Kilic, M. S., Bazant, M. Z. & Ajdari, A. Steric effects in the dynamics of electrolytes at large applied voltages. I. Double-layer charging. *Phys. Rev. E* **75,** 021502 (2007).

262. Fukuda, K. *et al.* Biosensors: Printed Organic Transistors with Uniform Electrical Performance and Their Application to Amplifiers in Biosensors (Adv. Electron. Mater. 7/2015). *Adv. Electron. Mater.* **1,** (2015).
263. Duffy, D. C., McDonald, J. C., Schueller, O. J. & Whitesides, G. M. Rapid Prototyping of Microfluidic Systems in Poly(dimethylsiloxane). *Anal. Chem.* **70,** 4974–4984 (1998).
264. Xiao, Y., Lai, R. Y. & Plaxco, K. W. Preparation of electrode-immobilized, redox-modified oligonucleotides for electrochemical DNA and aptamer-based sensing. *Nat. Protocols* **2,** 2875–2880 (2007).
265. Shewry, P. R., Halford, N. G., Belton, P. S. & Tatham, A. S. The structure and properties of gluten: an elastic protein from wheat grain. *Philos Trans R Soc Lond B Biol Sci* **357,** 133–142 (2002).
266. Wieser, H. Chemistry of gluten proteins. *Food Microbiol.* **24,** 115–119 (2007).
267. Celiac Disease and Nonceliac Gluten Sensitivity | Gastroenterology | JAMA | The JAMA Network. Available at: http://jamanetwork.com/journals/jama/article-abstract/2648637. (Accessed: 11th September 2017)
268. Ch'ng, C. L., Jones, M. K. & Kingham, J. G. C. Celiac Disease and Autoimmune Thyroid Disease. *Clin Med Res* **5,** 184–192 (2007).
269. Ross, M. P. *et al.* Analysis of food-allergic and anaphylactic events in the National Electronic Injury Surveillance System. *Journal of Allergy and Clinical Immunology* **121,** 166–171 (2008).
270. LONG, K. H. *et al.* The economics of celiac disease: a population-based study. *Aliment Pharmacol Ther* **32,** 261–269 (2010).
271. Castillo, N. E., Theethira, T. G. & Leffler, D. A. The present and the future in the diagnosis and management of celiac disease. *Gastroenterol Rep (Oxf)* **3,** 3–11 (2015).
272. Haraszi, R., Chassaigne, H., Maquet, A. & Ulberth, F. Analytical methods for detection of gluten in food--method developments in support of food labeling legislation. *J AOAC Int* **94,** 1006–1025 (2011).
273. Scherf, K. A. & Poms, R. E. Recent developments in analytical methods for tracing gluten. *Journal of Cereal Science* **67,** 112–122 (2016).

274. Van Boekel, M. A. J. S. Kinetic Modeling of Food Quality: A Critical Review. *Comprehensive Reviews in Food Science and Food Safety* **7,** 144–158 (2008).
275. Poms, R. E., Klein, C. L. & Anklam, E. Methods for allergen analysis in food: a review. *Food Additives & Contaminants* **21,** 1–31 (2004).
276. Rallabhandi, P., Sharma, G. M., Pereira, M. & Williams, K. M. Immunological Characterization of the Gluten Fractions and Their Hydrolysates from Wheat, Rye and Barley. *J. Agric. Food Chem.* **63,** 1825–1832 (2015).
277. Alves, T. O., D'Almeida, C. T. S. & Ferreira, M. S. L. Determination of Gluten Peptides Associated with Celiac Disease by Mass Spectrometry. (2017). doi:10.5772/67547
278. Rallabhandi, P. Gluten and Celiac Disease—An Immunological Perspective. *Journal of AOAC International* **95,** 349–355 (2012).
279. Monoclonal antibody sandwich enzyme immunoassays for determination of gluten in foods - Journal of Agricultural and Food Chemistry (ACS Publications). Available at: http://pubs.acs.org/doi/abs/10.1021/jf00098a029. (Accessed: 11th September 2017)
280. García, E. *et al.* Development of a general procedure for complete extraction of gliadins for heat processed and unheated foods. *Eur J Gastroenterol Hepatol* **17,** 529–539 (2005).
281. Collin, P., Mäki, M. & Kaukinen, K. Safe gluten threshold for patients with celiac disease: some patients are more tolerant than others. *Am J Clin Nutr* **86,** 260–260 (2007).
282. Tanner, G. J., Colgrave, M. L., Blundell, M. J., Goswami, H. P. & Howitt, C. A. Measuring Hordein (Gluten) in Beer – A Comparison of ELISA and Mass Spectrometry. *PLOS ONE* **8,** e56452 (2013).
283. Martín-Fernández, B., de-los-Santos-Álvarez, N., Martín-Clemente, J. P., Lobo-Castañón, M. J. & López-Ruiz, B. Challenging genosensors in food samples: The case of gluten determination in highly processed samples. *Talanta* **146,** 490–495 (2016).

284. Amaya-González, S., de-Los-Santos-Álvarez, N., Miranda-Ordieres, A. J. & Lobo-Castañón, M. J. Aptamer binding to celiac disease-triggering hydrophobic proteins: a sensitive gluten detection approach. *Anal. Chem.* **86,** 2733–2739 (2014).
285. Malvano, F., Albanese, D., Pilloton, R. & Di Matteo, M. A new label-free impedimetric aptasensor for gluten detection. *Food Control* **79,** 200–206 (2017).
286. Vasilescu, A., Nunes, G., Hayat, A., Latif, U. & Marty, J.-L. Electrochemical Affinity Biosensors Based on Disposable Screen-Printed Electrodes for Detection of Food Allergens. *Sensors (Basel)* **16,** (2016).
287. Miranda-Castro, R., de-los-Santos-Álvarez, N., Miranda-Ordieres, A. J. & Lobo-Castañón, M. J. Harnessing Aptamers to Overcome Challenges in Gluten Detection. *Biosensors (Basel)* **6,** 16 (2016).
288. Labib, M., Sargent, E. H. & Kelley, S. O. Electrochemical Methods for the Analysis of Clinically Relevant Biomolecules. *Chem. Rev.* **116,** 9001–9090 (2016).
289. Aghagholizadeh, R. *et al.* Characterization of wheat gluten subunits by liquid chromatography – Mass spectrometry and their relationship to technological quality of wheat. *Journal of Cereal Science* **76,** 229–235 (2017).
290. Qian, Y., Preston, K., Krokhin, O., Mellish, J. & Ens, W. Characterization of wheat gluten proteins by HPLC and MALDI TOF mass spectrometry. *J. Am. Soc. Mass Spectrom.* **19,** 1542–1550 (2008).
291. Slot, I. D. B., van der Fels-Klerx, H. J., Bremer, M. G. E. G. & Hamer, R. J. Immunochemical Detection Methods for Gluten in Food Products: Where Do We Go from Here? *Crit Rev Food Sci Nutr* **56,** 2455–2466 (2016).
292. Síglez, M. A. *et al.* GlutenTox® Pro Test for the Detection of Gluten in Select Foods and Surfaces. *Journal of AOAC International* **98,** 1608–1627 (2015).
293. Weng, X., Gaur, G. & Neethirajan, S. Rapid Detection of Food Allergens by Microfluidics ELISA-Based Optical Sensor. *Biosensors* **6,** 24 (2016).
294. Purohit, S., Sharma, A. & She, J.-X. Luminex and Other Multiplex High Throughput Technologies for the Identification of, and Host Response to, Environmental Triggers of Type 1 Diabetes. *Biomed Res Int* **2015,** (2015).

295. Holding, S., Wilson, F. & Spradbery, D. Clinical evaluation of the BioPlex 2200 Celiac IgA and IgG Kits - a novel multiplex screen incorporating an integral check for IgA deficiency. *J. Immunol. Methods* **405,** 29–34 (2014).
296. Lee, K. H. *et al.* 'Cut and stick' rubbery ion gels as high capacitance gate dielectrics. *Adv. Mater. Weinheim* **24,** 4457–4462 (2012).
297. Schalk, K., Lexhaller, B., Koehler, P. & Scherf, K. A. Isolation and characterization of gluten protein types from wheat, rye, barley and oats for use as reference materials. *PLOS ONE* **12,** e0172819 (2017).
298. Performance and Stability of Aerosol-Jet-Printed Electrolyte-Gated Transistors Based on Poly(3-hexylthiophene) - ACS Applied Materials & Interfaces (ACS Publications). Available at: http://pubs.acs.org/doi/abs/10.1021/am401200y. (Accessed: 11th September 2017)
299. Scharnweber, T. *et al.* Rapid prototyping of microstructures in polydimethylsiloxane (PDMS) by direct UV-lithography. *Lab Chip* **11,** 1368–1371 (2011).
300. Herne, T. M. & Tarlov, M. J. Characterization of DNA Probes Immobilized on Gold Surfaces. *J. Am. Chem. Soc.* **119,** 8916–8920 (1997).
301. Jazayeri, M. H., Amani, H., Pourfatollah, A. A., Pazoki-Toroudi, H. & Sedighimoghaddam, B. Various methods of gold nanoparticles (GNPs) conjugation to antibodies. *Sensing and Bio-Sensing Research* **9,** 17–22 (2016).
302. Buth, F., Kumar, D., Stutzmann, M. & Garrido, J. A. Electrolyte-gated organic field-effect transistors for sensing applications. *Appl. Phys. Lett.* **98,** 153302 (2011).
303. Hong, K., Kim, S. H., Lee, K. H. & Frisbie, C. D. Printed, sub-2V ZnO Electrolyte Gated Transistors and Inverters on Plastic. *Adv. Mater.* **25,** 3413–3418 (2013).
304. Hong, K., Kim, S. H., Lee, K. H. & Frisbie, C. D. Organic Electronics: Printed, sub-2V ZnO Electrolyte Gated Transistors and Inverters on Plastic (Adv. Mater. 25/2013). *Adv. Mater.* **25,** 3389–3389 (2013).
305. Li, Y. *et al.* All Inkjet-Printed Metal-Oxide Thin-Film Transistor Array with Good Stability and Uniformity Using Surface-Energy Patterns. *ACS Appl. Mater. Interfaces* **9,** 8194–8200 (2017).
306. Kim, S. H. *et al.* Electrolyte-Gated Transistors for Organic and Printed Electronics. *Adv. Mater.* **25,** 1822–1846 (2013).

307. Cho, E. J., Lee, J.-W. & Ellington, A. D. Applications of aptamers as sensors. *Annu Rev Anal Chem (Palo Alto Calif)* **2,** 241–264 (2009).
308. Cunningham, J. C. *et al.* Paper diagnostic device for quantitative electrochemical detection of ricin at picomolar levels. *Lab Chip* **15,** 3707–3715 (2015).
309. Liu, H., Xiang, Y., Lu, Y. & Crooks, R. M. Aptamer-based Origami Paper Analytical Device for Electrochemical Detection of Adenosine. *Angew Chem Int Ed Engl* **51,** 6925–6928 (2012).
310. Steel, A. B., Herne, T. M. & Tarlov, M. J. Electrochemical Quantitation of DNA Immobilized on Gold. *Anal. Chem.* **70,** 4670–4677 (1998).
311. Tang, L. & Lee, N. Y. A facile route for irreversible bonding of plastic-PDMS hybrid microdevices at room temperature. *Lab Chip* **10,** 1274–1280 (2010).
312. Chang, J., Ge, T. & Sanchez-Sinencio, E. Challenges of printed electronics on flexible substrates. in *2012 IEEE 55th International Midwest Symposium on Circuits and Systems (MWSCAS)* 582–585 (2012). doi:10.1109/MWSCAS.2012.6292087
313. Mahajan, A. *et al.* A Self-Aligned Strategy for Printed Electronics: Exploiting Capillary Flow on Microstructured Plastic Surfaces. *Adv. Electron. Mater.* **1,** n/a-n/a (2015).
314. Senaratne, W., Andruzzi, L. & Ober, C. K. Self-Assembled Monolayers and Polymer Brushes in Biotechnology: Current Applications and Future Perspectives. *Biomacromolecules* **6,** 2427–2448 (2005).
315. Bhattacharjee, N., Urrios, A., Kang, S. & Folch, A. The upcoming 3D-printing revolution in microfluidics. *Lab Chip* **16,** 1720–1742 (2016).
316. Ho, C. M. B., Ng, S. H., Li, K. H. H. & Yoon, Y.-J. 3D printed microfluidics for biological applications. *Lab Chip* **15,** 3627–3637 (2015).
317. Heger, Z. *et al.* 3D-printed biosensor with poly(dimethylsiloxane) reservoir for magnetic separation and quantum dots-based immunolabeling of metallothionein. *Electrophoresis* **36,** 1256–1264 (2015).
318. Kelley, S. O. Advancing Ultrasensitive Molecular and Cellular Analysis Methods to Speed and Simplify the Diagnosis of Disease. *Acc. Chem. Res.* **50,** 503–507 (2017).

319. Rackus, D. G. *et al.* A digital microfluidic device with integrated nanostructured microelectrodes for electrochemical immunoassays. *Lab Chip* **15,** 3776–3784 (2015).
320. Singh, K. V. *et al.* 3D nanogap interdigitated electrode array biosensors. *Anal Bioanal Chem* **397,** 1493–1502 (2010).
321. Squires, T. M., Messinger, R. J. & Manalis, S. R. Making it stick: convection, reaction and diffusion in surface-based biosensors. *Nat Biotech* **26,** 417–426 (2008).
322. Jensen, S. A. *et al.* Spherical Nucleic Acid Nanoparticle Conjugates as an RNAi-Based Therapy for Glioblastoma. *Sci Transl Med* **5,** 209ra152 (2013).
323. Tallarek, U., Vergeldt, F. J. & As, H. V. Stagnant Mobile Phase Mass Transfer in Chromatographic Media: Intraparticle Diffusion and Exchange Kinetics. *J. Phys. Chem. B* **103,** 7654–7664 (1999).
324. Smolsky, J., Kaur, S., Hayashi, C., Batra, S. K. & Krasnoslobodtsev, A. V. Surface-Enhanced Raman Scattering-Based Immunoassay Technologies for Detection of Disease Biomarkers. *Biosensors* **7,** 7 (2017).
325. Stephen Inbaraj, B. & Chen, B. H. Nanomaterial-based sensors for detection of foodborne bacterial pathogens and toxins as well as pork adulteration in meat products. *Journal of Food and Drug Analysis* **24,** 15–28 (2016).
326. Skariyachan, S. *et al.* Environmental monitoring of bacterial contamination and antibiotic resistance patterns of the fecal coliforms isolated from Cauvery River, a major drinking water source in Karnataka, India. *Environ Monit Assess* **187,** 279 (2015).
327. Quintela, I. A., de los Reyes, B. G., Lin, C.-S. & Wu, V. C. H. Simultaneous direct detection of Shiga-toxin producing Escherichia coli (STEC) strains by optical biosensing with oligonucleotide-functionalized gold nanoparticles. *Nanoscale* **7,** 2417–2426 (2015).
328. Ahmed, A., Rushworth, J. V., Hirst, N. A. & Millner, P. A. Biosensors for Whole-Cell Bacterial Detection. *Clin. Microbiol. Rev.* **27,** 631–646 (2014).
329. Nikkhoo, N., Cumby, N., Gulak, P. G. & Maxwell, K. L. Rapid Bacterial Detection via an All-Electronic CMOS Biosensor. *PLOS ONE* **11,** e0162438 (2016).

330. Mannoor, M. S., Zhang, S., Link, A. J. & McAlpine, M. C. Electrical detection of pathogenic bacteria via immobilized antimicrobial peptides. *PNAS* **107,** 19207–19212 (2010).
331. Garrett, T. R., Bhakoo, M. & Zhang, Z. Bacterial adhesion and biofilms on surfaces. *Progress in Natural Science* **18,** 1049–1056 (2008).
332. O'Toole, G. A. & Wong, G. C. Sensational biofilms: surface sensing in bacteria. *Curr Opin Microbiol* **30,** 139–146 (2016).
333. Agrawal, P. *et al.* Fast, Efficient, and Gentle Transfection of Human Adherent Cells in Suspension. *ACS Appl. Mater. Interfaces* **8,** 8870–8874 (2016).
334. G. Reifenberger, J., D. Dorfman, K. & Cao, H. Topological events in single molecules of E. coli DNA confined in nanochannels. *Analyst* **140,** 4887–4894 (2015).
335. Forkus, B., Ritter, S., Vlysidis, M., Geldart, K. & Kaznessis, Y. N. Antimicrobial Probiotics Reduce *Salmonella enterica* in Turkey Gastrointestinal Tracts. *Scientific Reports* **7,** srep40695 (2017).
336. Chortos, A., Liu, J. & Bao, Z. Pursuing prosthetic electronic skin. *Nature Materials* **15,** nmat4671 (2016).
337. Jain, A., K. J., P., Sharma, A. K., Jain, A. & P.n, R. Dielectric and piezoelectric properties of PVDF/PZT composites: A review. *Polym Eng Sci* **55,** 1589–1616 (2015).